NASA CR- 72429
Aerotherm Report No. 68-30

FINAL REPORT

STUDIES OF ABLATIVE MATERIAL PERFORMANCE FOR SOLID ROCKET NOZZLE APPLICATIONS

by

John W. Schaefer
Thomas J. Dahm
David A. Rodriguez
John J. Reese, Jr.
Mitchell R. Wool

prepared for

NATIONAL AERONAUTICS AND SPACE ADMINISTRATION

March 1, 1968

CONTRACT NAS7-534

Technical Management
NASA Lewis Research Center
Cleveland, Ohio
Solid Rocket Technology Branch
J. J. Notardonato

AEROTHERM CORPORATION
485 CLYDE AVENUE, MOUNTAIN VIEW, CALIFORNIA 94040
TELEPHONE (415) 964-3200 • TELEX: 34-8355

ABSTRACT

Analytical and experimental studies of ablative material performance for solid rocket nozzle applications were performed. Large scale computer codes were employed to calculate the ablation, thermal, and structural responses of the 260-SL-3 nozzle as a design check and as a basis for post-fire analysis. The calculated performance included consideration of surface chemical reactions, melt removal, particle deposition, char swelling, in-depth kinetic decomposition, and anisotropic mechanical and thermal properties. Laboratory tests were performed to determine and study the properties and performance mechanisms of three silica phenolic materials - MX2600, MX2600-96, and MXS-113. In performing these tests, an arc plasma generator was used to simulate the solid rocket nozzle environment and a two-dimensional nozzle was used to simulate a large ablative part. The results included the definition of the surface melt removal characteristics and the thermal conductivity of the charring material to 5,000°R for 0° and 90° layup angles. Ablative and thermal performance calculations were also performed for the nozzle of an upper-stage restartable beryllium propellant motor.

SUMMARY

Analytic and experimental studies of ablative material performance for solid rocket nozzle applications were performed. The two main program efforts were 1) a design and analysis study of the ablation, thermal, and structural performance of the 260-SL-3 nozzle and 2) a study of the properties and performance mechanisms of silica phenolic materials. Studies of the technique for calculating heat and mass transfer coefficients for input to ablation calculations, and of the performance of materials for nozzles of restartable beryllium propellant motors were also performed. The results of these studies are summarized in the following paragraphs.

In the design and analysis studies for the 260-SL-3 nozzle, the ablation and thermal performances of the nozzle materials were calculated using the Aerotherm ablation computer programs. These programs consider the thermochemical and, where appropriate, melt removal response of the ablating surface and the detailed in-depth response of the pyrolyzing ablative material. The surface boundary conditions were defined by a detailed flow field analysis which considered the flow nonuniformities due to the cloverleaf grain port configuration. Material performance predictions were made for both the 44-inch subscale nozzle and the 260-inch full scale nozzle prior to the 44-inch motor firing. Based on the post-fire analysis of the 44-SS-4 nozzle through comparisons of measured and predicted performance, it was determined that alumina particle deposition occurred in the reentrant portion of the nozzle in the regions between the propellant lobes. The surface recession due to particle deposition could be accounted for through the chemical reaction of the alumina particles with the carbon phenolic material. Based on this chemical model, the measured performance, and the flow field analysis, the particle deposition rates in the nozzle were defined. The maximum deposition rate occurred at the nose, the most forward region of the nozzle. Char swelling or warp was also identified as an important surface response mechanism for carbon phenolic and was quantified based on the measured and predicted material performance for the 44-SS-4 nozzle. The final predictions of ablation and thermal response for the 260-SL-3 nozzle included consideration of the above response mechanisms. The post-fire measured surface recession and in-depth performance for the 260-SL-3 nozzle agreed favorably with the final predicted response wherever comparisons could be made.

The stress response of the nose region of the 260-SL-3 nozzle was calculated using the Aerotherm thermostructural analysis computer program. This program considers anisotropic properties appropriate to tape-wrapped parts. The ablation and thermal response calculations discussed above

provided the surface boundary conditions and the internal temperature distributions required for these calculations. Based on the structural analysis, it was concluded that the nose region of the nozzle would survive the firing but that this section could drop into the case during the heat soak after the firing. The boundary condition and calculational mesh requirements for an accurate stress calculation were also defined.

In the study of thermal properties and performance mechanisms of silica phenolic materials, the materials considered were MX2600, MX2600-96 (double-thick cloth), and MXS-113 (random fibre tape). The first two materials have nominal 32 percent resin contents, the last material has a nominal 59 percent resin content. MX2600-96 is a lower cost material by virtue of the faster part wrapping time; MXS-113 is a lower cost material by virtue of the lower cost reinforcement. The properties determined for the three materials were the char thermal conductivities, including the conductivity in the partially degraded state, at both 0° and 90° layup angles. The performance mechanisms studied were liquid layer runoff, surface chemical reactions, and solid-phase chemical reactions. The Aerotherm arc plasma generator was used as a rocket simulator to perform these studies. The test configuration was a two-dimensional nozzle in which the test model formed one wall and was obtained from a tape-wrapped ring fabricated by large ablative part standards.

The char thermal conductivity was determined under dynamic test conditions which simulated the exit cone conditions of a typical large booster nozzle. The transient in-depth temperature response of the test models provided the primary conductivity data and the Aerotherm charring material ablation computer program served as the primary data reduction tool. The thermal conductivity was determined to $3,500^{\circ}R$ and extrapolated to higher temperatures. The conductivity in the partially degraded state was lower than that in the virgin and fully-charred states for all three materials. A large affect of layup angle was apparent for both MX2600-96 and MXS-113.

In the study of performance mechanisms for the silica phenolic materials, the test gas simulated a typical solid propellant both chemically and thermodynamically and the test conditions simulated the exit cone of a typical large booster nozzle. The surface response was studied through post-test measurements and observation and through motion picture photography of the ablating surface as seen through a window in the wall opposite the test model. The surface response as depicted by the surface photography showed that the flow of the melt was very erratic and the surface exhibited significant nonuniformities in temperature for the low removal rates experienced. The flow of the silica melt was characterized by a fail temperature of $3,600^{\circ}R$, the temperature above which silica will flow. No evidence of

reactions between the condensed phase silica and carbon of the char was apparent. Char swelling or warp apparently did not occur for the materials considered. The MX2600-96 material exhibited a performance which was essentially equivalent to MX2600 in all respects. The MXS-113 material exhibited a structurally weak char and greater surface recession which made it somewhat inferior to the other two materials.

The third program phase was the brief study of heat and mass transfer coefficient and radiative boundary condition input to an ablation calculation. On the basis of this study, it was tentatively concluded that the heat and mass transfer coefficients as calculated by the Aerotherm boundary layer integration computer program, using accurate transport properties, must be reduced by 25 percent to accurately define these coefficients for ablation calculations.

The final program phase was the study of material performance in the nozzle of an upper stage beryllium propellant motor. Material ablation and thermal performances for a primary firing and a secondary restart firing were calcuated for the pyrolytic graphite throat and graphite phenolic exit cone for a hypothetical nozzle and duty cycle. Screening calculations were also performed for several potential nozzle materials. For the particular nozzle design and duty cycle, the graphite phenolic exit cone was almost completely charred and the silica phenolic backup material in the throat charred significantly prior to the secondary burn. The nozzle integrity during the restart firing was therefore found to be somewhat questionable. In the screening calculations, tungsten was determined to be the most attractive material from a surface recession standpoint; it, of course, is not attractive from a weight, structural, and thermal standpoint. Silica phenolic, silicon carbide, beryllium oxide, and beryllium exhibited excessive surface recession. Graphite and carbon- and graphite-phenolic appeared to be the most attractive material choices. Based on the screening calculations, beryllium oxide deposition on the exposed material surface can occur due to the "condensation" of beryllium gas phase species in the combustion products. This deposition results in a reduced surface recession.

TABLE OF CONTENTS

LIST OF FIGURES

LIST OF FIGURES - Continued

LIST OF TABLES

LIST OF SYMBOLS

A	area (various subscripts), or one of two phenolic decomposition reactions
B	one of two phenolic decomposition reactions
B'	dimensionless particle deposition rate, defined $\dot{m}_p/\rho_e u_e C_M$
c_p	specific heat at constant pressure
C_H	Stanton number (heat transfer coefficient/$\rho_e u_e$)
$\tilde{C}_H$	local heat transfer coefficient ratio, defined $\rho_e u_e C_H/(\rho_e u_e C_H)_*$
C_M	mass transfer Stanton number, $C_M = C_H\ (Le)^{2/3}$
D_*	throat diameter
E	voltage
$f\ (\ )$	implied functional relationship
$f_1(\ ),\ f_2(\ )$	thermal conductivity weighting functions for virgin material and char, respectively
h	specific enthalpy (various subscripts)
$i,\ j$	nodal coordinates
I	current
k	thermal conductivity (various subscripts)
Le	Lewis number, defined Pr/Sc
$\dot{m}$	mass rate (various subscripts)
M	Mach number
p	pressure
Pr	Prandtl number
r	radial direction
R	nozzle radius, or recovery factor
$s,\ \dot{s}$	surface recession, surface recession rate
Sc	Schmidt number
$t_b,\ t_{web}$	total burn time
T	temperature
u	gas velocity
x	virgin material mass fraction, defined $\frac{\rho_p}{\rho_p-\rho_c}\left(1-\frac{\rho_c}{\rho}\right)$
z	axial direction

Subscripts

c	char material, or chamber property
e	boundary layer edge property
p	virgin material (plastic), or grain port cross section, or particle deposition, or free stream particles
po	grain port cross-section at $\tau = 0$
ref	reference or ambient property
t,o	total or stagnation property
w	wall or surface property
1	one of two conductivity weighting factors
2	one of two conductivity weighting factors
44	refers to calculations for 44-SS-4 motor
260	refers to calculations for 260-SL-3 motor
θ	layup angle (see table 2-3, table 3-6, notes b.)
*	throat property

Superscripts

'	$\theta = 60^{\circ}$ azimuth (behind lobes), or (see B')
•	denotes time rate of change (i.e. $\dot{s}$)
*	indicates condensed phase species (i.e. C*), or flags a footnote.

Greek

α	compliment of the tape wrap angle ($90 - \phi$)
γ	ratio of specific heats
δ	(See page 23)
δ_c	char depth
Δ	change of
ε	emissivity (various subscripts)
θ	layup angle reference to surface tangent, or nozzle azimuth angle

λ	boundary layer running length
ξ	(see Figure 4-1, page 123)
ρ	system density, or component or location density (various subscripts)
τ	propellant web fraction, defined propellant surface regression/initial propellant web thickness, or shear stress

Miscellaneous Combinations

const	constant value
$\dot{m}_p/\rho_e u_e C_M$	dimensionless particle deposition rate
$(\dot{m}_p)_{\tau=0}$	maximum particle deposition rate at $\tau=0$
R/D_*	dimensionless nozzle radius
λ/D_*	dimensionless running length
ρu	mass flux
$\tilde{\rho u}$	dimensionless mass flux, defined $\rho u/\rho_* u_*$
$\rho_* u_*/P_c$	reciprocal of the characteristic velocity
2D	two-dimensional
$\propto$	proportional to
$\pm$	plus or minus
$\leq$	less than or equal to
=	equal to

SECTION 1
INTRODUCTION

The economical design and development of ablative nozzles for large sclid boosters requires an optimum use of

Sophisticated design techniques
Laboratory tests
Subscale firings
Material performance analysis

and a minimum use of costly full-scale firings. Sophisticated design techniques include detailed ablation and structural analysis computer programs. Such techniques provide a complete description of the surface recession and in-depth thermal response of nozzle ablative parts and of the structural response of the nozzle assembly, ablative parts, and bond lines. Laboratory tests encompass cold flow tests which provide a definition of boundary conditions, and rocket simulator firings which provide a definition of materials response mechanisms and properties. Such tests must be accompanied by experimental and theoretical analysis to provide the information required for the design techniques. Subscale motor firings provide the final verification and/or basis for modification of the full-scale nozzle design. Verification is provided by a favorable comparison of the nozzle and ablative parts performance predictions with the actual performance, the prediction technique being that used for the full-scale nozzle design. Unfavorable comparison provides the basis for defining and quantifying the mechanisms which must be included in the design techniques for an accurate design prediction.

This report presents the results of a nozzle design and development support program in which all the above aspects of nozzle design were applied. Predictions of the ablative parts performance - ablation, thermal, and structural - were made for the 260-SL-3 260 inch motor nozzle and the 44-SS-4 subscale nozzle as a design check and as basis for post-fire analysis of the parts performance. A post-fire analysis was performed for both nozzles and a study was performed to define the requirements for an accurate structural analysis. This part of the overall program effort, specifically related to the 260-SL-3 nozzle, is presented in Section 2.

Laboratory tests using an arc plasma generator as a rocket simulator were performed to define and study the thermal properties and performance mechanisms of silica phenolic materials. The materials considered were MX2600 silica phenolic, MX2600-96 silica phenolic, and MXS-113 silica phenolic, the last two being lower cost materials. Char thermal conductivity was defined and the surface removal mechanisms of liquid layer runoff, surface chemical

reactions, and condensed phase reactions were studied. This phase of the overall program effort is presented in Section 3.

A study was also performed to define the effects of boundary condition input, primarily heat and mass transfer coefficients, on the predicted surface response of carbon phenolic. A parametric study using the 260-SL-3 nozzle throat as an example was performed and potential sources of error in the definition of boundary condition input were defined. This effort is presented in Section 4.

Finally, a special study of materials performance in the nozzle of an upper-stage beryllium propellant motor was also performed. Ablation performance was predicted for a hypothetical nozzle design and a materials screening study was performed for several candidate nozzle materials. The results of this effort are presented in Section 5.

SECTION 2

DESIGN AND ANALYSIS STUDIES FOR THE 260-SL-3 NOZZLE

The Aerotherm ablation and structural analysis computer programs were used to predict the performance of the 260-SL-3 and 44-SS-4 nozzles. Based on these results, an assessment of the nozzle design was made and, after the firings, a post-fire analysis was performed. A study of the requirements for accurate calculations of nozzle structural response was also performed. The results of this program phase are presented in this section. Section 2.1 describes the motors and nozzles and Section 2.2 describes the ablation performance prediction techniques. The flow field analysis to define the nozzle boundary conditions is presented in Section 2.3. Section 2.4 presents the predictions of ablation and thermal response and the post-fire analysis for both nozzles. Finally, Section 2.5 presents the stress analysis and related structural analysis studies.

2.1 MOTOR AND NOZZLE DESCRIPTION

The motor and nozzle configurations and the firing conditions for the 260-SL-3 and 44-SS-4 motors are presented briefly below. Only those details particularly pertinent to the prediction of material performance are presented; the complete description may be found in Reference 2-1.

The propellant for the 260-SL-3 motor was a standard aluminized propellant, Aerojet ANB-3254. The propellant grain port had a cloverleaf cross-section as shown in Figure 2-1. The nozzle was submerged with the most forward point being at an area ratio of 2.0. The propellant face was angled to accomodate the submerged nozzle; no propellant was included underneath the reentrant part

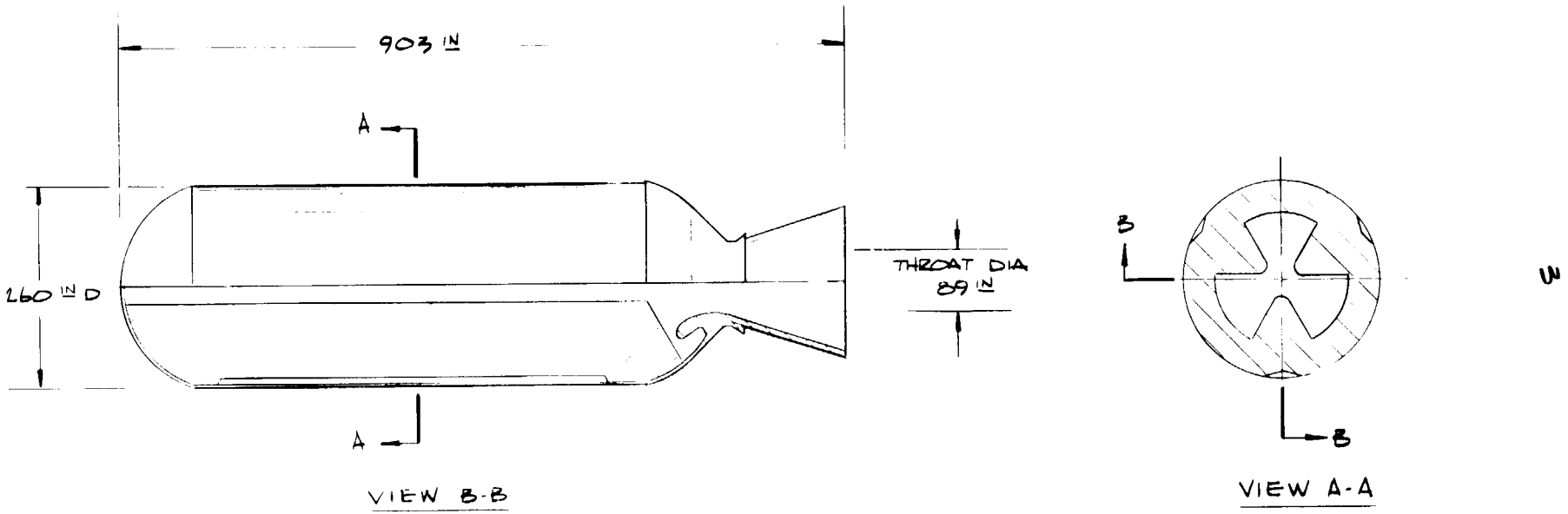

FIGURE 2-1 SCHEMATIC OF THE 260-SL-3 MOTOR

A 1160

of the nozzle. The projected pre-fire chamber pressure history on which the analyses presented in subsequent sections was based is presented in Figure 2-2.

The 260-SL-3 nozzle configuration is shown in detail in Figure 2-3. The throat diameter was 89 inches. The exposed ablative materials were FM 5131 silica phenolic in the underneath portion of the nozzle and in the exit cone starting at an area ratio of 2.5 and MX4926 carbon phenolic at all other locations. The layup angles for each ablative part are indicated schematically in the figure. All parts were hydroclave cured using standard procedures. No unusual conditions were known to exist in any of the parts except for wrinkling of the cloth and a possible delamination in the exit cone part at an area ratio of about 2.8.

The locations for which predictions of material ablation and thermal performance were made are also indicated in Figure 2-3. The description of these locations is summarized in Table 2-1.

The 44-SS-4 motor was a subscale to the 260-SL-3 motor, the nozzle configuration and propellant grain port cross-section being geometrically similar. The same ANB-3254 propellant was used. The projected pre-fire chamber pressure history on which the subsequent analyses were based is presented in Figure 2-4. The detailed nozzle configuration is presented in Figure 2-5. The throat diameter was 15.5 inches. There was no exit cone, per se, the nozzle exit area ratio being 2.5. The same exposed ablative materials were used in both the 260-SL-3 and 44-SS-4 nozzle. All ablative parts were hydroclave cured and no unusual conditions were known to exist. The prediction locations, shown in the figure, coincided with those of the 260-SL-3 nozzle and are summarized in Table 2-2.

2.2 MATERIAL PERFORMANCE PREDICTION TECHNIQUE

The performance prediction of material response encompassed the determination of surface recession, including chemical corrosion and mechanical erosion, and surface and internal thermal response of the exposed ablative and backup materials, including surface and in-depth temperatures and in-depth decomposition. The tools used for these predictions were the Aerotherm ablation computer programs. These programs are discussed briefly below.

The programs appropriate to charring materials and used in the predictions are:

Aerotherm Chemical Equilibrium (ACE) Program *

Charring Material Thermal Response and Ablation (CMA) Program

The first program is concerned with the thermochemical behavior of the material surface when exposed to a chemically reactive environment. The surface removal mechanisms considered by the program are chemical corrosion, decomposition, phase change, and liquid layer runoff. The CMA program calculates the

* The more powerful ACE program is now used in place of the original Equilibrium Surface Thermochemistry (EST) program.

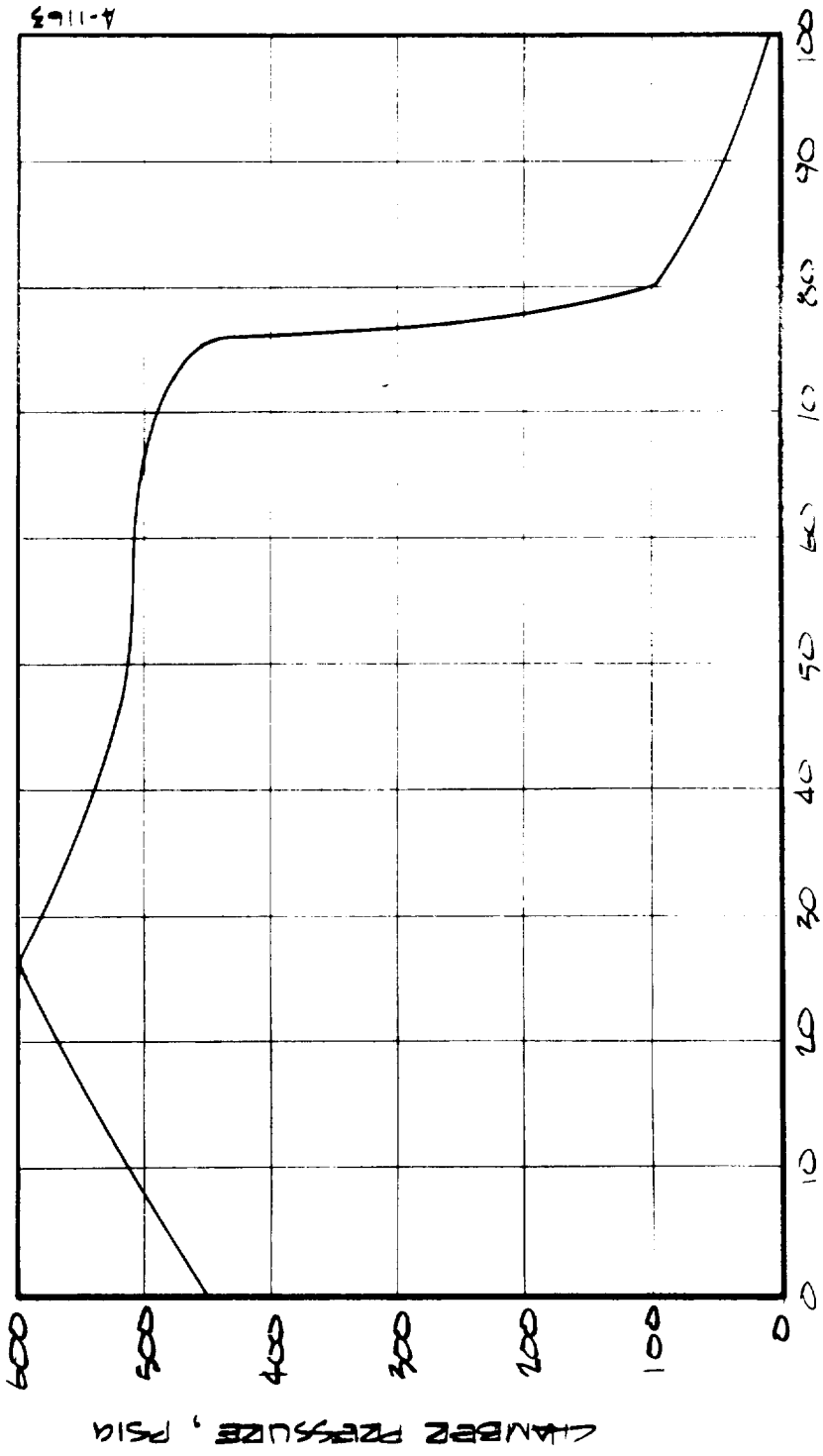

FIGURE 2.2 PROJECTED CHAMBER PRESSURE HISTORY FOR THE 260-SL-3 MOTOR.

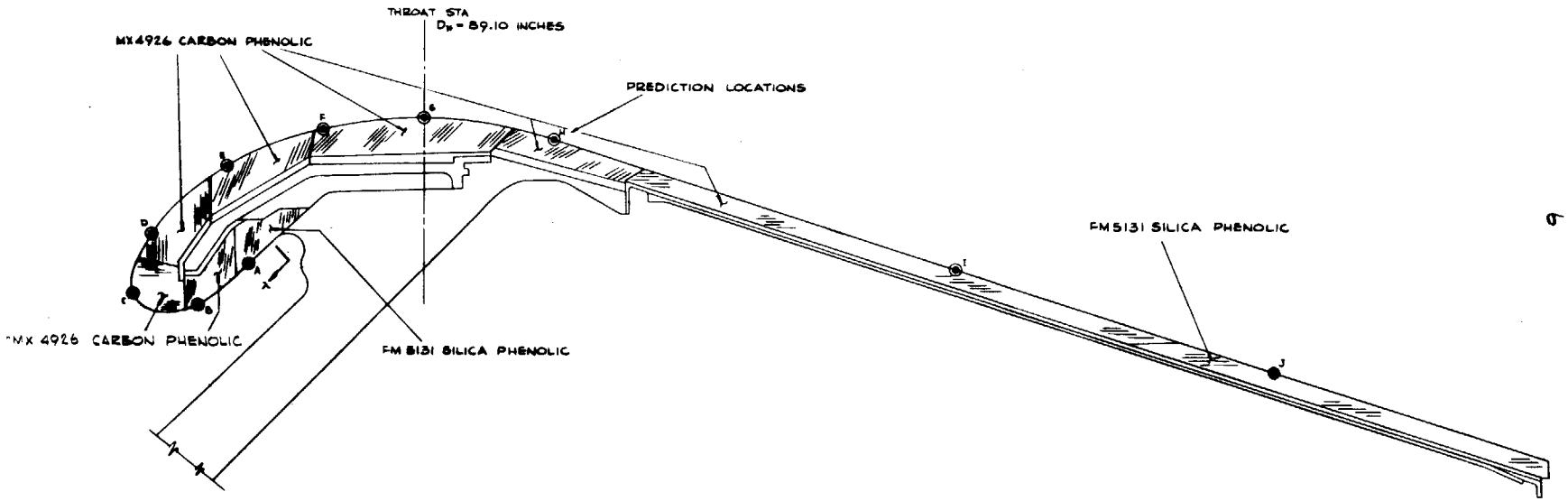

FIGURE 2-3 260-SL-3 NOZZLE CONFIGURATION

TABLE 2-1

PREDICTION LOCATIONS IN THE 260-SL-3 NOZZLE

Location	λ/D_* [a]	A/A_*	Material	Layup [b] Angle
A	-0.605	- underside	FM5131 Silica Phenolic	82°
B	-0.538	- underside	MX4926 Carbon Phenolic	
C [c]	-0.465	-2.00 nose leading edge		0°
D [c]	-0.398	-1.80		90°
E [c]	-0.252	-1.26		67.5°
F [c]	-0.125	-1.06		45°
G [c]	0	1.0		
H	0.208	1.15		30°
I	0.720	1.90		0°
J	1.211	2.80	FM5131 Silica Phenolic	

a) Referenced to the throat; boundary layer assumed to start at $\lambda/D_* = -0.650$.

b) Referenced to the centerline.

c) Predictions made both between propellant lobes (0°) and behind propellant lobes (60°).

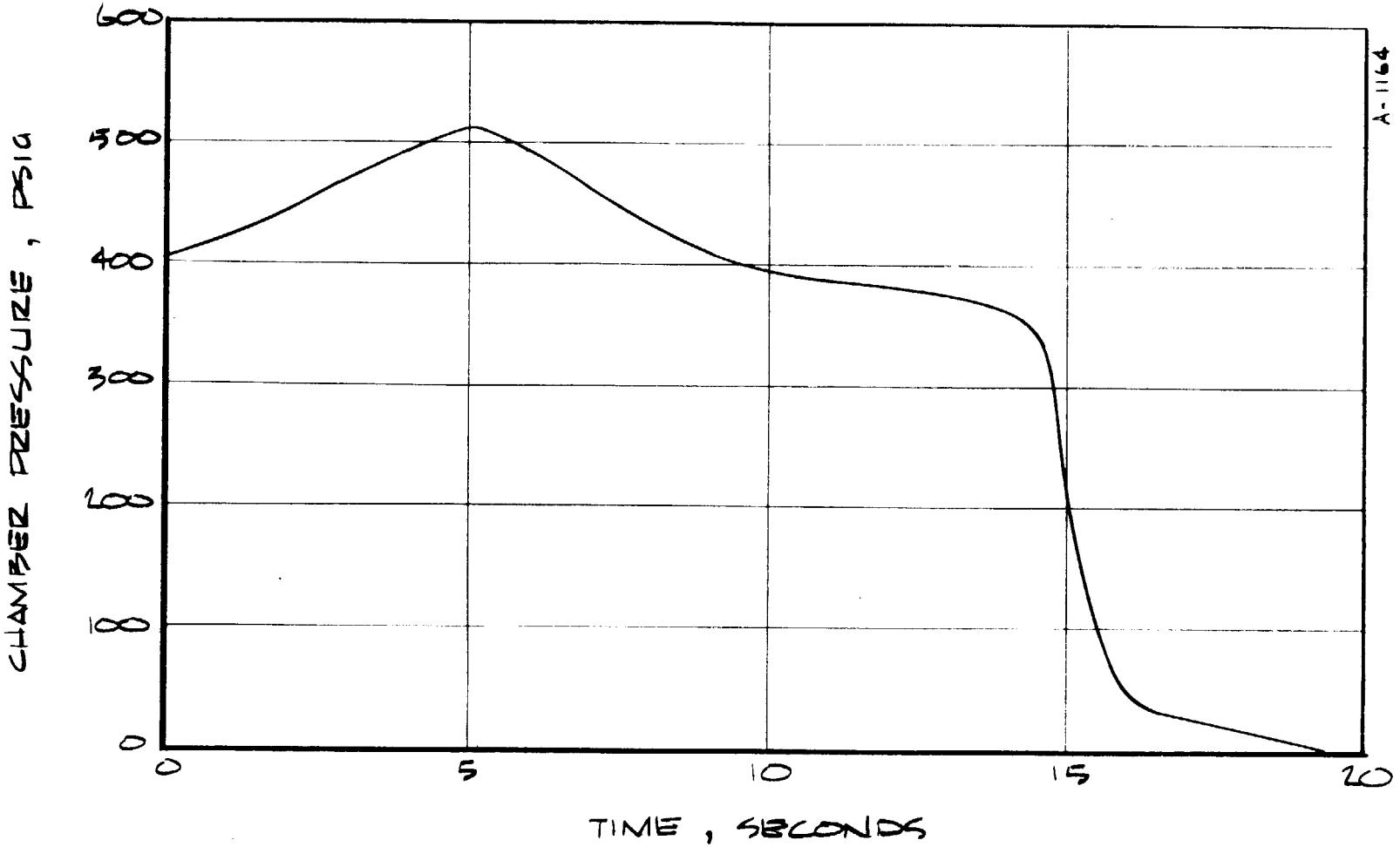

FIGURE 2-4 PROJECTED CHAMBER PRESSURE HISTORY FOR THE 44-55-4 MOTOR.

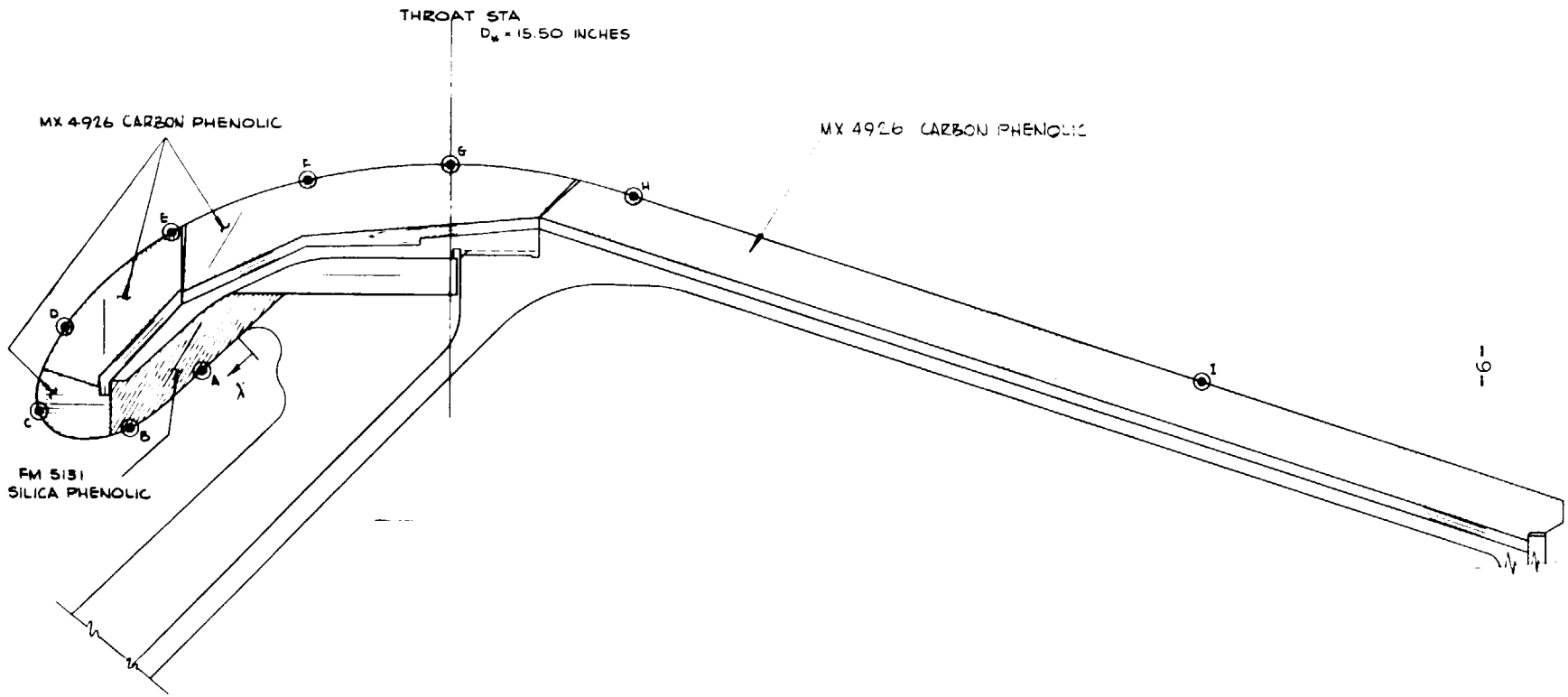

FIGURE 2-5 44-SQ-4 NOZZLE CONFIGURATION

TABLE 2-2

PREDICTION LOCATIONS IN THE 44-SS-4 NOZZLE

Location	λ/D_* [a]	A/A_*	Material	Layup Angle [b]
A	-0.605	- underside	FM5131 Silica Phenolic	60°
B	-0.538	- underside	d	
C [c]	-0.465	-2.00 nose leading edge	MX4926 Carbon Phenolic	0°
D [c]	-0.398	-1.80		90°
E [c]	-0.252	-1.26		60°
F [c]	-0.125	-1.06		
G	0	1.0		
H	0.208	1.15		30°
I	0.720	1.90		

a) Referenced to the throat; boundary layer assumed to start at $\lambda/D_* = -0.650$.

b) Referenced to the centerline.

c) Predictions made both between propellant lobes (0°) and behind propellant lobes (60°).

d) Predictions made for silica phenolic prior to design change to carbon phenolic.

material transient response in terms of surface recession and surface and internal thermal response, part of the input being generated by the ACE program. The internal thermal response includes the calculation of the decomposition in depth of organics to form a char. These programs are discussed in greater detail in References 2-2 through 2-5.

The input information required to predict material performance is:

Combustion products chemical composition
Local gas temperature and pressure, recovery enthalpy
Transfer coefficients (heat and mass)
Incident radiation heat flux

Material elemental chemical composition - reinforcement and resin, or composite
Material density - virgin material and char
Material thermal properties
- Specific heat
- Thermal conductivity
- Surface emissivity
- Heat of formation

} Virgin material and char

Kinetic constants of decomposition - resin and, if applicable, reinforcement, or composite

The first group of input is related to the motor and nozzle; this information defines the boundary conditions to which the material is exposed. The latter group of input characterizes the material response to the boundary conditions. The definition of propellant type (ANB-3254) and a standard combustion calculation provides the combustion products chemical composition. The other three sets of boundary conditions input information requires a flow field analysis. This analysis for the two motors is presented in the following section, Section 2.3.

The material property input information was available for MX4926 carbon phenolic (Reference 2-2) and is presented in Table 2-3. The input for FM5131 silica phenolic was estimated from the results of Reference 2-2 and 2-6 and is also included in Table 2-3. For silica phenolic, the thermal conductivity was treated as being a function of temperature and degradation state such that in the partially degraded state the conductivity was lower than both the virgin material and char values. This is a realistic model and is discussed further in Section 3. Also for silica phenolic, liquid layer runoff was included in the surface response calculations through specification of a fail temperature for silica (Table 2-3). The fail temperature is typically the melt temperature for the particular surface species. Although silica exhibits no discrete melt temperature but rather a continually decreasing viscosity with increasing temperature, the "phase change" value from Reference

Table 2-3 Thermal and Physical Properties of Carbon Phenolic and Silica Phenolic Used in the Predictions of the 260-SL-3 and 44-SS-4 Nozzle Material Performance

Material	Nominal Density (lb/ft^3)	Nominal Resin Mass Fraction	Resin Residual	Resin Elemental Formula (Phenolic)	Reinforcement Elemental Formula	Fail Temperature (^oR)	Virgin Material					Char				Virgin Material Mass Fraction	Thermal Conductivity Weighting Function	
							Temperature (^oR)	Specific Heat ($Btu/lb\ ^oR$)	Thermal Conductivity $\times 10^4$ ($Btu/ft\ sec\ ^oR$) 0^o Layup	Thermal Conductivity $\times 10^4$ ($Btu/ft\ sec\ ^oR$) 90^o Layup	Emissivity	Specific Heat ($Btu/lb\ ^oR$)	Thermal Conductivity $\times 10^4$ ($Btu/ft\ sec\ ^oR$) 0^o Layup	Thermal Conductivity $\times 10^4$ ($Btu/ft\ sec\ ^oR$) 90^o Layup	Emissivity		Virgin Material	Char
MX4926 Carbon Phenolic	89.4	0.345	0.40	C_6H_6O	C	--	530	0.210	1.39	2.36	0.85	0.210	1.83	3.11	0.85	1.0	1.0	0
							800	0.360	1.58	2.69		--	--	--		0.5	0.5	0.5
							1000	--	--	--		0.430	1.90	3.15		0.0	0.0	1.0
							1160	0.360	1.83	3.11		--						
							1500	0.472				0.472	1.95	3.20				
							2000	0.484				0.484	2.35	4.15				
							3000	0.493				0.493	5.40	8.95				
							4000	0.498				0.498	11.55	14.70				
							5000	0.500				0.500	18.80	21.25				
							6000	0.500				0.500	26.50	28.35				
FM5131 Silica Phenolic[d]	108.2	0.325	0.50	C_6H_6O	SiO_2	3389	530	0.260	0.885[e]		0.85	0.210	2.85[e]		0.85	1.0	1.0	0.0
							1000	--				0.430	3.02			0.9	0.5	0.0
							1160	0.310				--	--			0.6	0.5	0.0
							1500	0.472				0.472	3.22			0.5	0.0	1.0
							2000	0.484				0.484	3.42			1.0	0.0	1.0
							3000	0.493				0.493	5.53					
							4000	0.498				0.498	8.40					
							5000	0.500				0.500	12.20					
							6000	0.500				0.500	12.20					

a) The decomposition kinetic constants for phenolic resin are tabulated below. The residual densities tabulated for reaction B correspond to a resin residual of 0.40 and 0.50, respectively.

Reaction	Initial Density (lb/ft^3)	Residual Density (lb/ft^3)	Pre-exponential Factor (sec^{-1})	Activation Energy Factor (^oR)	Density Factor Exponent
A	20.25	0	1.40×10^4	15,400	3
B	60.75	32.40 40.50	4.48×10^8	36,800	3

b) The following equation was used for layup angles other 0^o and 90^o

$$k_\theta = k_{0^o}\left[1 + \left(\frac{k_{90^o}}{k_{0^o}} - 1\right)\sin\theta\right]$$

where θ is the layup angle referenced to a tangent to the surface.

c) The conductivity is given by

$$k = f_1(x)\ k_p(T) + f_2(x)\ k_c(T)$$

where x is the virgin material mass fraction, $f_1(x)$ and $f_2(x)$ are the virgin material and char weighting functions, respectively, and k_p and k_c are the virgin material and char conductivities, respectively.

d) Data for silica phenolic materials obtained in the experimental phase of the overall program are presented in Table 3-6.

e) These data are for MXS-89 silica phenolic at 90^o layup angle from Reference 2-6 and were used herein independent of layup angle.

2-7 was used.

The liquid layer removal model was checked out early in the program and these results are presented here. A prediction of the silica phenolic response in the exit cone of the 260-SL-1 nozzle was made at a location for which recession measurements were available (Reference 2-2). The comparison of predicted and measured surface and in-depth response with and without the liquid runoff model is shown in Table 2-4. The predicted and measured surface recessions are almost identical when liquid layer removal is considered; the measured char depth falls between the predicted char and pyrolysis zone depths. Based on these results, the more sophisticated treatment of silica phenolic response appears quite accurate. Further details on liquid runoff are presented in Section 3.

2.3 FLOW FIELD ANALYSES

The flow field analyses pertinent to the prediction of the 44-SS-4 and 260-SL-3 nozzle ablative material performances are presented in this section. The analyses were of three types: 1) determination of boundary layer edge conditions; 2) estimation of the boundary layer behavior subject to the nozzle geometry, boundary layer edge conditions, and wall conditions, and 3) post-fire evaluation of the 44-SS-4 material behavior as influenced by the actual subscale motor flow field behavior. Analyses 1 and 2 are presented in 2.3.1, with the latter analysis appearing in Section 2.3.2.

2.3.1 Prefire Analyses

2.3.1.1 Boundary Layer Edge Conditions

Boundary layer edge conditions constitute a portion of the input to the boundary layer program for the computation of heat and mass transfer coefficients. Certain of these edge conditions, along with the estimated heat and mass transfer coefficients from the boundary layer program, constitute a portion of the input to the subsequent material performance calculations. A general description of the procedures employed herein to obtain this input information for a given propellant is presented in the following paragraphs.

The first step consisted of the determination of properties that would exist for an equilibrium, isentropic expansion from chamber conditions to a range of static pressures employing the ACE computer program. A portion of the results obtained from this calculation consisted of temperature, density, velocity, mass flux (density times velocity), and molecular composition as a function of static pressure ($\overline{\leq} p_c$). The mass fluxes were then nondimensionalized by the maximum mass flux during the expansion, $(\rho_* u_*)$, the mass flux that would occur at the throat of a nozzle for a one-dimensional-isentropic expansion process.

TABLE 2-4

PREDICTED PERFORMANCE FOR SILICA PHENOLIC WITH DIFFERENT SURFACE RECESSION MECHANISMS, 260-SL-1 NOZZLE AT $A/A_* = 3.8$

Recession Mechanism	Surface Recession (in)		Char Depth[a] (in)		Pyrolysis Zone Depth[a] (in)
	Predicted	Measured	Predicted	Measured	Predicted
Surface Chemical reaction and liquid removal	0.467	0.46	0.773	0.88	0.927
Surface chemical reactions only	0.177	0.46	0.55	0.88	-

a) Referenced to original surface.

$$\tilde{\rho u} \equiv \frac{\rho u}{\rho_* u_*} \tag{2-1}$$

From this point on, the non-dimensional mass flux, $\tilde{\rho u}$, and chamber pressure, p_c, were taken as the independent variables to which all boundary layer edge conditions can be conveniently related. The convenience is due in part to the fact that for typical solid propellants it is found that the variation of the parameters p/p_c, T, and u with $\tilde{\rho u}$ for an isentropic expansion is essentially independent of the chamber pressure employed in the calculation, as is the reciprocal of the propellant characteristic velocity, $\rho_* u_*/p_c$. More significantly, the convenience of the parameter $\tilde{\rho u}$ lies in the fact that for geometries for which a one-dimensional flow hypothesis is acceptable, the variation of $\tilde{\rho u}$ along a nozzle surface is independent of the fluid flowing through the nozzle and the scale of the nozzle (assuming geometric similarity between subscale and full scale nozzles). From this fact, it is reasonable to suppose that the variation of $\tilde{\rho u}$ is geometry-dependent only even for 3-dimensional flow geometries, providing a simple framework for incorporation of the many considerations of flow field behavior (e.g., application of experimental cold flow results to the estimation of the behavior of solid propellant combustion products).

The elemental composition of the propellant is an input parameter to the isentropic expansion calculations. The boundary layer edge molecular composition was determined from the elemental composition and equilibrium calculations, yielding the variation (among other things) of the mass fraction of condensed species for the equilibrium isentropic expansion process. These condensed species enter into the estimation of the flow field behavior in several important ways. For example, they influence the state of the gases at the edge of the boundary layer through their (assumed) equilibrium with the gases, and they may exist within the boundary layer to alter in an unknown way the behavior of the boundary layer. In addition to their effects on the flow field, they can interact with nozzle insulation materials if these condensed phases penetrate the boundary layer, and they are the primary contributors to radiation heat flux to the nozzle insulation material. In the case of solid propellant combustion products, the very existence of condensed species may also give rise to non-equilibrium effects due to their inertia (thermal and kinetic lags during the expansion process).

The flow field analysis is considerably simplified if it is assumed that condensed species are in equilibrium with the boundary layer edge gases, and that they do not penetrate the boundary layer. Employing the equilibrium assumption, it is typically found for solid propellant combustion products that the mass fraction of condensed species is approximately invariant during the

isentropic expansion process. The influence of condensed species on the boundary layer has been typically ignored, as has the presence of the condensed species in terms of potential chemical reactions with the wall. In addition, the mass and energy (sensible enthalpy) contributions of the condensed species are deleted from the system. However, condensed phases contribute energy flux to the nozzle wall (which is included here) by virtue of radiation typically at their local temperature, which is the local gas temperature by the equilibrium assumption.

These simplifications, along with the simplification of equilibrium expansion and constant mass fraction of condensed species during the expansion process, yield a value of $\rho_* u_* / p_c$ reduced by the contribution of the condensed phases to the mass flux. In this case, values of $\tilde{\rho u}$ are the same with or without consideration of condensed phases in the system (another convenience of the parameter, $\tilde{\rho u}$).

At this point, the boundary layer edge conditions consist of pressure ratio, temperature, velocity, and "gas alone" composition and enthalpy as a function of $\tilde{\rho u}$. These parameters must be related to the nozzle geometry, and the nozzle materials. Relation to the geometry comes from further analysis of the flow field behavior, described below; relation to the materials comes from further chemical and energy calculations described in Section 2.4.

The nozzle geometries under consideration were presented in Figures 2-3 and 2-5. The orientation of the nozzle entry region with respect to the propellant grain is presented in Figure 2-6, taken from Reference 2-8. The variation of nozzle radius with surface running length, λ, is presented in Figure 2-7. Because of the proximity of the propellant grain to the re-entrant nozzle, the boundary layer edge mass flux, $\tilde{\rho u}$, depends upon the distance, λ, along the nozzle surface from the stagnation line on the underside of the nozzle; the azimuthal orientation, θ, with respect to the propellant grain lobes; and the propellant web fraction, τ, which influences the proximity of the propellant grain geometry, and by certain flow irreversibilities associated with flow separation off the end of the grain, and subsequent flow circulation which is indicated by the arrows in Figure 2-6.

It is convenient now to enumerate the generalized flow field analysis assumptions which have been previously expressed or implied. In relation to boundary layer edge conditions including condensed phases (if appropriate), these reduce to:

1. The value of $\tilde{\rho u}$ is a function of the nondimensional nozzle surface coordinate, λ/D_*, propellant web fraction, τ (=propellant surface regression/initial propellant web thickness), and nozzle azimuth, θ, independent of the boundary layer edge medium and independent of system scale.

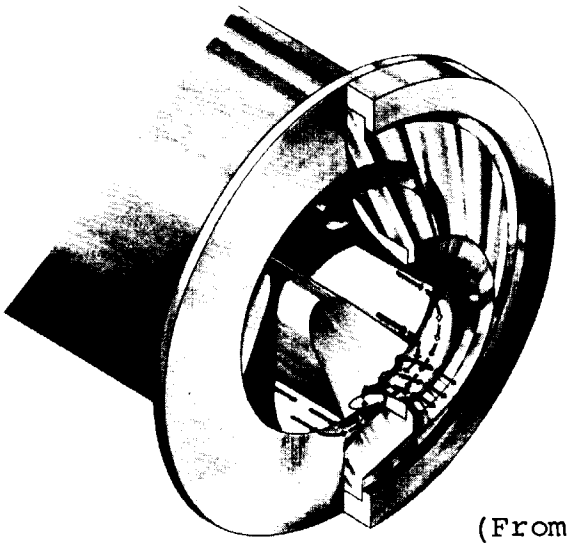

(From Reference 2-8)

Figure 2-6 Typical flow pattern in annular passage between nozzle lip and aft-end casing.

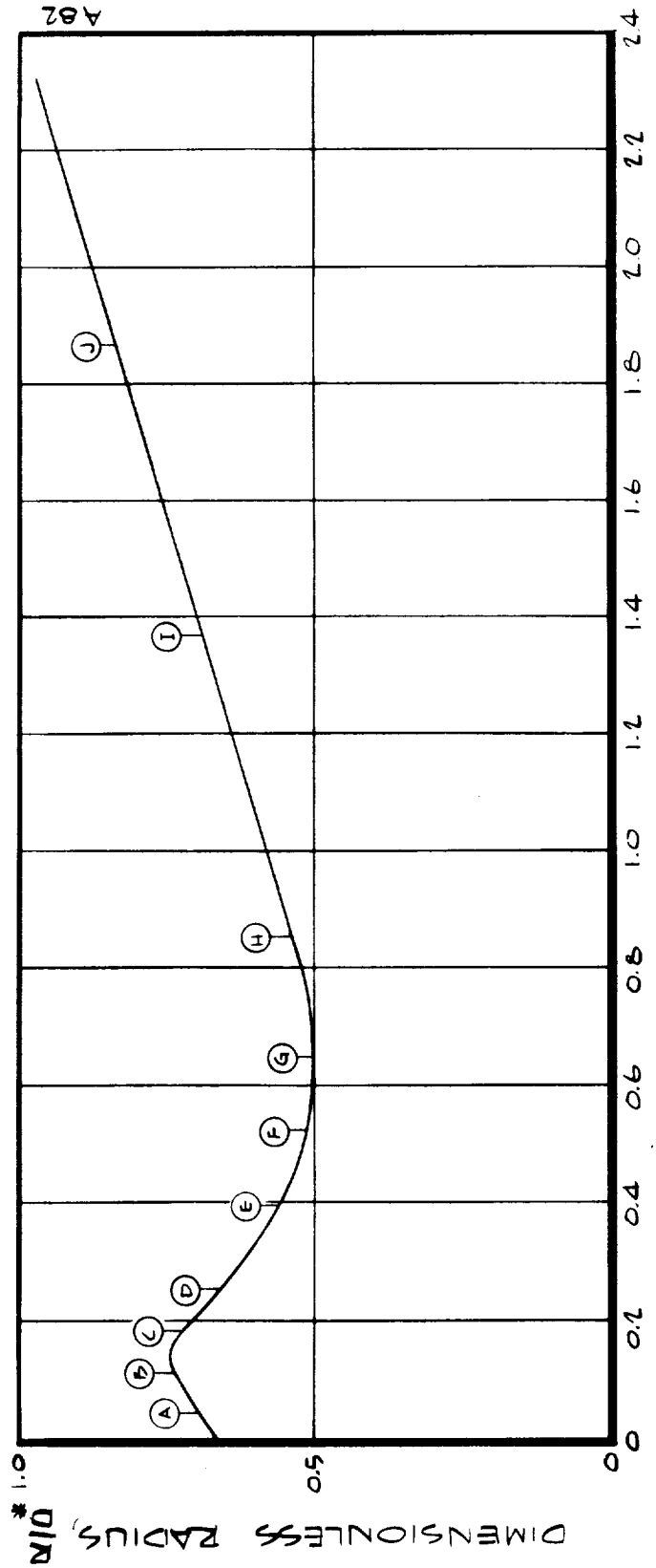

FIGURE 2-7 VARIATION OF NOZZLE RADIUS WITH BOUNDARY LAYER RUNNING LENGTH.

2. Within a given azimuthal plane, the state of the boundary layer edge medium is isentropically related to the state of the edge medium at the unity Mach number condition appearing in that plane. That is, the boundary layer edge entropy level is a function of nozzle azimuth and web fraction, independent of surface coordinate. However, this assumption does not exclude the consideration of flow irreversibilities which are known to exist due to flow separation off the end of the propellant grain, for example.

Certain other assumptions will be indicated later in relation to the estimation of boundary layer behavior. The estimation of the variation of $\tilde{\rho u}$ within the nozzles (and thence, all boundary layer edge conditions for a given chamber pressure) is presented in the following subsections.

2.3.1.1.1 Region upstream of the Throats

Mach number variations with nozzle location and simulated web fraction were obtained from cold flow test results obtained by NASA Lewis Research Center (References 2-8 through 2-10). These results were used directly for positions in the nozzle between the reentrant nozzle leading edge and nozzle throat, in the form of nondimensional mass fluxes calculated from the following relation (reciprocal of the isentropic one-dimensional Mach number-area ratio relation)

$$\tilde{\rho u} = \frac{M}{\left[\frac{2}{\gamma+1}\left(1 + \frac{\gamma-1}{2} M^2\right)\right]^{(\gamma+1)/2(\gamma-1)}} \qquad (2\text{-}2)$$

where the Mach numbers in Equation (2-2) are those reported in Reference 2-9 (or Reference 2-8) and $\gamma = 1.4$ (the cold flow test medium is air). These experimental Mach numbers presume knowledge of the following <u>local</u> parameters

static pressure
stagnation pressure
flow direction (in order to measure the true local stagnation pressure).

From the propellant grain geometry in relation to the nozzle, and from the work of Reference 2-11, it is estimated that a local variation of stagnation pressure in excess of 5 percent is likely to have existed for the $\tau = 0$ grain simulation in the cold flow tests. According to Reference 2-12, local static and stagnation pressures were measured (p_t varying by about 5 percent) during these experiments; however, the local flow directions were not reported. The local boundary layer edge mass fluxes which might be interpreted from the reported Mach numbers are highly sensitive to inaccuracies in the measurements of local static and stagnation pressures. This was briefly studied as shown

in Figure 2-8 where it was found (for example) that a 5-percent uncertainty in the interpreted experimental stagnation pressure results in a change in boundary layer edge mass flux by as much as 43 percent ($\Delta\tilde{\rho u} = .43$) of that which occurs at unity Mach number (where $\tilde{\rho u} = 1.0$).

These and other considerations prompted the decision to employ cold flow results obtained upstream (in terms of λ) of the nozzle leading edge only as qualitative guides for the estimation of the actual conditions.

The cold flow results were obtained for two simulated web fractions, $\tau = 0$ and 0.34. In the following paragraphs, the methods employed for the estimation of $\tilde{\rho u}$ upstream of the throats for all web fractions is presented. The shape and location of the stagnation line and some of the consequent simplifications will be discussed first. Certain general considerations of the behavior of the flow field within a solid propellant motor will then be indicated to provide justification for the final flow field variations assumed.

Based on the cold flow information available, it was not possible to establish the shape or location of the stagnation line occuring on the reentrant nozzle. The stagnation line establishes the origin of the boundary layer development on the nozzle, and is therefore by definition at $\lambda = 0$. The stagnation line was assumed to be independent of nozzle azimuth, and its location was assumed to be as indicated in Figure 2-3 and 2-5 by the origins of λ. Other experimental information of potential utility but not available were locations of boundary layer separation (if any), or regions of reverse flow. For example, on the outside (underside) of the nozzle it is not known if the nozzle boundary layer edge flow is in the direction of positive λ, which is the direction assumed.

The analysis consisted primarily of the estimation of the variation with web fraction of $\tilde{\rho u}$ at certain critical locations (λ/D_*) along the nozzle. One of these critical locations is station B on the outside of the nozzle, another being point C which is the nozzle leading edge. Due to lack of information to the contrary, it has been simply assumed the $\tilde{\rho u}=0$ at $\lambda = 0$ and varies linearly between $\lambda = 0$ and λ_B, and between λ_B and λ_C.

The magnitudes of surface velocities (or mass fluxes) induced in the vicinity of the nozzle entrance due to flow through the nozzle are dependent upon the location of the stagnation line and nozzle approach velocities, both of which are influenced by the grain geometry in relation to the nozzle. It is convenient to estimate for later use the nozzle approach mass flux which is the grain exit mass flux. Mass continuity requires:

$$(\tilde{\rho u})_{\text{grain exit}} = \frac{A_*/A_p}{1 + \delta} \qquad (2\text{-}3)$$

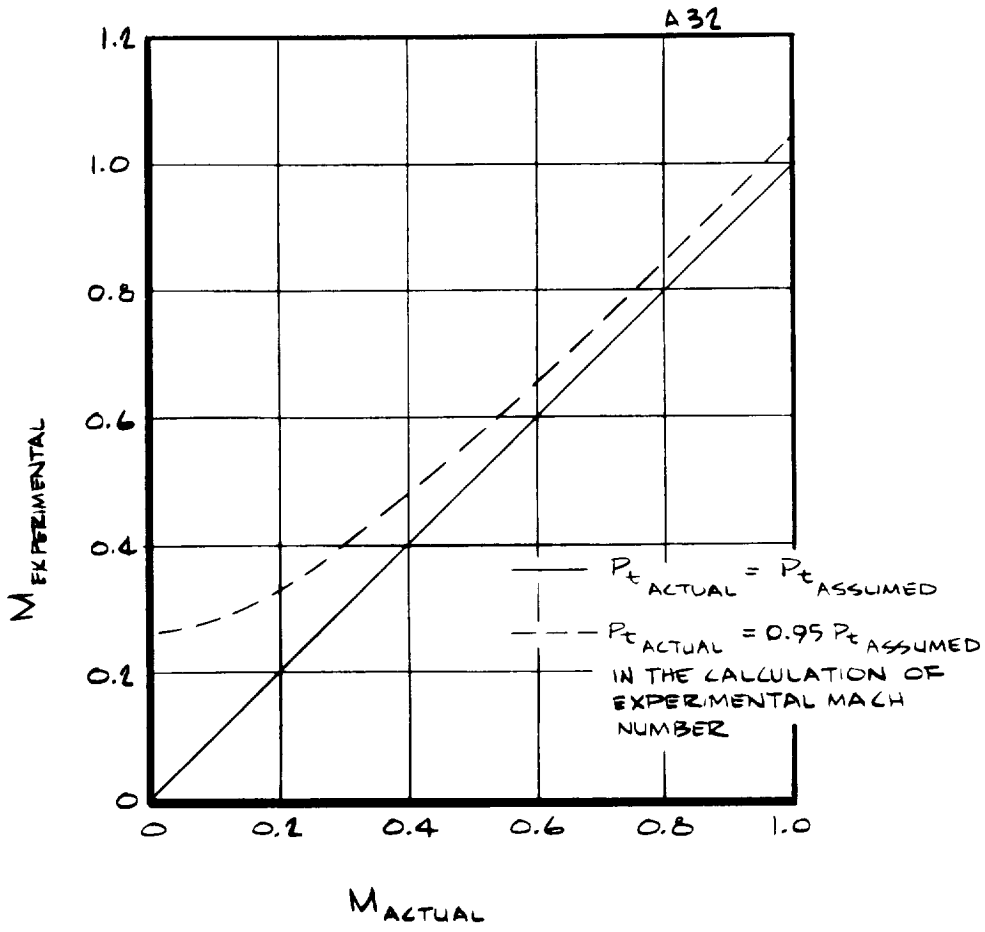

a) MACH NUMBER SENSITIVITY

FIGURE 2-8 COLD FLOW DATA SENSITIVITY TO STAGNATION PRESSURE UNCERTAINTY

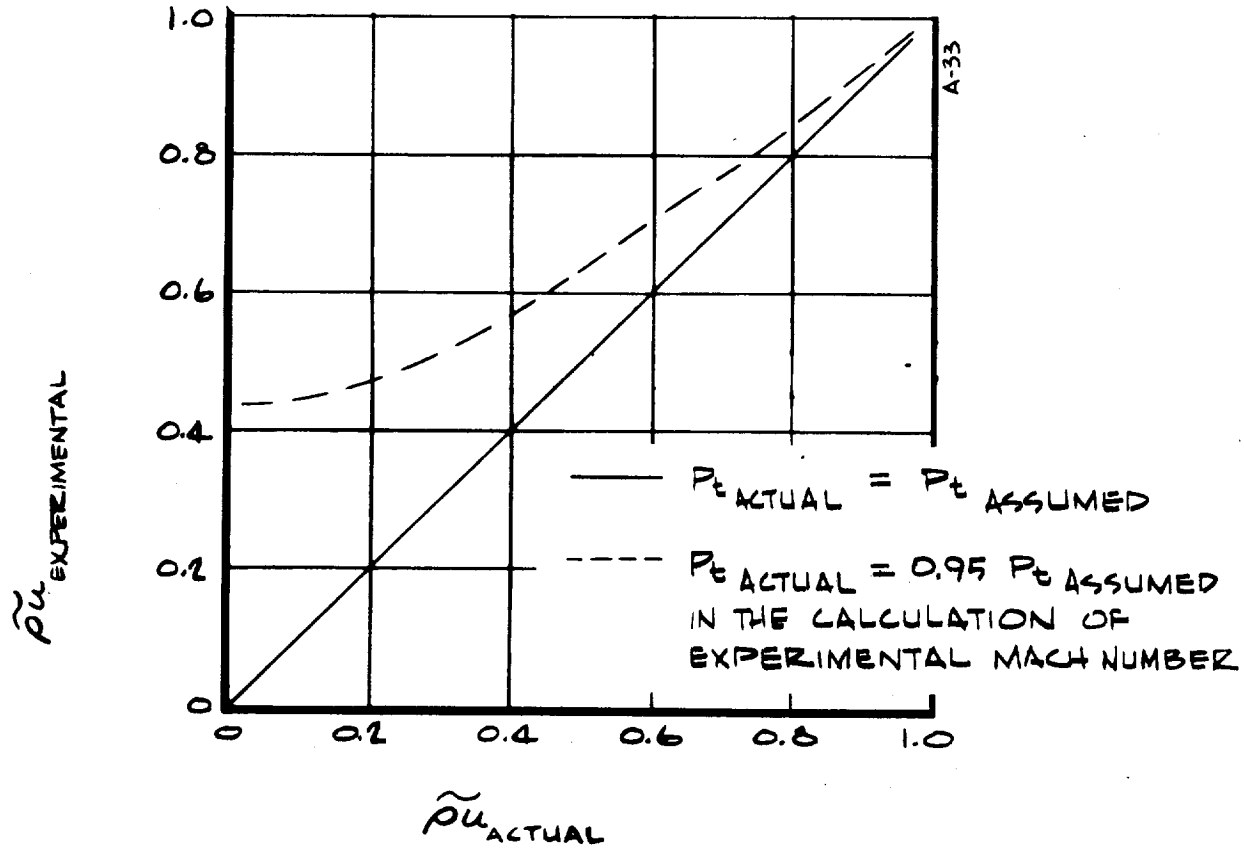

b) SURFACE MASS FLUX SENSITIVITY

FIGURE 2-8 CONCLUDED

where

$$\delta = \frac{\text{grain cutback propellant mass evolution}}{\text{grain perforation mass evolution}}$$

A_p = grain port cross section area

For an "ideal" grain where its port perimeter is independent of web fraction, the grain port flow area varies as

$$A_p = A_{po} + (A_{case} - A_{po})\ \tau$$

(where A_{po} is the port area at $\tau = 0$) such that the "ideal" grain exit mass flux variation is

$$(\tilde{\rho u})_{\text{grain exit}} = \frac{A_* / A_{po}}{(1+\delta)\left[1 + \left(\frac{A_{case}}{A_{po}} - 1\right)\ \tau\right]} \tag{2-4}$$

Even for an infinitely large chamber cavity, flows would be induced along the reentrant surface. The surface mass fluxes at any web fraction can be idealized as consisting of two parts: 1) that distribution that would exist for an infinitely large chamber plus 2) a perturbation (large or small) due to the proximity of the grain and its exit mass flux. From the form of Equation (2-4) it might be supposed that the perturbation mass fluxes might decay as

$$\frac{1}{\text{const} + \text{const} \times \tau} \tag{2-5}$$

which is the form assumed here.

The specific variations employed in this analysis (approximately consistent with the analysis of Reference 2-13) which have not already been specified are

1. points B

   $(\tilde{\rho u})_B = \frac{0.37}{1 + 2.5\tau}$ (independent of nozzle azimuth, and approximately equal to grain exit mass flux, Equation (2-4))

2. points C to the throat

   $\theta = 0$; from Equation (2-2) through direct use of the cold flow results, independent of τ

   $\theta = 60$;

   $(\tilde{\rho u})_{60^\circ} = (\tilde{\rho u})_{0^\circ} + f(\tau)\ f\left(\frac{\lambda}{D_*}\right)$

where $f(\tau) = \frac{1}{1+10\tau}$

$$f\left(\frac{\lambda}{D_*}\right) = \left[(\tilde{\rho u})_{60^\circ} - (\tilde{\rho u})_{0^\circ}\right]_{\tau=0} \quad \text{(see Figure 2-9)}$$

The functions $f(\tau)$ and $f(\lambda/D_*)$ have been obtained from evaluations of the cold flow data, the former function resulting from data at point C for the two simulated web fractions.

These resulting mass flux variations are presented in Figure 2-10 for the two azimuths being defined by the position behind the grain lobes ($\theta = 60^\circ$), and between lobes ($\theta = 0^\circ$). For convenience and where appropriate, mass fluxes obtained from one dimensional theory are also presented.

2.3.1.1.2 Downstream of the throats

The variation of $\tilde{\rho u}$ downstream of the throats was estimated with the aid of two simple theories, and the experimental data of Reference 2-14. The first theory was applied to the region immediately downstream of the throat. It assumes that the local value of $\tilde{\rho u}$ is that obtained through evaluation of Equation (2-2) employing the Mach numbers obtained by a Prandtl-Meyer turn from unity Mach number. The turning angle is the local slope of the nozzle surface and the theory is applied between the throat and the point where the throat section blends into the conical region of the nozzle. Results obtained from this theory were compared very favorably with the experimental data of Reference 2-14.

The second theory assumes that the local mass flux can be predicted by one-dimensional theory in regions reasonably far removed from the throat. The definition of "reasonably far removed" was determined from the data of Reference 2-14 and these data were also used to estimate values of $\tilde{\rho u}$ which blend between the two regions where the theories are applied. These estimated values of $\tilde{\rho u}$ are presented in Figure 2-10, where results from one-dimensional theory are also presented.

2.3.1.2 Boundary Layer Analysis

Consideration was given here only to the energy boundary layer. Its consideration according to the energy integral method presented in Reference 2-5 resulted in the estimation of the spatial and temporal variations of nozzle "nonablating wall" heat transfer coefficients. "Nonablating wall" mass transfer coefficients were assumed to be equal to 95 percent of the heat transfer coefficients, based on an assumed Lewis number of 0.93 and the "similiarity" relationship, $C_M = C_H\,(Le)^{2/3}$ (these assumptions are discussed

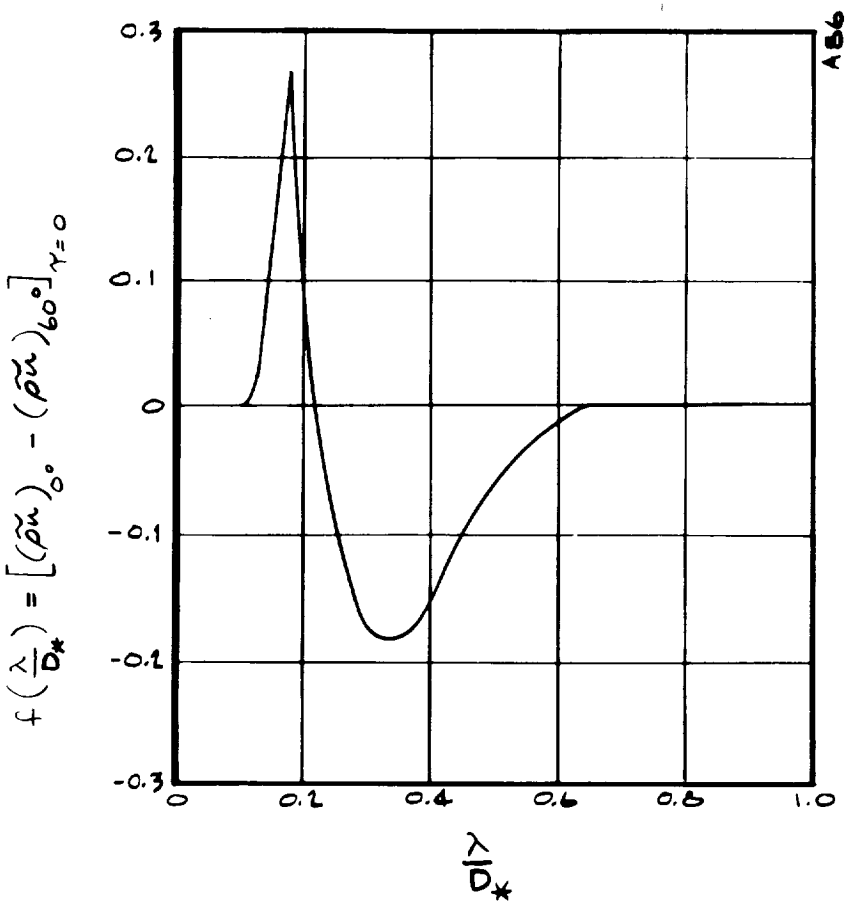

FIGURE 2-9 MASS FLUX ASYMMETRY FUNCTION

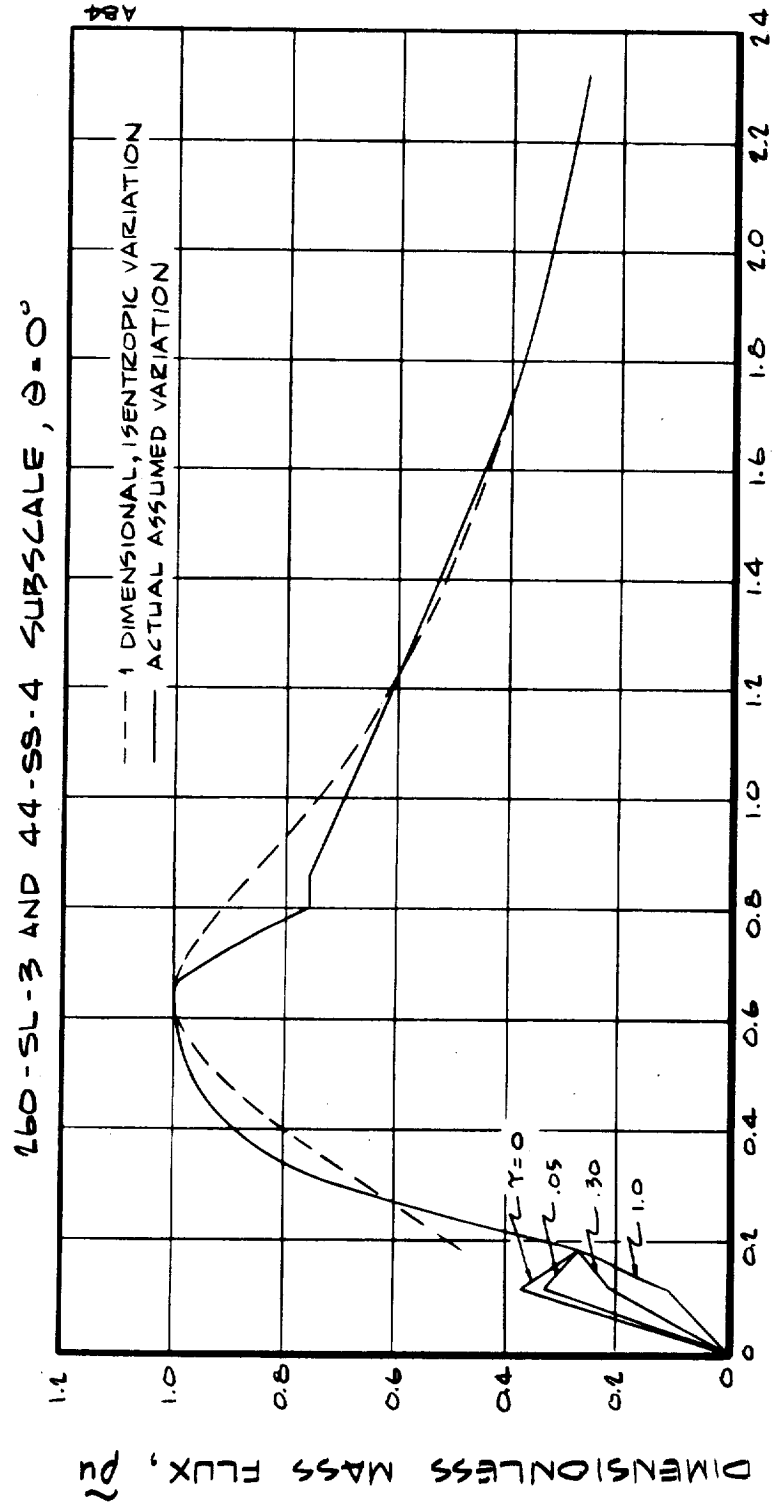

a) $\theta = 0°$, BETWEEN LOBES

FIGURE 2-10 ASSUMED BOUNDARY LAYER EDGE MASS FLUXES

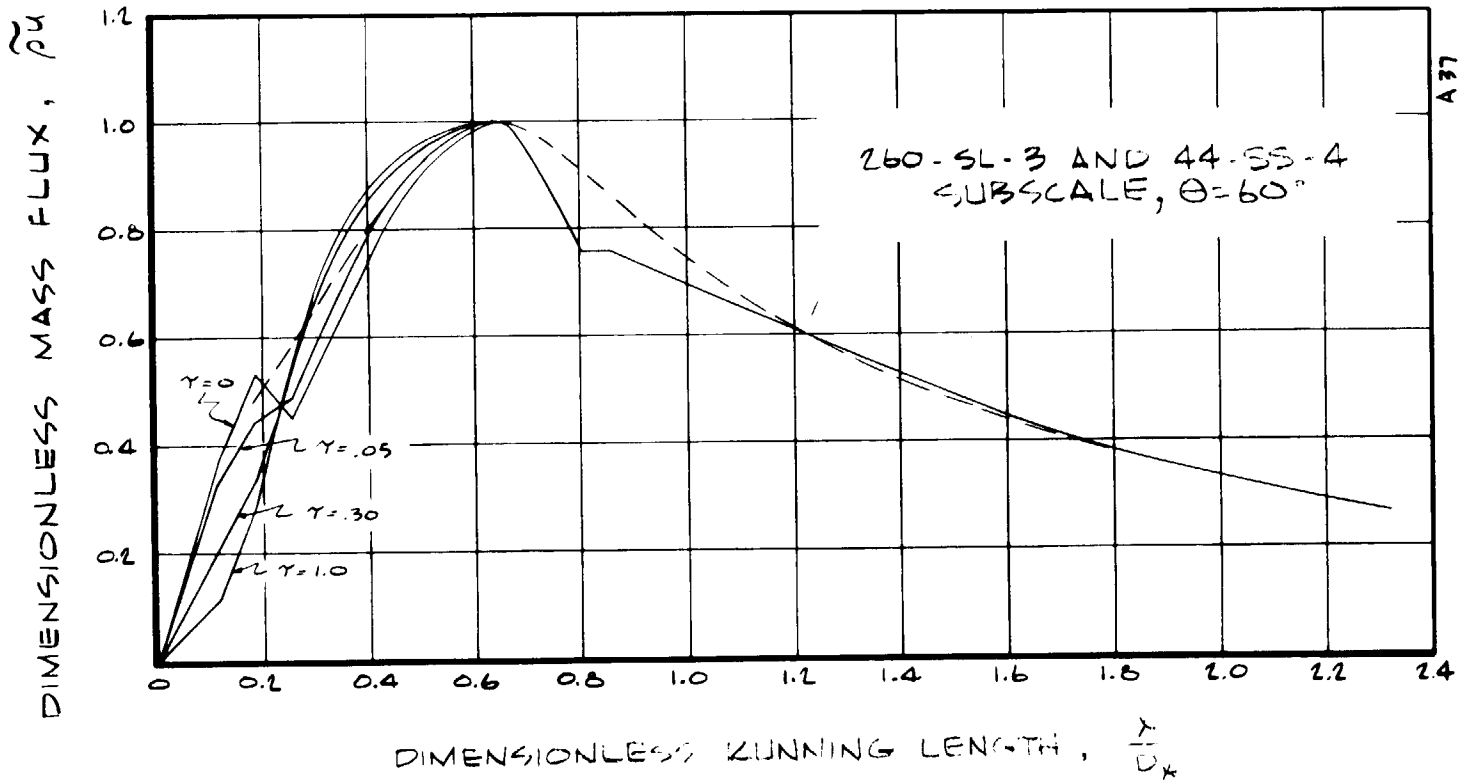

b) $\theta = 60°$ BEHIND LOBES

FIGURE 2.10 CONCLUDED

further in Section 4).

Certain of the assumptions and simplifications employed in the boundary layer analysis (aside from those employed in the development of the method) are as follows:

1. The boundary layer is turbulent over its length, its origin being at $\lambda = 0$ (Figures 2-3 and 2-5).
2. Within the azimuthal planes considered it is presumed that the boundary layer behaves as if the flow were axisymmetric.
3. The influence of ablation on boundary layer behavior is ignored (improvements detailed in appendix A of Reference 2-2 would obviate this simplification).
4. The local boundary layer edge velocity, and static temperatures and pressures are those obtained for an equilibrium isentropic expansion of the propellant from the chamber condition to the local subsonic or supersonic values of $\tilde{\rho u}$ presented in Figure 2-10.
5. It is presumed that propellant condensed phases do not penetrate the boundary layer, and the properties within and at the edge of the boundary layer are those of the propellant gases alone.
6. The recovery factor is equal to unity. This assumption in combination with 5 above yields a "gas alone" recovery enthalpy which varies with edge velocity, although the gas-plus-condensed-phase recovery enthalpy is invariant.

With the above assumptions along with the simplification that the magnitude of $\rho u/p_c$ at a given value of $\tilde{\rho u}$ is independent of chamber pressure, p_c, the boundary layer method yields the following functional relationship for heat transfer coefficient

$$\rho_e u_e C_H \propto f\left(\frac{\lambda}{D_*}, \theta, \tau, t_b\right) \frac{p_c^{0.8}}{D_*^{0.2}} \qquad (2\text{-}6)$$

The burn time, t_b, influence the λ variation of wall enthalpy at a given web fraction. The upstream and local variations of wall enthalpy influence the local value of the heat transfer coefficient.

Heat transfer coefficients have been predicted for the nozzles indicated in Figures 2-3 and 2-5 scaled to a throat diameter of one foot for convenience. Calculations were performed for one chamber pressure (500 psia), four web fractions ($\tau = 0, 0.05, 0.3, 1.0$), two azimuths ($\theta = 0$, 60 degrees), while employing a mix of four wall enthalpy distributions appropriate to the real times associated with these web fractions for the subscale and full-scale motors. Approximate nondimensional results for both the subscale and full scale motors (within about plus or minus 3 percent of the actual results) are presented in Figure 2-11 for the various prediction locations and for the range of web

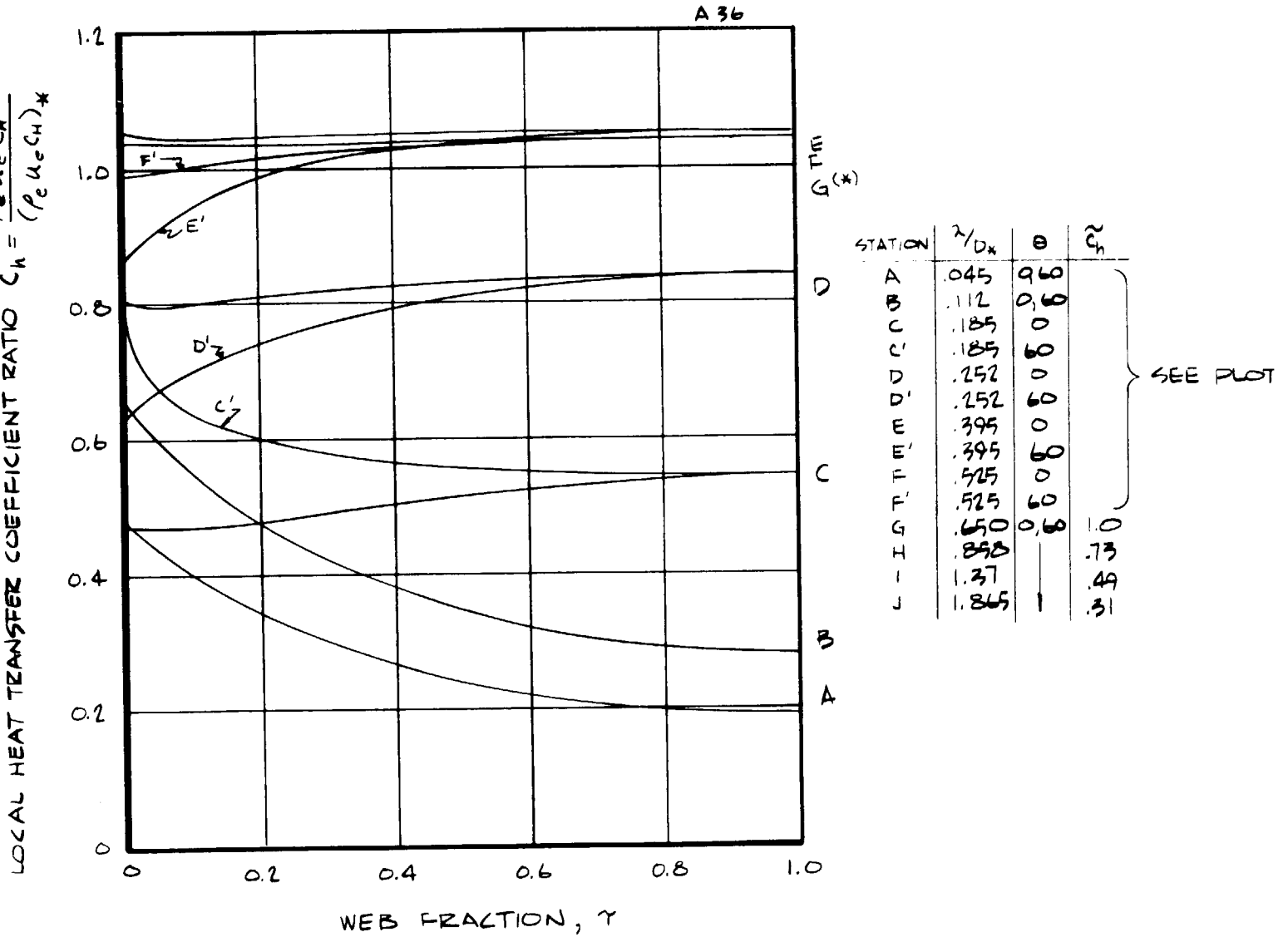

FIGURE 2-11 NON-DIMENSIONALIZED HEAT TRANSFER COEFFICIENTS FOR THE SUBSCALE & FULL SCALE MOTORS.

fractions considered. The predicted time variation of throat heat transfer coefficients for both motors is presented in Figure 2-12, which includes consideration of the actual throat sizes and the chamber pressure histories of Figures 2-2 and 2-4.

2.3.2 Estimated Experimental Flow Field Behavior for the 44-SS-4 Motor

A post-fire evaluation of the subscale motor ablative material behavior was performed in several areas, one being the interpretation of the actual flow field behavior as evidenced by the material response. As discussed in Section 2.4, the material behavior between the propellant lobes upstream of the throat was not accurately predicted. This poor prediction could not be rationalized on the basis of a bad estimate of the heat and mass transfer coefficients as influenced by the boundary layer behavior. That is, the magnitude and distribution of the material erosion prediction deficiency between the grain lobes was believed to be caused by an erosion mechanism not considered in the predictions.

Because of the location of the prediction deficiency, the presumption of propellant condensed phase interaction with the nozzle material was warranted. The interaction was not considered in the initial predictions because the possibility of appreciable propellant condensed phase contact with the wall was ruled out as described below.

Consider the following sketch of the flow field behavior hypothesized for the predictions. It was presumed that the flow along the nozzle wall

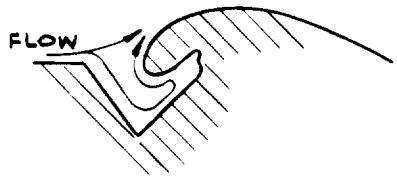

A93

would be in the direction of positive λ at all nozzle azimuths. If this was so, it might be expected that condensed phases within the stream would be deflected away from the nozzle leading edge because of the flow along the wall. The above sketch presumes a location of the stagnation line in the vicinity of $\lambda = 0$. In the regions behind the grain lobe the observed cold flow behavior was approximately as sketched. It was known, however, that flow leaving the grain exit in the between lobe azimuth was deflected behind the grain lobe because of its reduced base pressure (see Figure 2-6). In retrospect, it is likely that at $\theta = 0$, the flow behavior was such as to yield a stagnation point near the nozzle leading edge, as in the following sketch. The flow configuration in this sketch does not have the shielding

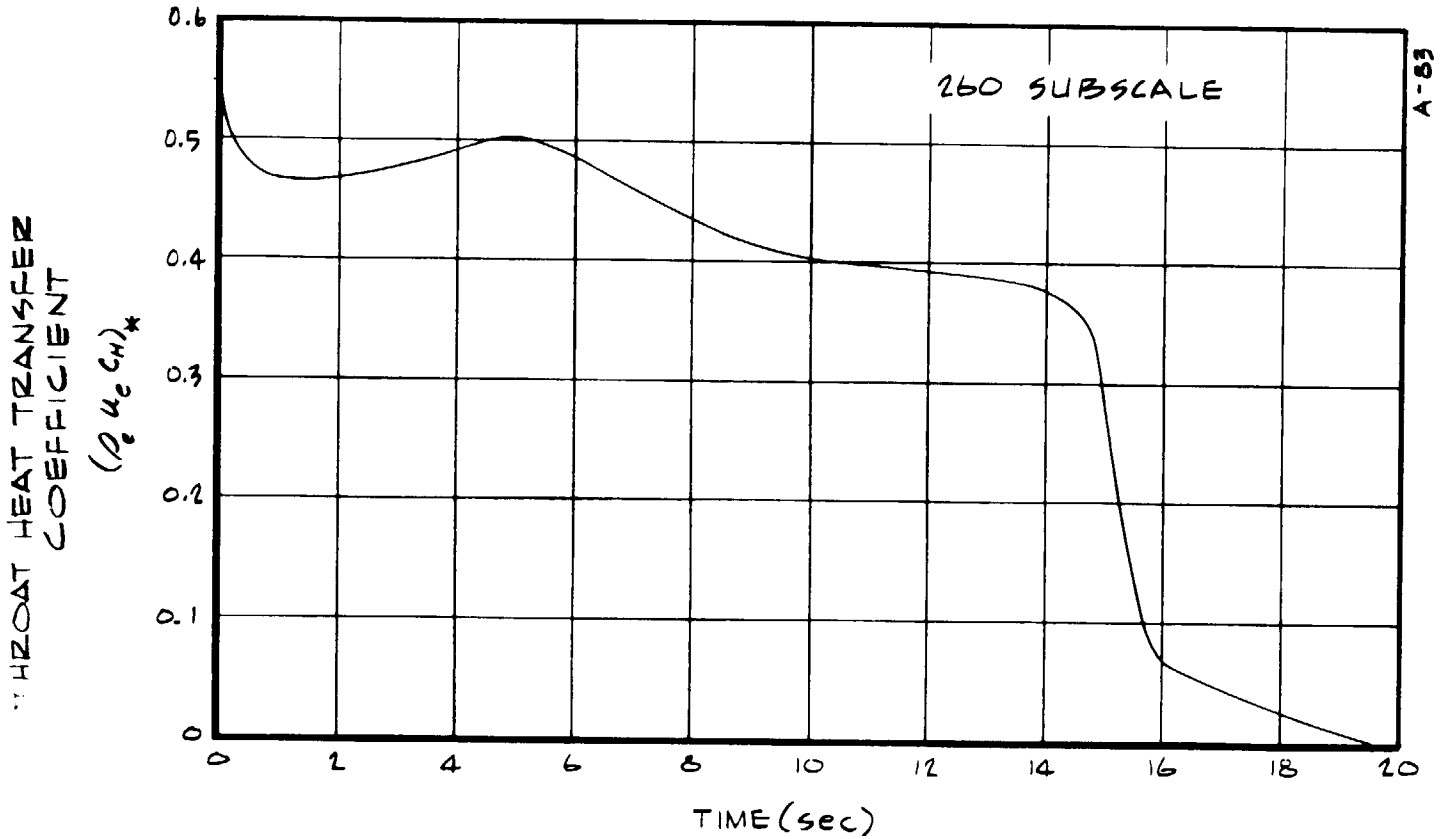

a) 44-55-4

FIGURE 2-12 ESTIMATED THROAT HEAT TRANSFER COEFFICIENT

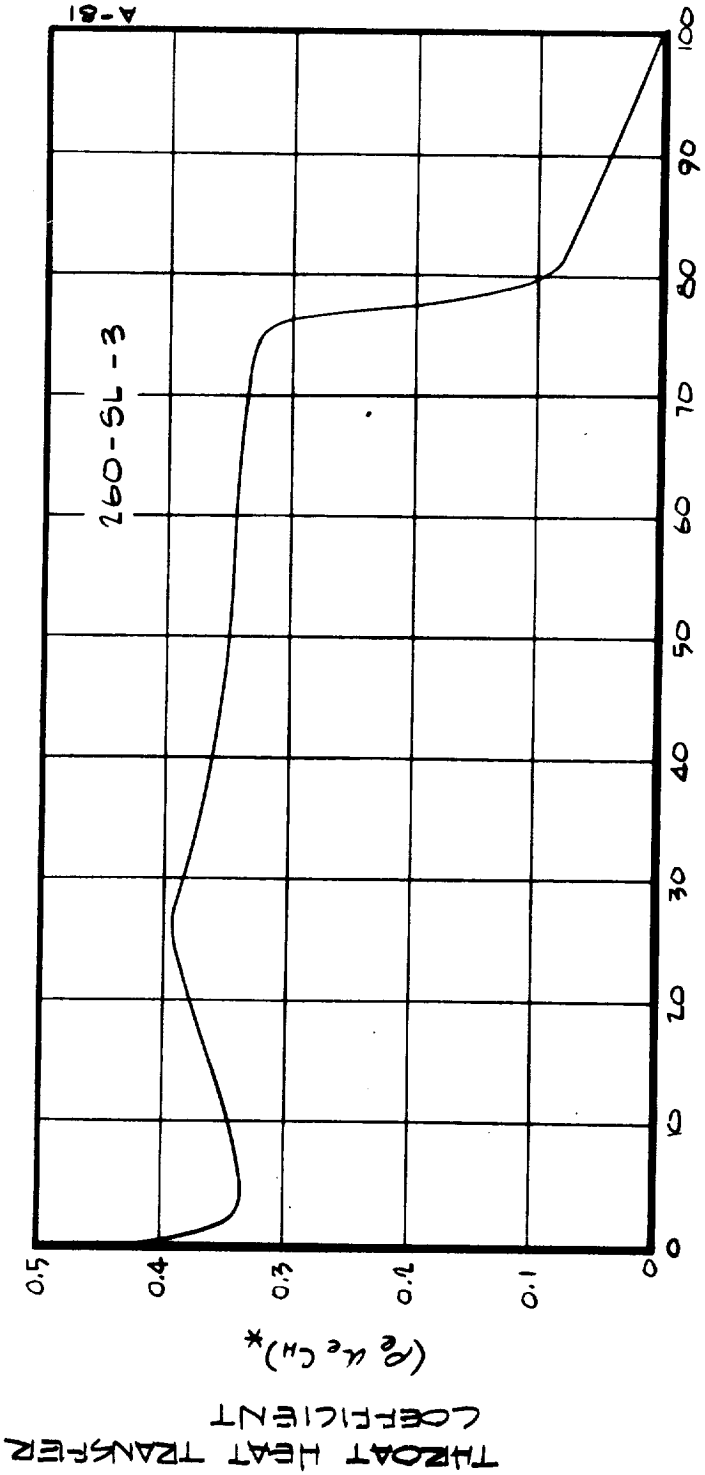

b) 160-SL-3

FIGURE 2-12 CONCLUDED

flow in the vicinity of the leading edge, and propellant condensed phase might be expected to deposit on the wall with a "collection efficiency" likened to a cylinder in particle-laden cross flow. Previous experience with reentrant nozzles behind circular grain ports has shown the nozzle material behavior to be predictable without consideration of propellant condensed phase-nozzle wall interaction. It is believed that the flow field behavior at certain azimuths behind noncircular grain ports at early burn times can be (and was) as described in the latter sketch, the flow behind circular ports or non-circular ports at late burn times* being more like that in the former sketch.

Thus, the prediction deficiency at $\theta = 0^{\circ}$ is attributed to a propellant condensed phase - nozzle wall interaction not considered. The actual surface recession mechanism is discussed in Section 2.4.

2.4 PREDICTIONS OF MATERIAL PERFORMANCE

Predictions of material performance in terms of surface and in-depth ablation and thermal response were made for both the 44-SS-4 and 260-SL-3 nozzles. The prediction locations were presented previously in Figures 2-3 and 2-5 and Tables 2-1 and 2-2. At calculation locations for which the flow field was circumferentially non-uniform due to the grain port configuration (C through F), two predictions were made, one corresponding to the between-propellant-lobes position, and the other to the behind-propellant-lobes position.

Preliminary predictions were first made for both nozzles prior to the 44-SS-4 motor firing. A post-fire analysis of the 44-SS-4 nozzle material performance, primarily through comparison with the predicted performance, provided the basis for updated predictions at some of the locations in the 260-SL-3 nozzle. For all but four of the 14 prediction locations, these final predictions were performed prior to the 260-SL-3 firing. For the other four locations, the final predictions were performed in two steps because of time limitations before the 260-SL-3 motor firing. The predictions at these four locations were first estimated prior to the 260-SL-3 firing and then performed in greater detail immediately after the firing. A brief post-fire analysis of the 260-SL-3

* Times greater than about 1/3 of web time, based on the nearly symmetrical flow field results for these late times in Figure 2-10.

nozzle material performance was also performed. These predictions and the results of the post-fire analyses are presented in the following sections, Sections 2.4.1 covering the 44-SS-4 nozzle and Section 2.4.2 the 260-SL-3 nozzle.

2.4.1 44-SS-4 Nozzle Predictions and Post-Fire Analysis

The material performance predictions for the 44-SS-4 nozzle and their comparison with the measured performance are presented in Table 2-5 and Figure 2-13. The agreement between the measured and predicted performance is seen to be unfavorable. The measured recession was actually negative at supersonic area ratios greater than about 1.5 and was very large in the nose region between propellant lobes. A detailed post-fire analysis was therefore performed to define the cause of the discrepancies between measurement and prediction so that the appropriate phenomena could be incorporated in the final predictions for the 260-SL-3 nozzle.

The first potential explanation considered was a difference between the assumed and the actual chamber pressure history. The actual chamber pressure was slightly higher and the firing time slightly shorter than that shown in Figure 2-4 and assumed in the predictions. These differences tended to be self compensating and were small so that their effect on the predicted performance can be ignored.

Two other phenomena were then investigated and determined to provide the probable explanation of the discrepancy between measured and predicted performance. These were char layer warp or swelling as explaining the small and negative measured surface recession in the "exit-cone", and particle deposition as explaining the large recession in the nose region. The char layer warp results in a change in the layup angle in the char region, either during the firing or after shutdown, which in turn results in an apparently lower surface recession than actually occurred. This char layer warp is illustrated in the sketch below and is discussed in Reference 2-2. Swelling in the char

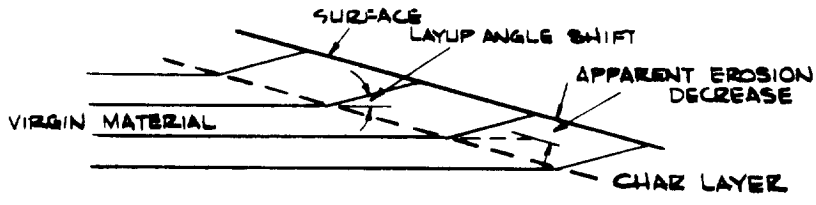

TABLE 2-5

MATERIAL PERFORMANCE PREDICTIONS FOR THE 44-SS-4 NOZZLE AND COMPARISON WITH MEASUREMENT

Location	A/A_*	Material	Surface Recession (in)		Char Depth [a] (in)	
			Predicted	Measured	Predicted	Measured
A	- underside	FM5131 Silica Phenolic	0.088	-	0.312	-
B	- underside		(0.137) [b]	-	0.295	-
C-0°	-2.00 nose leading edge	MX4926 Carbon Phenolic	0.040	0.143	0.58	0.50
C-60°			0.047	0.060	0.59	
D-0°	-1.80		0.071	-	0.418	-
D-60°			0.061	-	0.361	
E-0°	-1.26		0.093	0.090	-	0.32
E-60°			0.090	0.056	-	
F-0°	-1.06		0.092	0.073	0.398	0.33
F-60°			0.091	0.050	0.397	
G	1.0		0.085	0.046/c 0.030		0.36
H	1.15		0.054	-	0.364	-
I	1.90		0.027	-	0.337	-

a) Referenced to original surface.

b) Predictions made for silica phenolic prior to design change to carbon phenolic.

c) $0°/60°$.

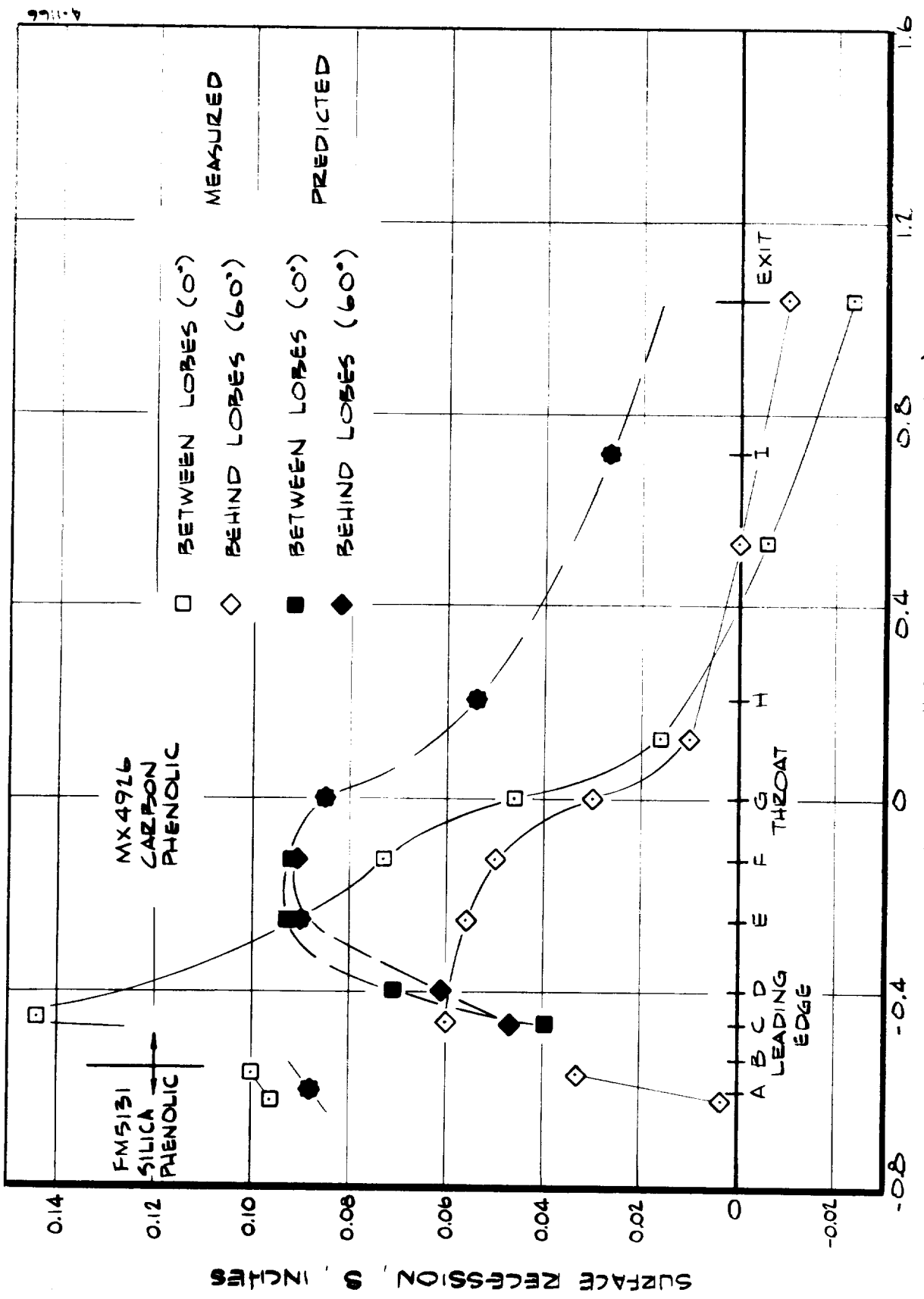

FIGURE 2-13 COMPARISON OF MEASURED AND PREDICTED SURFACE RECESSION FOR THE 44-SS-4 NOZZLE, INITIAL PERTURBATION.

layer or pyrolysis zone is a similar phenomenon that also results in an apparently lower surface recession than actually occurred. To account for the char layer warp or swelling quantitatively, three different assumptions were made:

(1) Apparent recession decrease due to warp or swelling proportional to char depth

(2) Apparent recession decrease due to warp or swelling proportional to char thickness

(3) Apparent recession decrease due to warp caused by a constant layup angle shift across thickness of the char.

These were applied to the measured and predicted surface recession results for the 44-SS-4 nozzle by requiring close agreement between the recessions in the supersonic region of the nozzle (in the vicinity of Location I, Figure 2-5). The predicted char depths and thicknesses were used in all cases. Based on the analysis of results, the following relations for the recession decrease were found:

$$s_{warp} = 0.105\ \delta_{char} \tag{2-7}$$

$$s_{warp} = 0.135\ \tau_{char} \tag{2-8}$$

$$\theta_{warp} = 9\text{-}1/2^{\circ} \tag{2-9}$$

where the three equations correspond respectively to the above assumptions and δ_{char} is the char depth, τ_{char} is the char thickness, and θ_{warp} is the layup angle shift. The net surface recession is given by

$$s_{net} = s_{calculated} - s_{warp} \tag{2-10}$$

where s_{warp} is given above (assumptions (1) and (2)) or is calculated from the char thickness, layup angle, and warp angle (assumption (3)). The first two assumptions yielded essentially the same net surface recession at each location; the comparison of measured and predicted recession is shown in Figure 2-14 for the entire nozzle. In the submerged portion of the nozzle, only the behind-lobes (60°) results are presented. Also for location C, the surface recession decrease due to warp was assumed zero since the layup angle referenced to the surface was 90° and therefore any warp would have a negligible affect on the measured surface recession; note that the layup angle referenced to the surface was much less than 90° for all other locations. From Figure 2-14, the comparison of measured and predicted surface recession is now quite favorable throughout the nozzle. The warp correction resulted in a decrease in the calculated recession of about 40 mils at all locations. The comparison

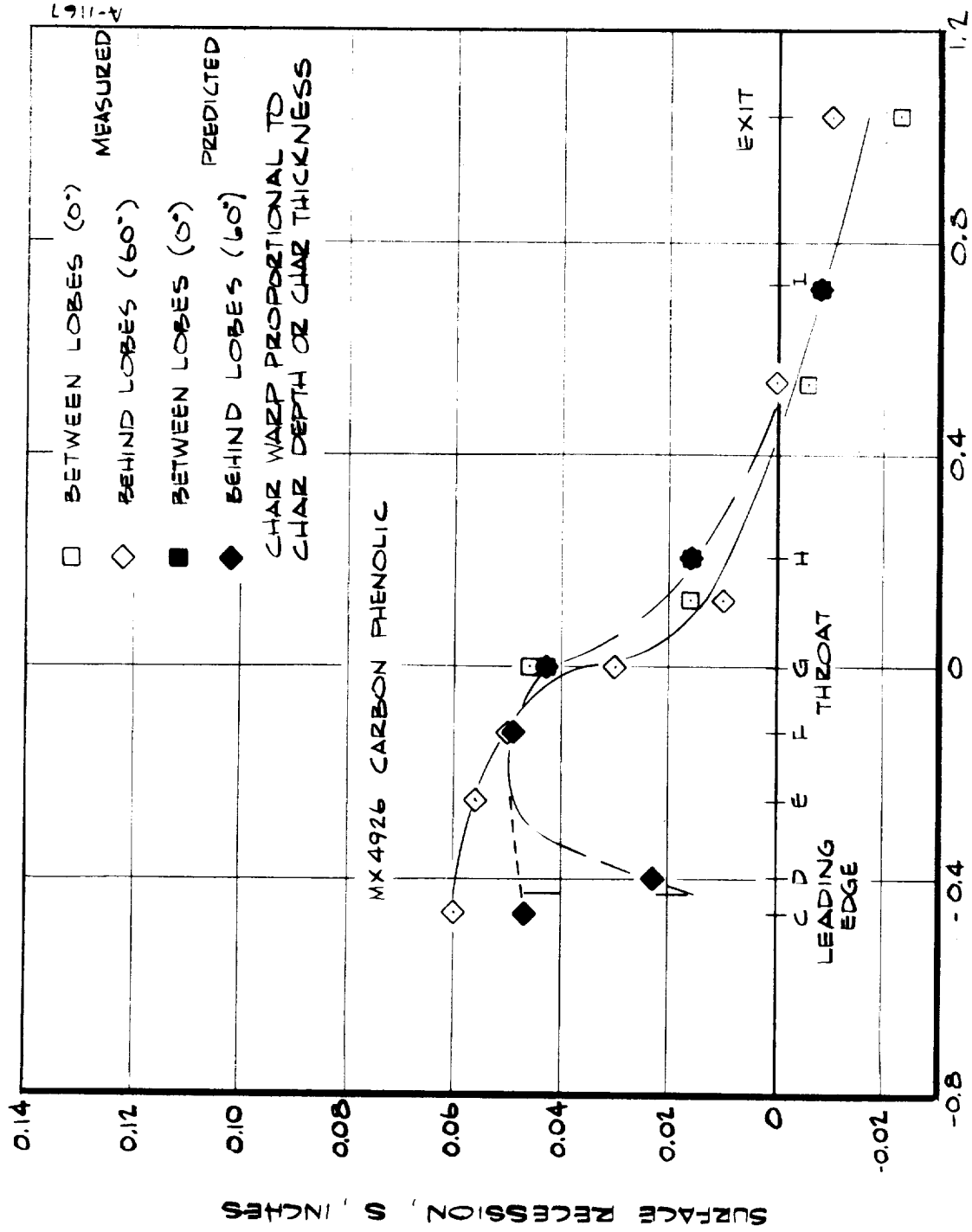

FIGURE 2-14 PREDICTED SURFACE RECESSION INCLUDING CHAR WARP CORRECTION (EQUATIONS (2-7) AND (2-8)) AND COMPARISON WITH MEASUREMENT FOR THE 44-SS-4 NOZZLE

for the angle correction approach, assumption (3), is presented in Figure 2-15 and exhibits a somewhat less favorable agreement between measurement and prediction.* On this basis and because of the simplicity of the char depth approach, assumption (1), this method was used in the final predictions for the 260-SL-3 nozzle.

The phenomenon which is felt to explain the large surface recession between propellant lobes in the nose region is particle deposition. The Al_2O_3 particles (actually droplets at chamber conditions) flow down the propellant grain and, because of their momentum and the low gas-phase mass flux around the nose at the between lobes locations, deposit on the material surface in the nose region as disucssed in Section 2.3. Note that this particle deposition phenomenon apparently is not significant at the behind-lobes region. This effect is apparently directly related to the asymmetric grain port since no particle deposition effects were observed in firings of submerged nozzles for which the propellant grain port was circular (e.g., Reference 2-15).

The possible mechanisms which cause surface recession due to particle deposition fall into two basic categories, mechanical abrasion and chemical reactions. Since chemical reactions would certainly be expected to occur even in the presence of mechanical effects, this mechanism was considered first. Calculations were performed for the steady state ablation of carbon phenolic at conditions typical of the nose region and with varying Al_2O_3 particle deposition rates. The calculated surface recession response as a function of particle deposition rate is presented in Figure 2-16. Two curves are presented: the first corresponds to steady state conditions** and the second corresponds to conditions typical of the early part of the firing (pseudo-transient) for which the char and pyrolysis zone recession rates are higher than the surface recession rate. For a dimensionless deposition rate $\dot{m}_p/\rho_e u_e C_M$ of 10 the recession rate is about 50 mils/sec, this corresponding to only approximately 4 percent of the total particle mass flux ($lb/ft^2 sec$) in the stream. On this basis, the chemical model of surface recession due to particle deposition certainly seems reasonable and in itself can explain the measured recession in the nose region of 44-SS-4 nozzle. This discrepancy between measured and predicted surface recession in the nose region of the 44-SS-4 nozzle (Figure 2-13) is therefore felt to be due to chemical reactions associated with particle deposition. The actual particle deposition rates can and should be quantified through further flow field analyses, and the material

*Note that the magnitude of this assumption (3) correction is a function of both layup angle and char thickness, not char thickness only as in assumption (2).

**Steady state implies that the surface, char, and pyrolysis zone penetration rates are all equal.

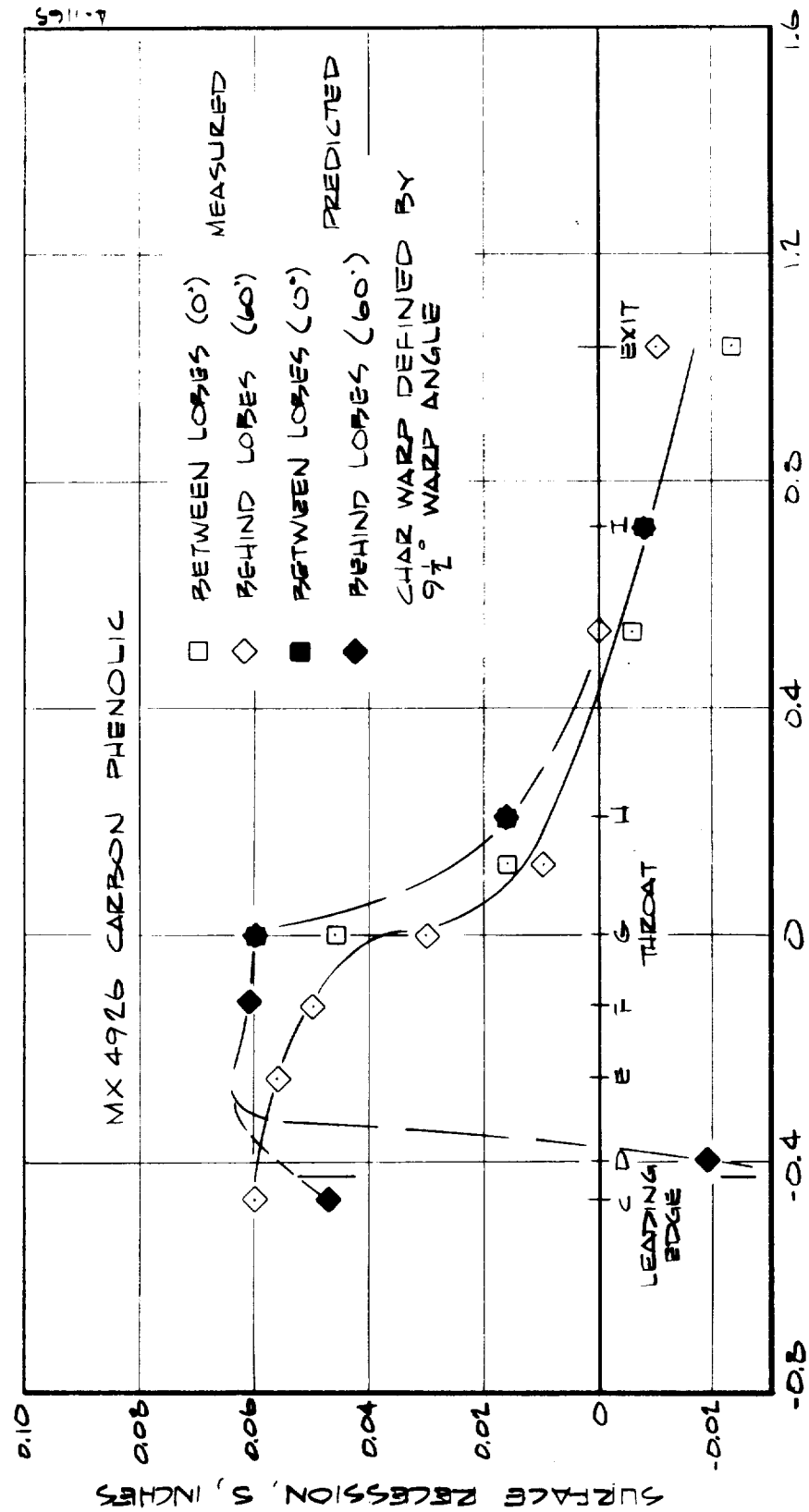

FIGURE 2-15 PREDICTED SURFACE RECESSION INCLUDING CHAR WARP CORRECTION (EQUATION (2-9)) AND COMPARISON WITH MEASUREMENT FOR THE 44-SS-4 NOZZLE

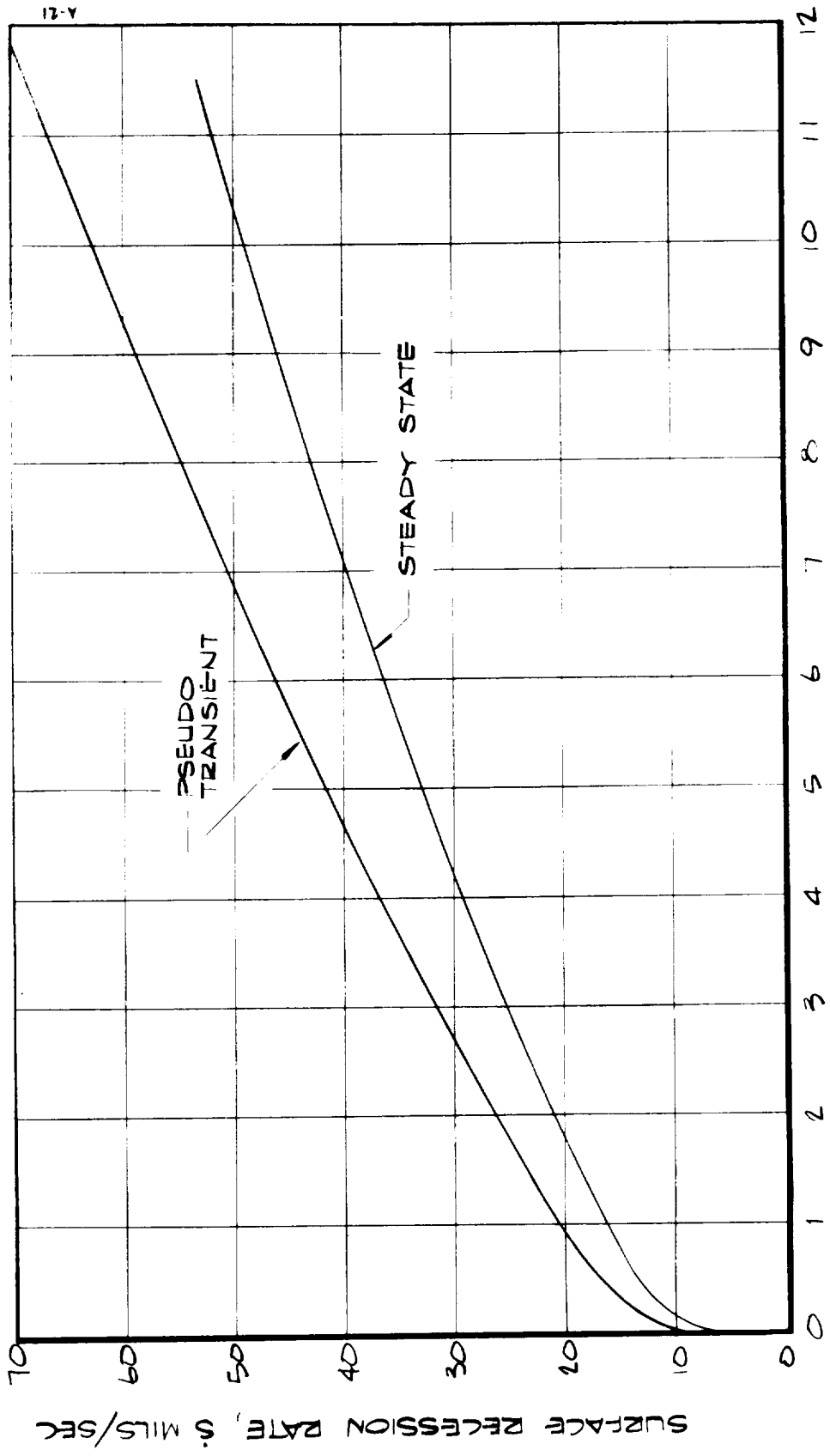

FIGURE 2-16 EFFECT OF PARTICLE DEPOSITION RATE ON THE STEADY STATE SURFACE RECESSION OF CARBON PHENOLIC.

behavior due to the above chemical mechanism can and should be more accurately quantified by detailed transient calculations.

The above post-fire analysis for the 44-SS-4 nozzle was used in support of the final 260-SL-3 material performance predictions as discussed in the following section.

2.4.2 260-SL-3 Nozzle Predictions and Post-Fire Analysis

The predictions of material performance for the 260-SL-3 nozzle were performed in two steps: first, a preliminary prediction prior to the 44-SS-4 nozzle firing; and second, a final prediction prior to the 260-SL-3 nozzle firing and incorporating the post-fire analysis results of the 44-SS-4 firing. These prediction steps are summarized in the table below. Note that at all

260-SL-3 PREDICTIONS

- Preliminary
  - Prior to 44-SS-4 motor firing
    - All locations
      - Transient response calculation, surface recession due to gas phase reactions with surface material
- Final
  - Prior to 260-SL-3 motor firing
    - All locations except C through F at 0°
      - Transient response calculations, surface recession due to gas phase reactions with surface material and corrected for char warp
    - Locations C through F at 0°
      - Extrapolation of 44-SS-4 nozzle results
  - After 260-SL-3 motor firing (before response measurements were available)
    - Locations C through F at 0°
      - Quasi-steady response calculations, surface recession due to gas phase and particle (Al_2O_3) reactions with surface material and corrected for char warp

locations except the four between the propellant lobes for which particle deposition was expected (C through F at 0°), the final predictions differed from the preliminary predictions only by the char warp correction. The char warp was assumed to be proportional to char depth through Equation (2-7) in the final predictions; however, predictions were also made based on char thickness, Equation (2-8). Note that for silica phenolic at all layup angles and carbon phenolic at 90° layup angle (referenced to the surface) no warp was assumed to occur. At the four particle deposition locations, the final predictions were performed in two steps - first, an extrapolation of the

44-SS-4 nozzle results was performed and second, an approximate calculation of the performance was made.

All prediction results and their comparison with measurement are presented in Table 2-6. The final surface recession and char depth predictions and their comparison with measurement are shown in Figures 2-17 and 2-18. Because the nose part dropped into the case after the firing, only average measured results were available in this region (between locations B and E) and therefore no direct comparison between measurement and prediction is possible at these locations. Also, because the exit cone was lost, no comparisons are possible in this region (location J). The comparison between measured and predicted surface recession (Figure 2-17) is seen to be quite favorable at all positions including the silica phenolic part in the underneath section of the nozzle (location A). In the particle deposition region, the predictions exhibit a somewhat higher recession than the measurements. These comparisons and appropriate information relative to the predictions are discussed below.

In the extrapolation of material performance in the particle deposition region, the 44-SS-4 results at the four appropriate locations (C through F at 0°) were used directly to relate computed and actual expected surface recession for the 260-SL-3 nozzle according to

$$s_{260} = \frac{(s_{pred})_{260}}{(s_{pred})_{44}} \left[(s_{meas})_{44} + (s_{warp})_{44} \right] - (s_{warp})_{260} \qquad (2\text{-}11)$$

where the predicted surface recessions (s_{pred}) were from the preliminary calculations which did not include the char warp or particle deposition effects and the warp recessions were calculated from Equation (2-7). These estimates for locations C, D, E, and F between propellant lobes (0°) are included in Table 2-6.

In the final approximate predictions for the 260-SL-3 nozzle, the 44-SS-4 material performance was used to define the particle deposition rates which were in turn applied to the 260-SL-3 predictions. As noted above, the occurrence of particle deposition is related to the non-circular grain port configuration. With increasing firing time, the grain port approaches a circular cross-section and therefore the particle deposition rate will decrease through the firing. Based on the cold flow test results (Section 2-3), it was therefore assumed that particle deposition was significant only for the first third of the 44-SS-4 and 260-SL-3 firings. The deposition rate assumed in the final predictions was therefore as shown in the sketch below.

TABLE 2-6

MATERIAL PERFORMANCE PREDICTIONS FOR THE 260-SL-3 NOZZLE

Location	A/A_*	Material	Surface Recession (in)					Char Depth [b]	
			Measured [a]	Final Prediction		Preliminary Final Pred.	Initial Pred.	Measured [a]	Final Pred.
				Warp Proportional to Char Depth	Warp Proportional to Char Thickness				
A	- underside	FM5131 Silica Phenolic		0.696	0.696		0.696		0.90
B	- underside	MX4926 Carbon Phenolic		0.096	0.096		0.178		1.13
C-0°	-2.00 nose leading edge		(0.77)	1.07		0.906	0.253	(1.49)	--
C-60°				0.288	0.288		0.288		1.39
D-0°	-1.80			0.855	--	0.785	0.418		--
D-60°				0.309	0.337		0.399		1.18
E-0°	-1.26			0.694	--	0.654	0.525		--
E-60°				0.414	0.456		0.509		1.25
F-0°	-1.06		0.53	0.582	--	0.547	0.512	1.10	--
F-60°			0.47	0.414	0.456		0.507		1.18
G	1.0		0.43	0.389	0.427		0.481	1.13	1.16
H	1.15			0.233	0.252		0.313		1.08
I	1.90			0.116	0.123		0.185		0.95
J	2.80	FM5131 Silica Phenolic		0.447	0.447		0.447		0.64

a) Results at other locations are presented in Figures 2-17 and 2-18; numbers in parenthesis indicate no position reference was available.
b) Referenced to original surface.

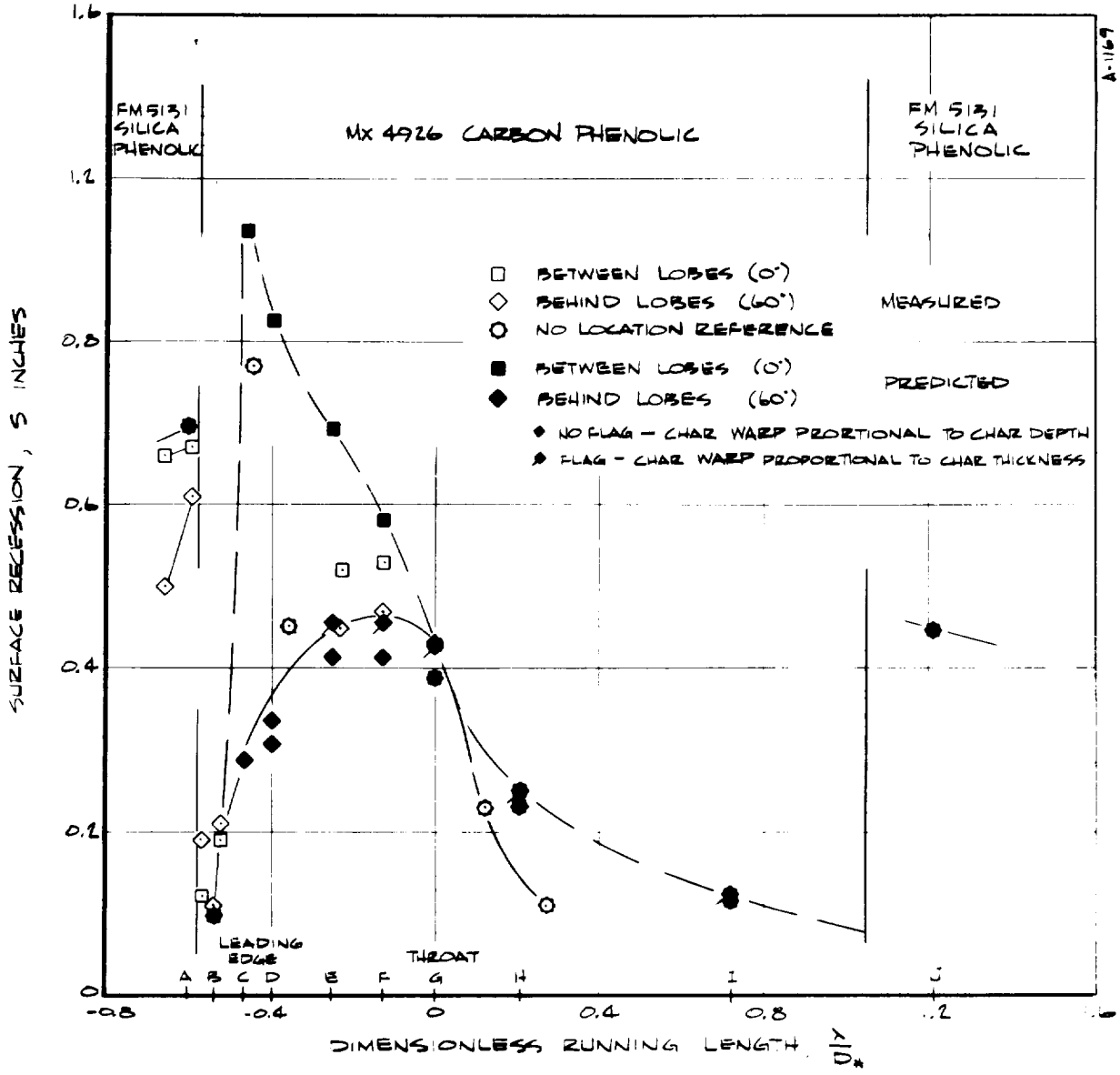

FIGURE 2-17 COMPARISON OF MEASURED AND PREDICTED SURFACE RECESSION FOR THE 260-SL-3 NOZZLE.

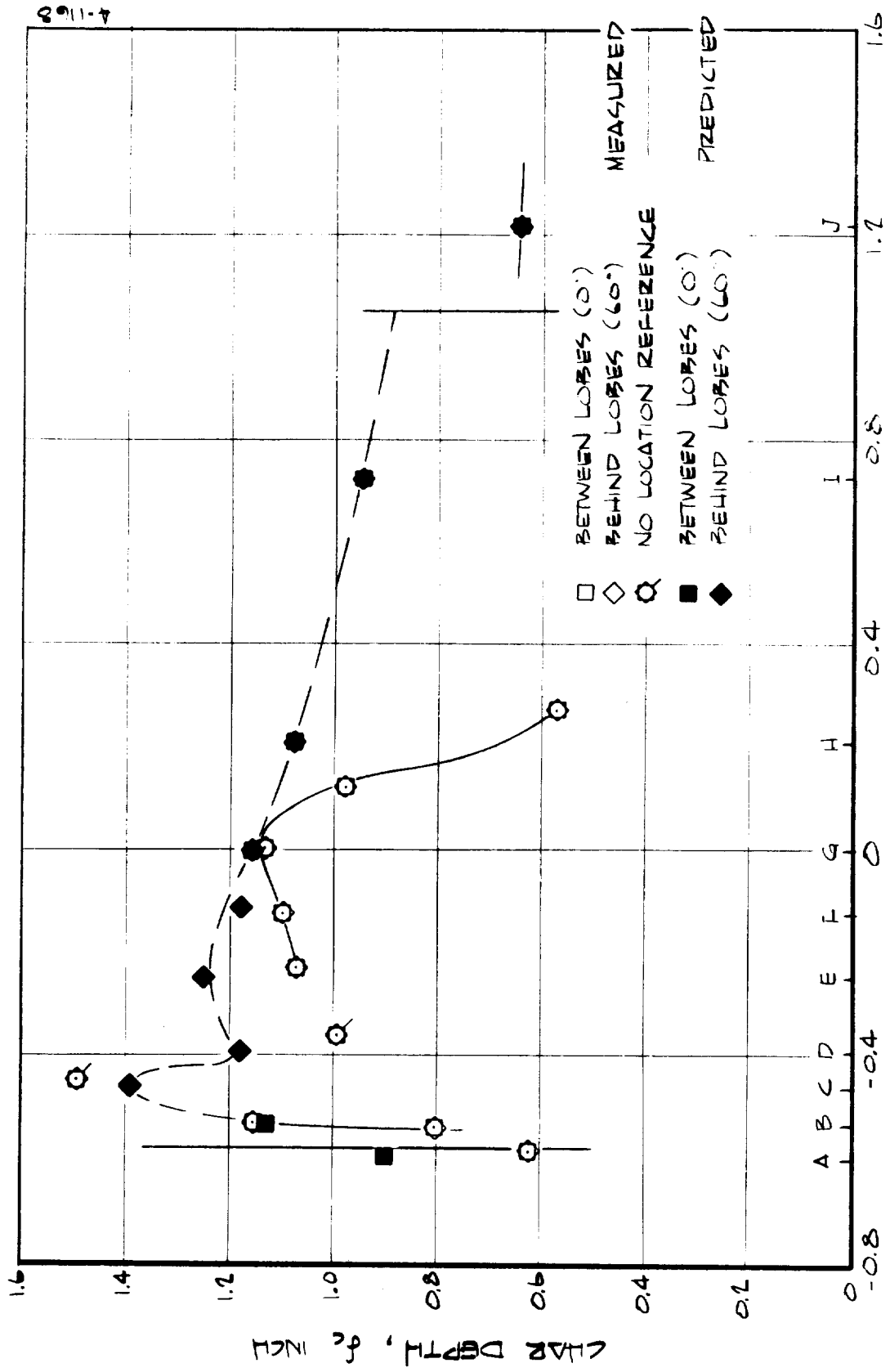

FIGURE 2-18 COMPARISON OF MEASURED AND PREDICTED CHAR DEPTH FOR THE 160-SL-3 NOZZLE

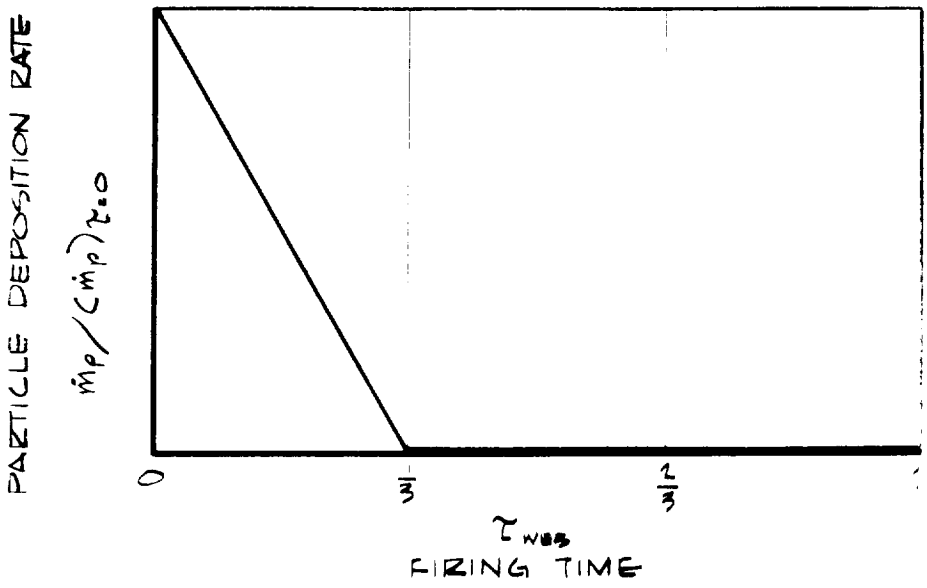

In order to quantitatively define the particle deposition rates at the four between propellant-lobes locations, the measured recession for the 44-SS-4 nozzle was first corrected for char layer warp through Equation (2-7), where the char depth used was that calculated in the preliminary predictions prior to the 44-SS-4 firing.* These corrected measured recessions were then used to define the particle deposition rates by requiring

$$s_{meas} + s_{warp} = \frac{1}{\rho_{char}} \int_0^{t_{web}} (B')(\rho_e u_e C_M)\, dt \qquad (2\text{-}12)$$

where B'(t) was determined through consideration of Figure 2-16 ($B'(\dot{m}_p)$) and the above sketch ($\dot{m}_p(\tau)$). Since particle deposition was limited to the early part of the firing, the pseudo transient curve of Figure 2-16 was used. The maximum particle deposition rates (at $\tau_{web} = 0$) determined for the four locations considered are presented in Table 2-7. For the 260-SL-3 nozzle, the reasonable assumption that the particle deposition rates (fluxes) were the same as those for the 44-SS-4 nozzle was then made. The surface recession was then calculated using these deposition rates and Equation (2-12) where s_{meas} is now interpreted as the predicted surface recession. A more exact treatment of particle deposition, including a complete transient calculation of material surface and in-depth response, could have been performed using both the ACE

*The char depth is a relatively weak function of surface recession and therefore, at least for the 44-SS-4 nozzle, the differences in measured and predicted surface recession would be expected to have only a small effect on char depth.

TABLE 2-7

PARTICLE DEPOSITION RATES FOR THE
44-SS-4 AND 260-SL-3 NOZZLES

Location	A/A_*	Maximum Particle Deposition Rate $(\dot{m}_p)_{\tau=0}$ ($lb/ft^2 sec$)
C-0°	-2.00 nose leading edge	1.18
D-0°	-1.80	1.16
E-0°	-1.26	0.61
F-0°	-1.06	0.26

and CMA computer programs. This effort was beyond the scope of the contract, however.

Before discussing the comparison between measured and predicted material response, it should be noted that propellant ejection and large chamber pressure excursions occurred intermittently near the end of the firing. This anomolous performance should not have had a significant effect on the material response except in localized regions of propellant impact, however. The comparison of measured and predicted performance, wherever comparison can be made, is therefore felt to be valid.

As seen from Table 2-6 and Figure 2-17, the final predictions of material performance in the particle deposition region are somewhat higher than the measurements wherever direct comparisons can be made (locations E and F at 0°). This discrepancy may be attributed to the simplifying assumptions made in the particle deposition analysis or it may be due, at least in part, to a thin alumina layer that was apparently found on the surface of the fired nozzle in the nose region. The actual thickness of this layer or even its existence has apparently not been firmly defined, however. Based on the assumptions and constraints of the analysis performed herein, this layer would not have existed during the firing. Therefore, its presence would result in an apparent overprediction of the surface recession. Also, if the assumptions of the analysis are correct and the alumina layer does in fact exist, it must have formed during or immediately after tail-off. A more detailed analysis of the prediction technique, the fired nozzle, and tail-off phenomena are required to make a more definitive analysis of the results in the particle deposition region.

At the behind-lobes locations in the nose region (locations C through F at 60°) it was felt that no particle deposition would occur. Based on the favorable comparisons between prediction and measurement in this region (Figure 2-17), it appears that this conclusion was correct.

The predicted recessions employing the two char warp assumptions and their comparison with measurement (Figure 2-17) demonstrate that char warp proportional to char thickness, rather than char depth, exhibits a generally better agreement with the measured recessions. This is not too surprising since it is the thickness, not the depth, over which any warp or swelling would be expected to occur. Char depth was used as the primary warp correction parameter in the final predictions because it is less sensitive to differences in measured and predicted surface recession and because the results for the 44-SS-4 nozzle exhibited essentially no difference between the char depth and char thickness corrections. Based on the 260-SL-3 results, however, char thickness is preferable and is therefore recommended for future use (Equation (2-8) for carbon phenolic). It should be noted that the mechanism

of this warp (or swelling) and its occurrence, during the firing or after shutdown, has not been identified and requires further study.

To summarize the 260-SL-3 post-fire analysis presented above, the prediction of surface recession must account for char layer warp or swelling and for particle deposition in certain regions for non-circular grain port configurations. Char warp may be treated as proportional to char thickness except in regions where the layup angle is near 90° referenced to the surface. Particle deposition results in an enhanced surface recession due apparently to the chemical reaction of the particles with the surface (char) material. The calculation of material response in regions where particle deposition occurs requires a knowledge of the particle deposition rate as a function of firing time.

2.5 STRESS ANALYSIS

A stress analysis study was performed for the 260-SL-3 nozzle to determine the structural integrity of the nose region and to define the requirements for an accurate stress calculation. The nose region was considered because successful performance here was critical to the overall nozzle performance and because this performance was considered to be somewhat questionable prior to the firing; it also provided a region which exercised all the capabilities of the stress analysis computer program. The stress analysis was broken down into two different phases: the first was performed prior to the 260-SL-3 firing to analyze the integrity of the nose region and the second was performed after the firing to study the requirements for accurate computer program calculations of the stress condition. In the first phase, an isotropic properties computer program was used and in the second phase a new, more general Aerotherm orthotropic program, developed just prior to the start of this phase, was used. The computer programs are discussed below in Section 2.5.1 and the analysis results are presented in Section 2.5.2.

2.5.1 Stress Analysis Computer Programs

The stress analysis computer programs used in the study were the Rohm and Haas program (Reference 2-16) and the recently developed Aerotherm Generalized Orthotropic Axisymmetric Solids (GORAS) program. Both programs utilize finite element structural analysis techniques which are based on the direct stiffness matrix displacement method for treating general solid bodies of revolution as discussed in References 2-16 and 2-17. The Rohm and Haas code is limited to isotropic materials; for orthotropic materials, an isotropic approximation of the material properties was therefore made. This code was used for the pre-fire, first phase analysis and the material property data used were simply the maximum values independent of direction (along the

tape or across the tape). Material properties were specified for each finite element and, to provide some compensation for the above properties assumption, maximum values of element temperatures were used to define these properties.

The Aerotherm orthotropic stress analysis program, GORAS, is based on an earlier, less general program developed by Wilson (Reference 2-17) in which the meridional or r-z plane must be a plane of isotropy. The Aerotherm program, however, allows a more general treatment of orthotropy; it can treat orthotropic materials which, at any point, have the plane of isotropy normal to the meridional plane, but otherwise arbitrarily oriented, as well as materials which have the r-z plane as a plane of isotropy. The sketch below provides a convenient representation of this generality. The previous treatment of anisotropy allows properties in the circumferential (θ) direction to differ

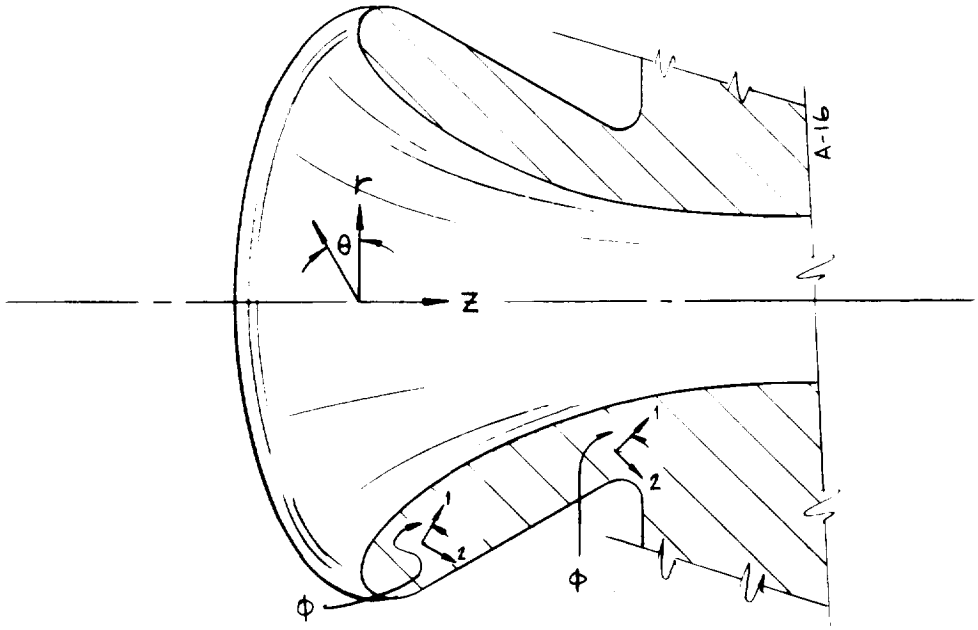

from those in the r-z plane.* The GORAS program allows properties in the radial (r) direction to differ from those in the axial (z) direction where the "principle" axes of this variation are the 1-2 axes which are specified by the variable angle ϕ.** This latter case is, of course, the tape wrap situation

*The r-z plane is a plane of isotropy.

**The 1-θ surface is a surface of isotropy.

where ϕ is the complement of the tape wrap angle ($\alpha = 90^{\circ} - \phi$) and is specified for each mesh point in the problem grid. The meridional (r-z plane) geometry can be completely arbitrary but the external loading must be axisymmetric. The program is based on elastic theory and incorporates a general temperature dependence of material properties.

Material properties are input for each finite element as a function of temperature. Values corresponding to the average temperature of an element are used in the GORAS program stress computation. Therefore, material property data were input in such a manner that effective (or temperature averaged) values for each element were used in the calculation. This is practically feasible because the finite element net was chosen to coincide with the isotherm pattern, and is important and necessary where unavoidably large temperature gradients occur across an element. Actual orthotropic material property data were utilized and are presented in Table 2-8 for MX4926 carbon phenolic and FM5131 silica phenolic. These properties were obtained from References 2-18 and 2-19 through a rational interpretation of the data presented therein. Note that the data in the char region (Reference 2-19) were available only for a carbon phenolic material and were taken to be representative for both materials considered. The virgin material data (Reference 2-18) were available for the specific materials of interest.

Several auxiliary subroutines and satellite programs have also been developed for optional use with the GORAS program. These include a capability for automatic finite element mesh generation and for automatic calculation of temperatures at finite element mesh points from an arbitrarily specified input temperature field. In addition, capability is being developed for automatic plotting of stress level contours. This merely requires modification of an existing program for plotting temperature contours.

2.5.2 Stress Analysis Results

The stress analysis studies were performed for the nose region of the 260-SL-3 nozzle at the behind-propellant-lobes position and for 60 seconds through the firing. The nose region and its isotherms and the three analysis grid mesh systems considered are presented in Figures 2-19 through 2-22. The isothermal lines and surface recession shown in Figure 2-19 were defined by the ablation and thermal response predictions discussed in Section 2.4. This surface recession, indicated by the shaded areas, and the isotherms are the predicted conditions at 60 seconds through the firing at the behind-lobes position. For simplicity in these analyses, the steel support structure was assumed to be rigid; relative to the structural capabilities of the tape wrapped parts this is not an unreasonable assumption. The two phases of the analysis studies

TABLE 2-8

THERMAL EXPANSION AND MECHANICAL PROPERTIES
OF CARBON PHENOLIC AND SILICA PHENOLIC

CARBON PHENOLIC (MX 4926) Poisson's Ratio = 0.2

Thermal Expansion (Referenced to 530°R)				Elastic Modulus In Compression				Elastic Modulus In Shear (Interlaminar)	
Along Tape Direction		Across Tape Direction		Along Tape Direction		Across Tape Direction			
Temperature (°R)	(μin/in°R)	Temperature (°R)	(μin/in°R)	Temperature (°R)	(psi)	Temperature (°R)	(psi)	Temperature (°R)	(psi)
530	3.90	530	8.35	530	2.3×10^6	530	2.3×10^6	530	0.90×10^6
1060	3.90	860	8.35	3260	0.4×10^6	1460	0.3×10^6	640	0.50×10^6
1260	0	1080	25.9	6000	0.15×10^6	6000	0.15×10^6	1260	0.28×10^6
2760	0	1360	0					1360	0.04×10^6
3460	1.40	2760	0					1960	0.04×10^6
4460	2.60	3460	1.4					2060	0.15×10^6
5460	3.55	4460	2.6					6000	0.15×10^6
		5460	3.55						

SILICA PHENOLIC (FM 5131) Poisson's Ratio = 0.2

Thermal Expansion (Referenced to 530°R)				Elastic Modulus In Compression				Elastic Modulus In Shear (Interlaminar)	
Along Tape Direction		Across Tape Direction		Along Tape Direction		Across Tape Direction			
Temperature (°R)	(μin/in°R)	Temperature (°R)	(μin/in°R)	Temperature (°R)	(psi)	Temperature (°R)	(psi)	Temperature (°R)	(psi)
530	3.45	530	16.6	530	2.0×10^6	530	1.15×10^6	530	0.25×10^6
820	3.45	1020	16.6	1460	0.6×10^6	1300	0.15×10^6	660	0.15×10^6
1200	0.30	1460	0	6000	0.15×10^6	6000	0.15×10^6	1060	0.11×10^6
1460	0	2760	0					1160	0.04×10^6
2760	0	3460	1.40					2460	0.04×10^6
3460	1.40	4460	2.60					2560	0.15×10^6
4460	2.60	5460	3.55					6000	0.15×10^6
5460	3.55								

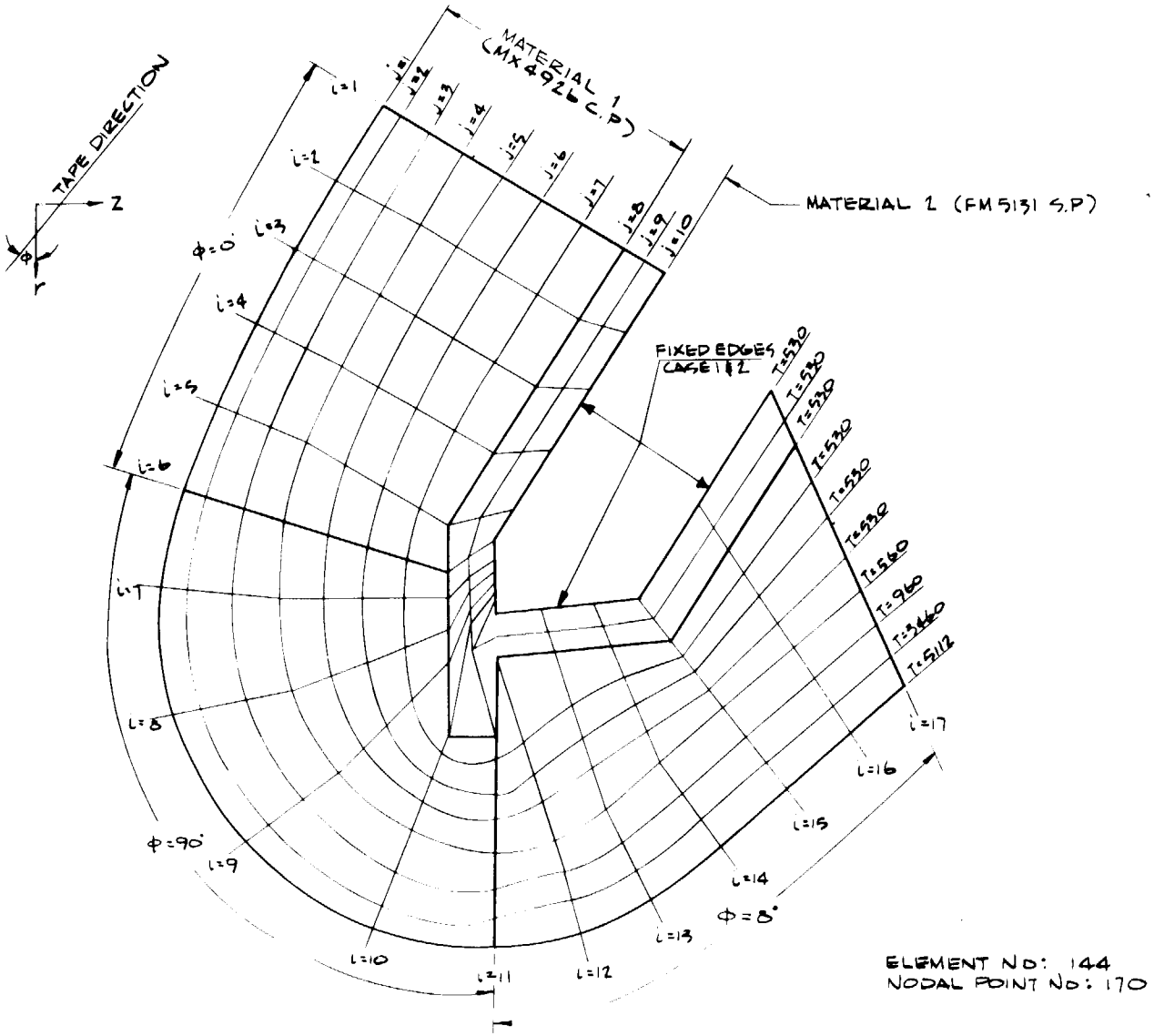

FIGURE 1-10 NOZZLE PROBLEM STANDARD MESH

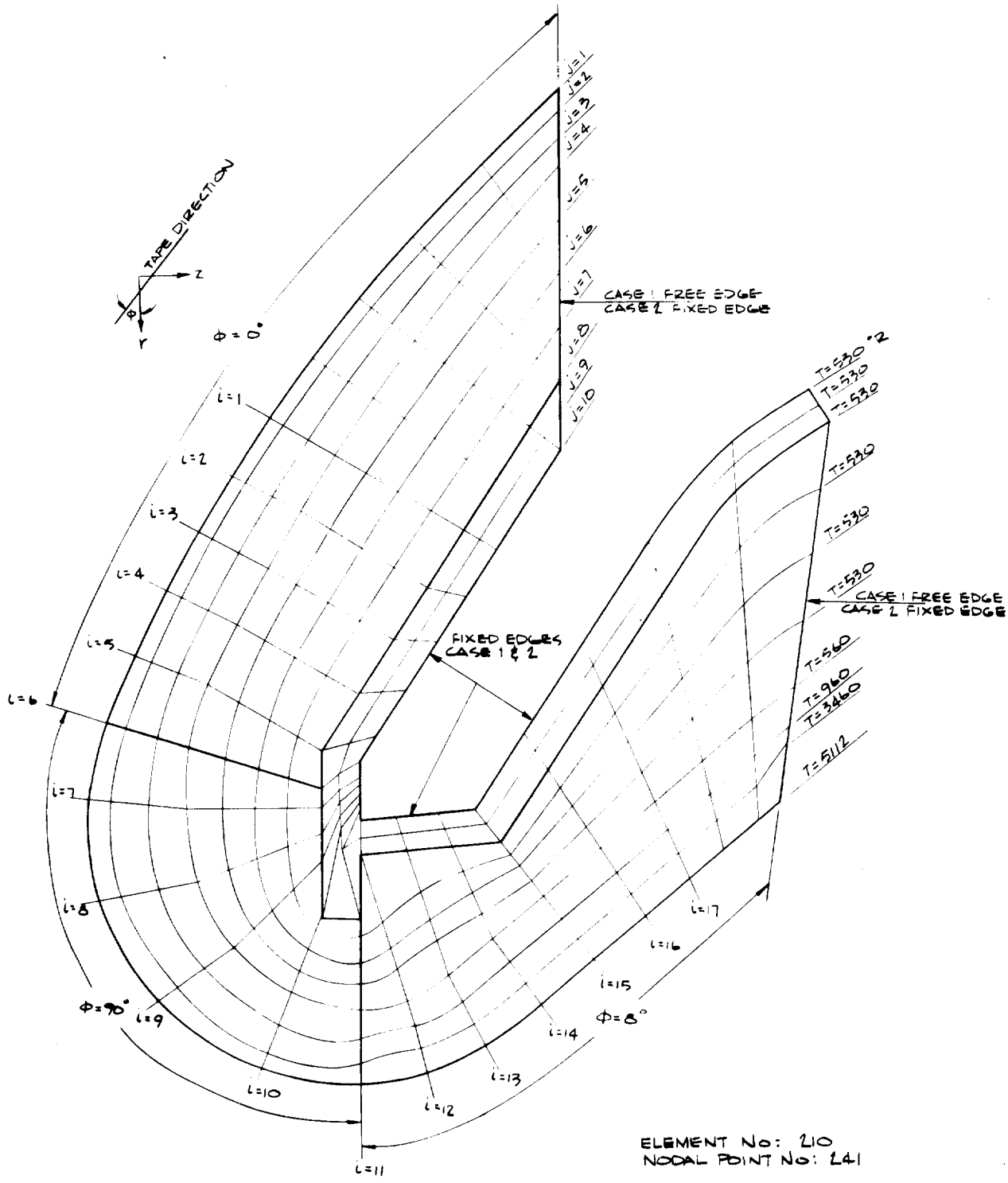

FIGURE 2-21 NOZZLE PROBLEM MOVED BOUNDARIES.

A-408

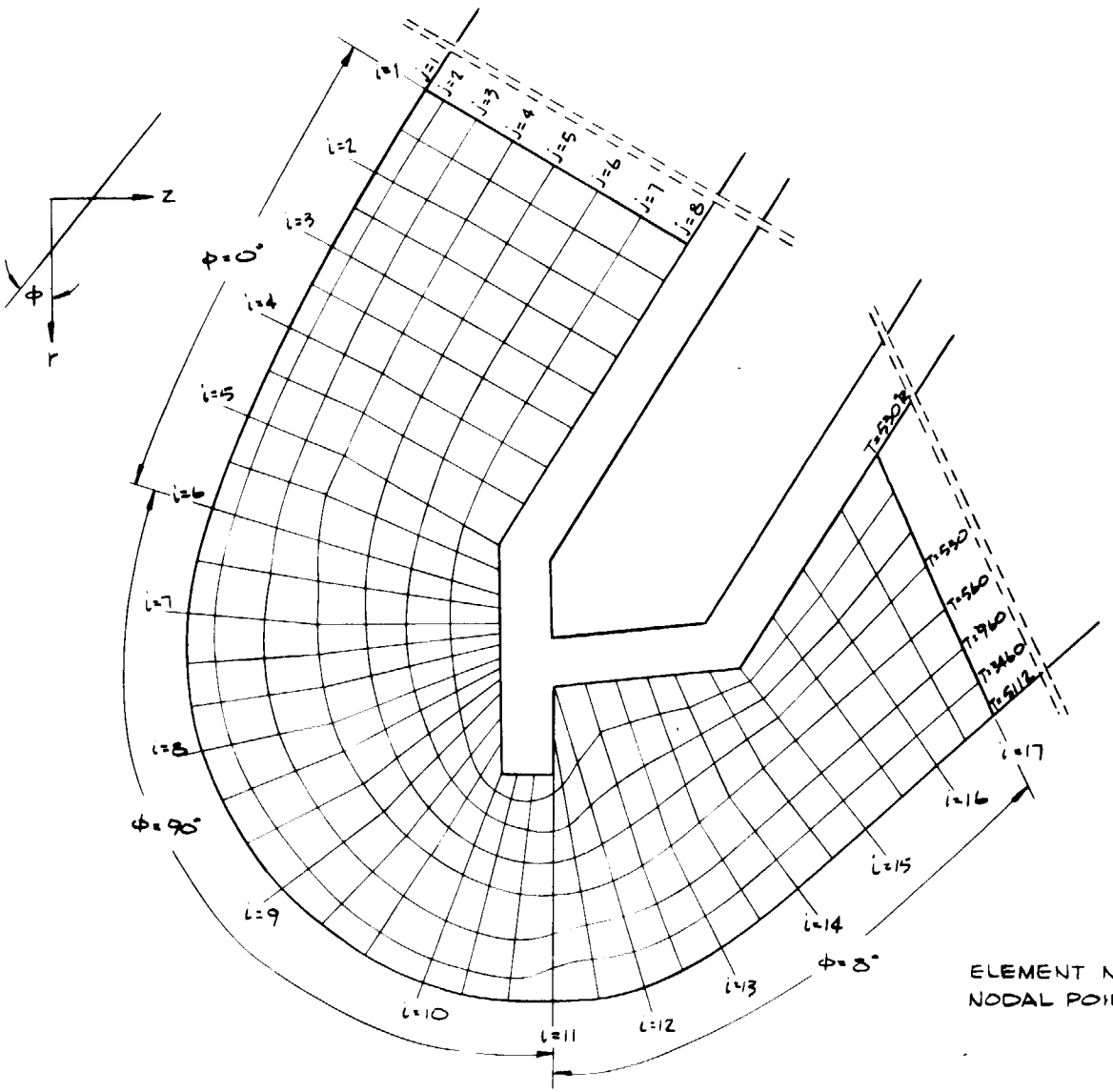

ELEMENT No: 252
NODAL POINT No: 296

FIGURE 2-22 NOZZLE PROBLEM FINER MESH

A-410

are presented in the following sections, Section 2.5.2.1 discussing the pre-fire structural integrity analysis and Section 2.5.2.2, the accuracy requirements analysis.

2.5.2.1 Pre-fire Analysis

For the pre-fire analysis, the computer program of Reference 2-16 was used and isotropic properties necessarily assumed. As noted in Section 2.5.1, maximum properties were used in the calculations. These properties corresponded closely to the along tape direction properties of Table 2-8 except that the high-temperature thermal expansion was somewhat lower than that indicated. The complete structural response was calculated for the grid mesh of Figure 2-20. The analysis of these calculations was based on the calculated stress levels with particular note taken of bond-line and cross-ply tensile stresses and bond-line and interlaminar shear stresses. The ultimate cross-ply tensile stress for both MX4926 carbon phenolic and FM5131 silica phenolic is about 500 psi and the ultimate interlaminar shear stress is about 1000 psi. These values were also taken to be representative of the bond-line values. The compressive load capabilities are about 20,000 psi and 8000 psi for MX4926 carbon phenolic and FM5131 silica phenolic, respectively, and the tensile load capabilities in the tape direction are about 5000 psi for both materials.* These last values were well above the corresponding calculated levels.

Based on the calculated stress levels and using the above ultimate stress values as a guide, the following general conclusions were made. The primary bond-line, D in Figure 2-19, was in compression and the shear levels were less than 1000 psi over most of its length. A tensile stress was calculated to occur in the region at the end of the steel support structure, however, and the shear levels were found to be high in this region and in the region of bond-line C. Based on the compressive loading and moderate shear over most its length, however, bond-line D was expected to hold through the firing.

Bond-lines A, B, and C were formed during the part and over-warp cure process and therefore had greater inherent strength than bond-line D. The preliminary analysis indicated that bond-line A was in compression and that the shear levels were moderate, the bond-line corresponding closely to the to the principle axis (zero shear) in the virgin material region. On this basis, no problem with the integrity of bond-line A was expected. Bond-line B, however, exhibited high shear levels and tensile loading primarily over the vertical portion of its length. These levels were acceptable, however, on the "downstream" portion of the bond-line and, therefore, the bond

*These ultimate stress figures are for the virgin materials from Reference 2-18.

should hold at least in this region. Bond-line C exhibited high tensile and shear stresses and, therefore, was not expected to contribute to the structural integrity of the assembly.

In summary, bond-lines A and D were expected to hold the nose ring in place, bond-line B was expected to hold the downstream part in place, and bond-line D was expected to hold the whole assembly in place. It was therefore concluded that no structural failure would occur during the firing. It was also concluded, however, that thermal degradation of the bond-lines during the cooldown period after firing could well result in the nose ring or nose assembly dropping out. The nose ring could fall out due to the failure of bond-line A and the local failure of bond-line D or the whole assembly could fall out due to the complete failure of bond-line D. These conclusions (reported initially in Reference 2-20) were borne out in the 260-SL-3 firing.

Based on the pre-fire analysis, the cross-ply tensile stress and interlaminar shear were such that no delaminations would be expected to occur in both the nose ring and the downstream port.

2.5.2.2 Accuracy Requirements

The study of the requirements for accurate computer program stress calculations fell conveniently into three categories:

Effect of an isotropic assumption for an orthotropic material

Effect of boundary location and constraint

Effect of grid mesh size.

Representative results are presented in Figures 2-23 through 2-27, Figures 2-28 through 2-32, and Figures 2-33 through 2-37, respectively; stress conditions are presented for the nose ring and adjacent parts in terms of the normal stresses in the across-the-tape direction for several in-depth locations and the shear stress along bond-lines A and D. The mesh systems used and identified in the figures were presented previously in Figures 2-20 through 2-22. All results presented were generated by the GORAS program with material property input as presented in Table 2-8. The results of Figures 2-23 through 2-27 for the maximum properties isotropic case are quite similar to those obtained in the pre-fire analysis using the code of Reference 2-16.*

In Figures 2-23 through 2-27, the stress condition calculated for an isotropic approximation of the orthotropic properties of MX4926 carbon phenolic is compared with the stress condition calculated for the actual orthotropic

*The differences between the two results were small and were due to the different char thermal expansion properties used as discussed previously.

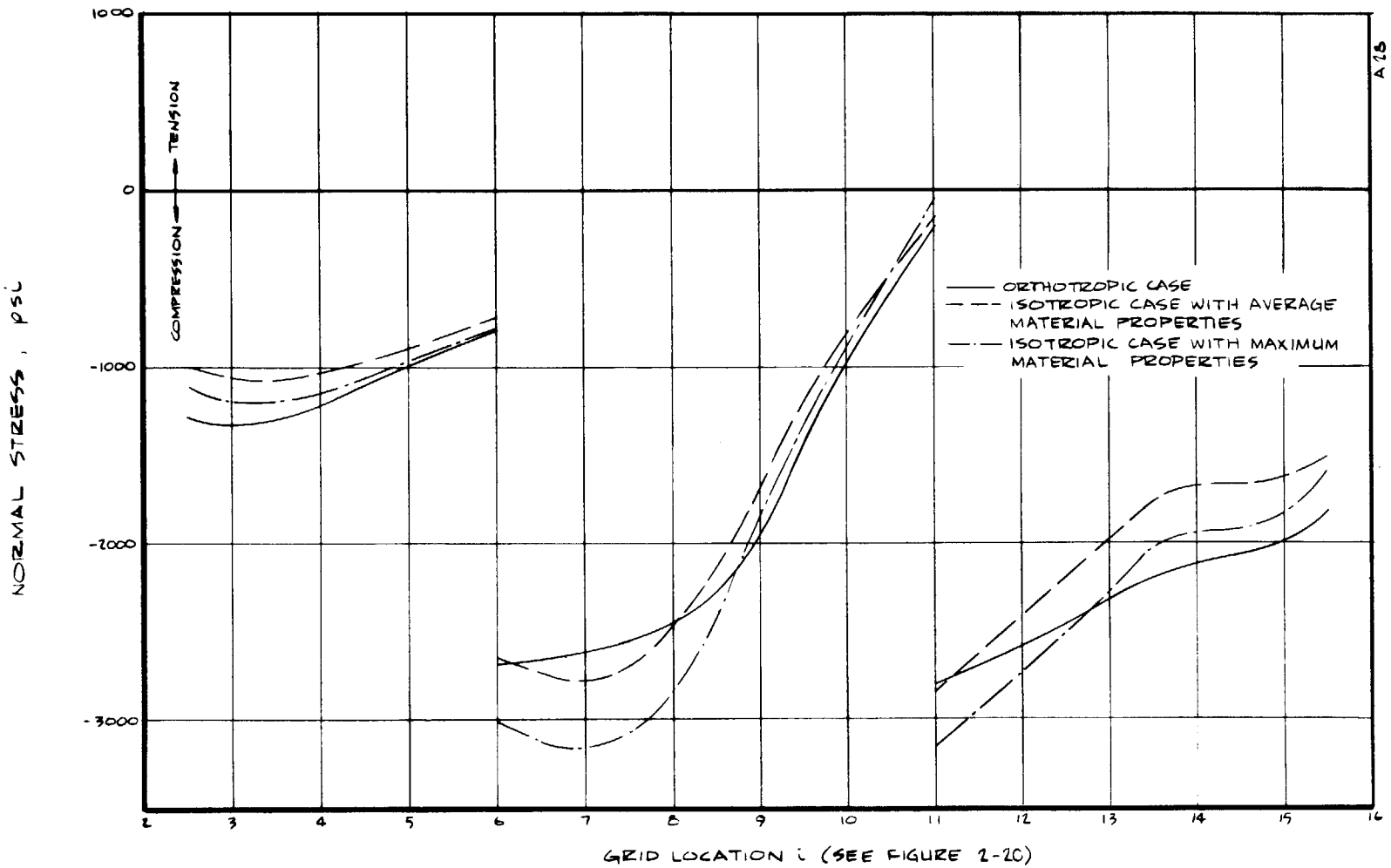

FIGURE 2-23 STRESSES ACROSS THE TAPE DIRECTION FOR ROW OF ELEMENTS BOUNDED BY THE ISOTHERMS T = 512 °R & T = 3460 °R (J = 2)

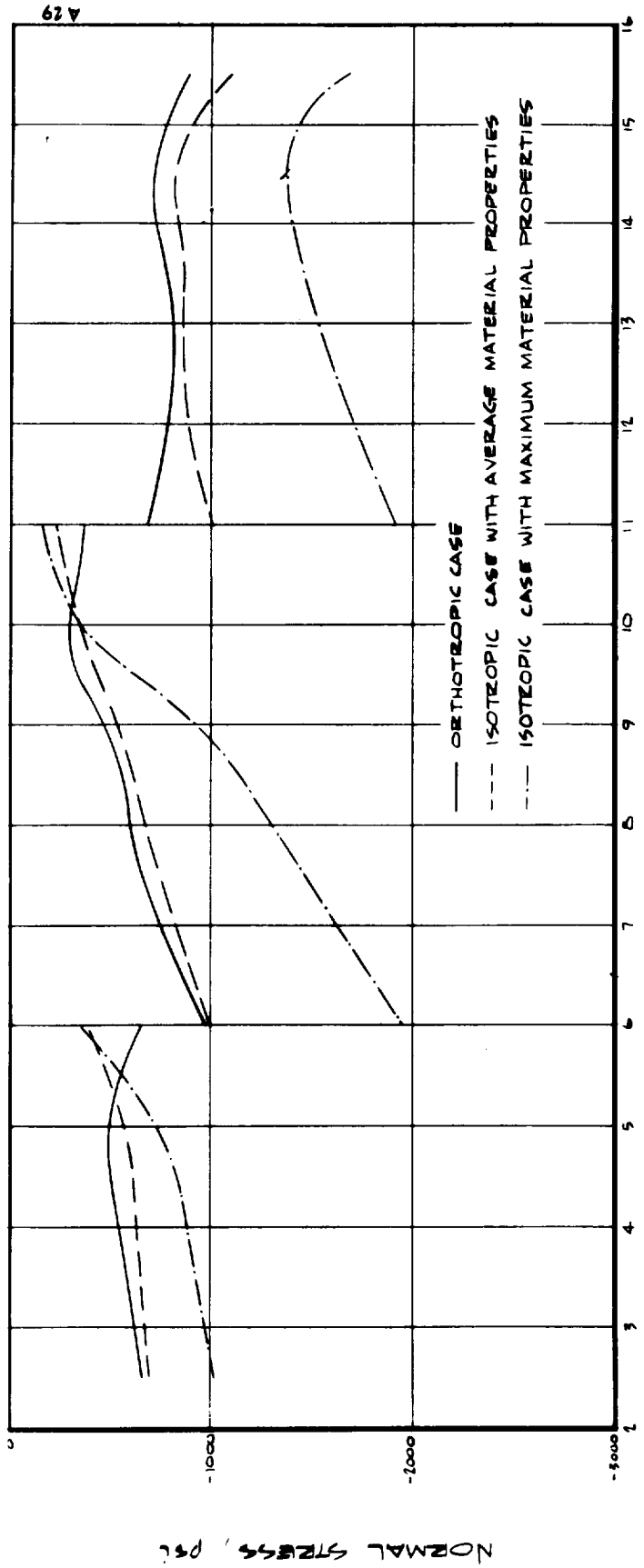

FIGURE 2-24 NORMAL STRESSES ACROSS THE TAPE DIRECTION FOR ROW OF ELEMENTS BOUNDED BY THE ISOTHERMS T = 3460°R & T = 960°R (J = 2-3)

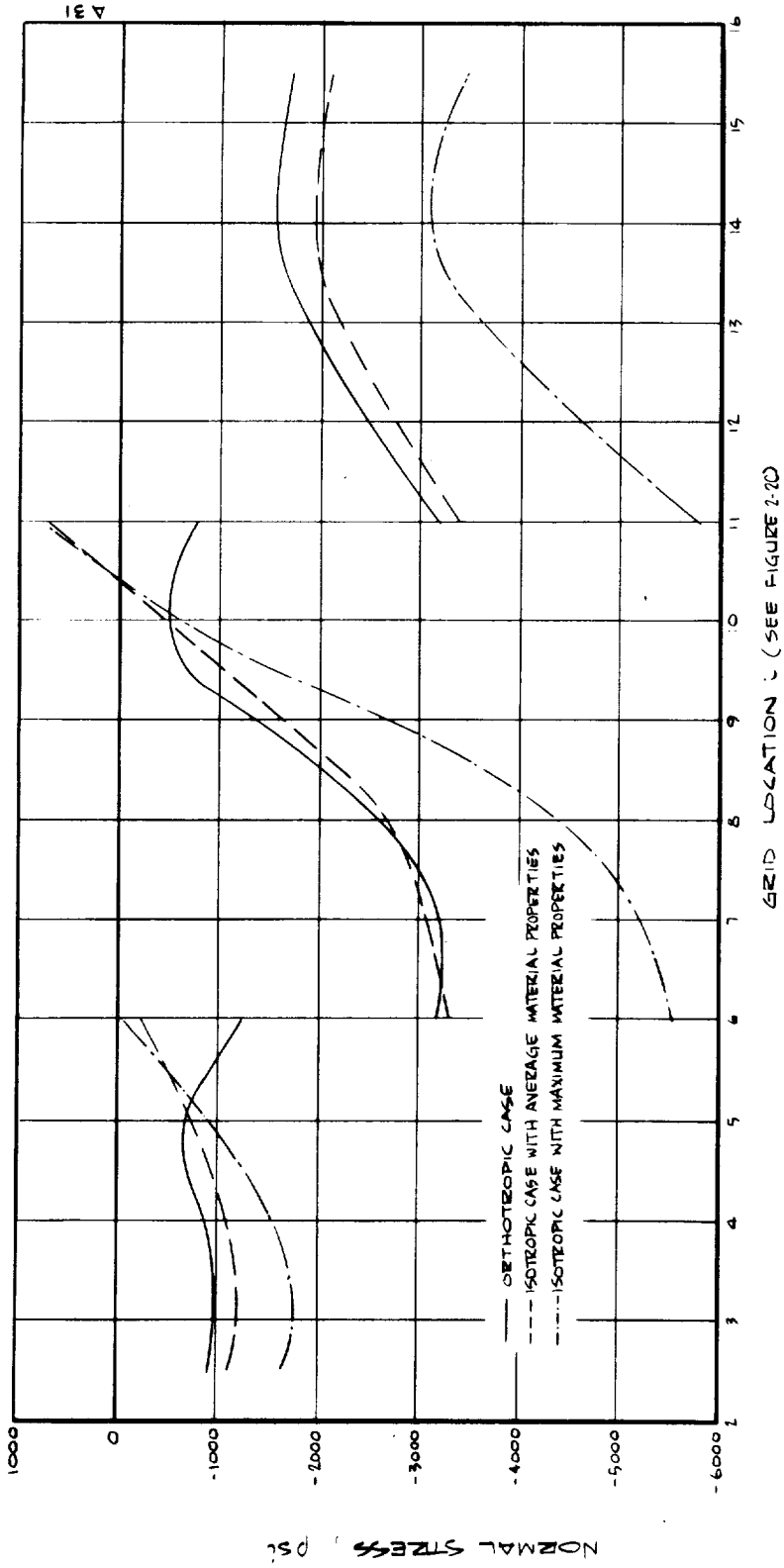

FIGURE 2-15 NORMAL STRESSES ACROSS THE TAPE DIRECTION FOR ROW OF ELEMENTS BOUNDED BY THE ISOTHERMS T= 960°R & T= 560°R (J = 3-4)

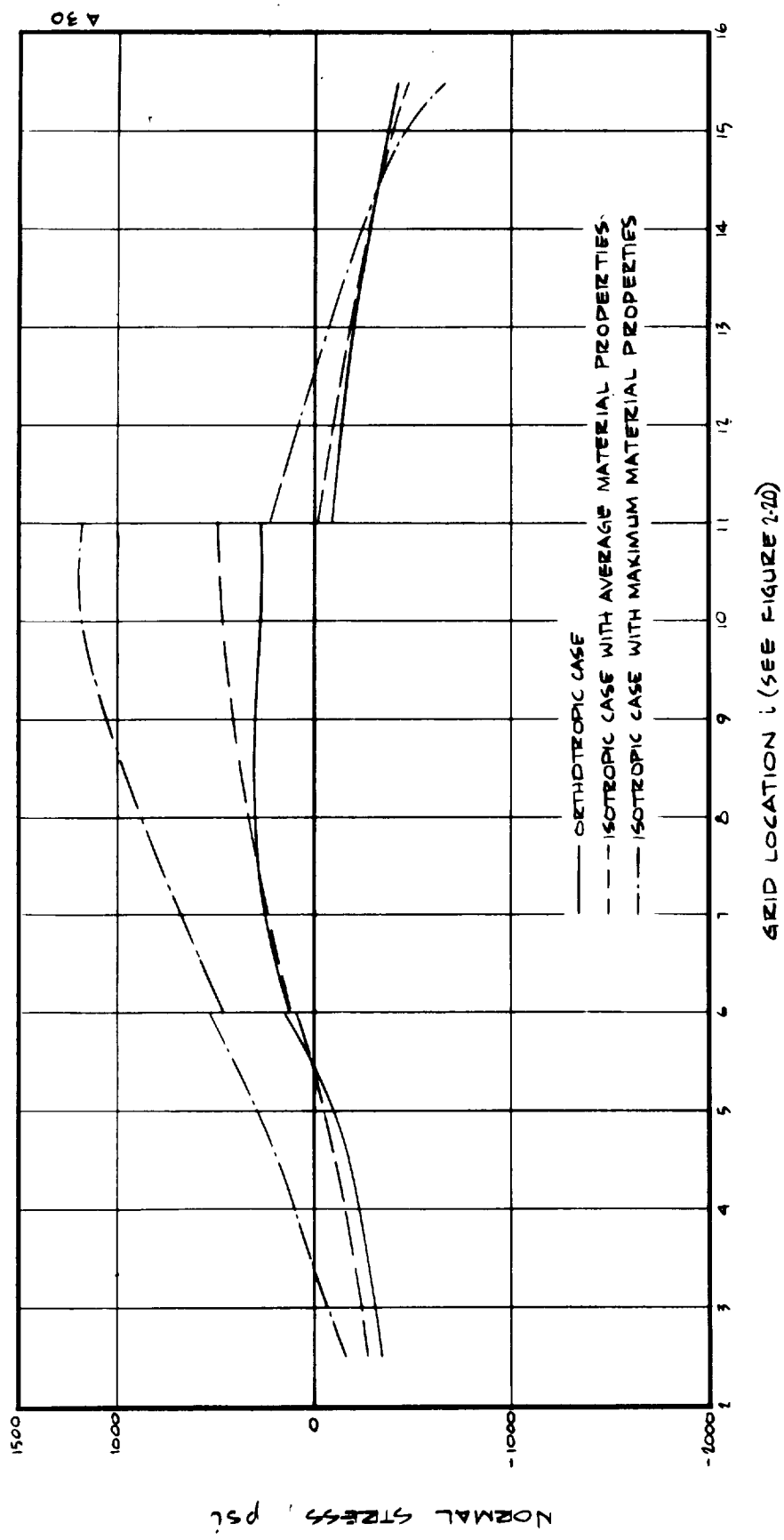

FIGURE 2-26 NORMAL STRESSES ACROSS THE TAPE DIRECTION FOR ROW OF ELEMENTS BOUNDED BY $j = 5$ & $j = 6$ ($T = 530\ ^{\circ}R$)

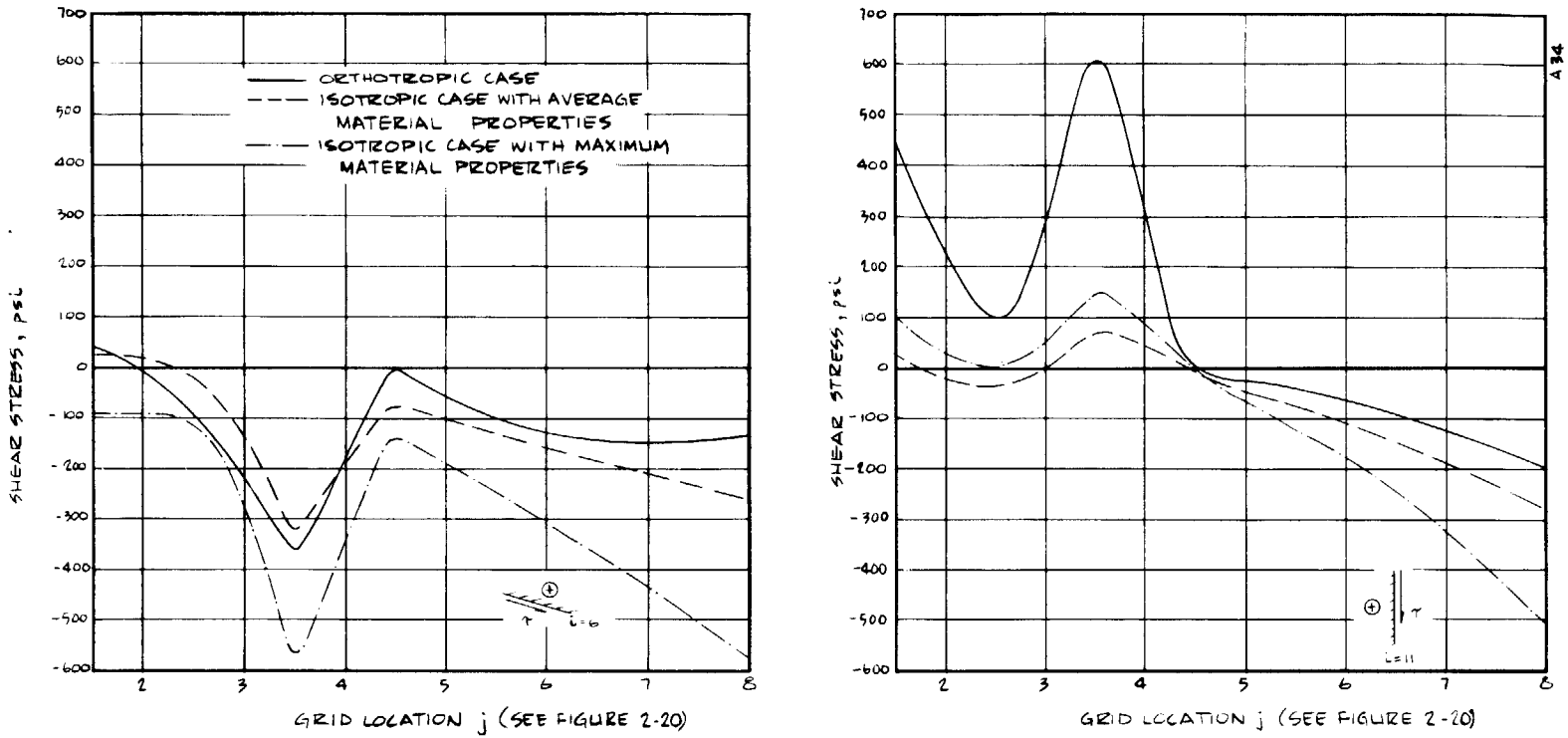

a) i = 6 (ϕ = 0-90)

b) i = 11 (ϕ = 90-8)

FIGURE 2-27 SHEAR STRESS ALONG THE BOND LINES

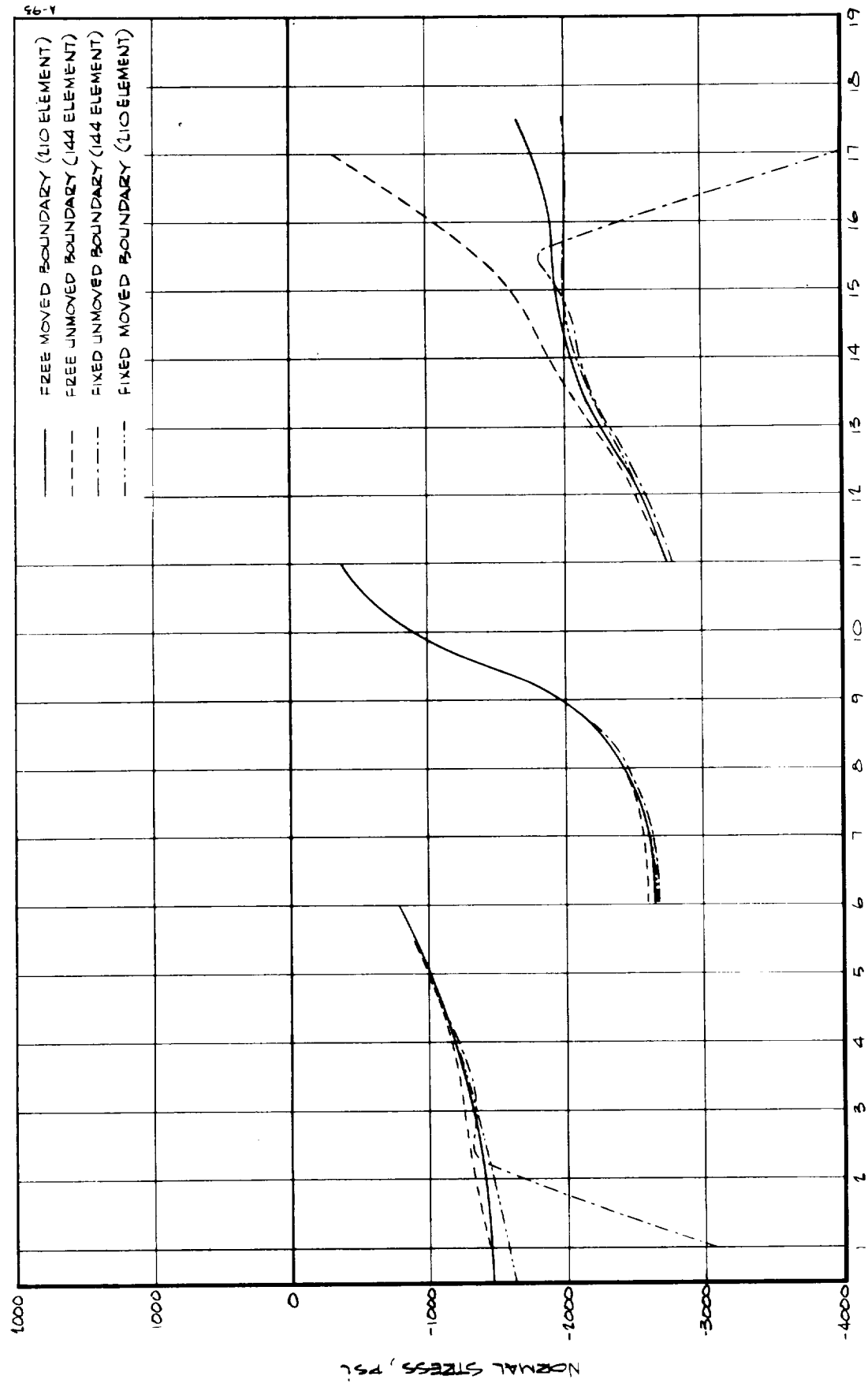

FIGURE 2-18 STRESSES ACROSS THE TAPE DIRECTION FOR ROW OF ELEMENTS BOUNDED BY ISOTHERMS T = 511.2 & T = 346.0 °R (1 : 1 - 2)

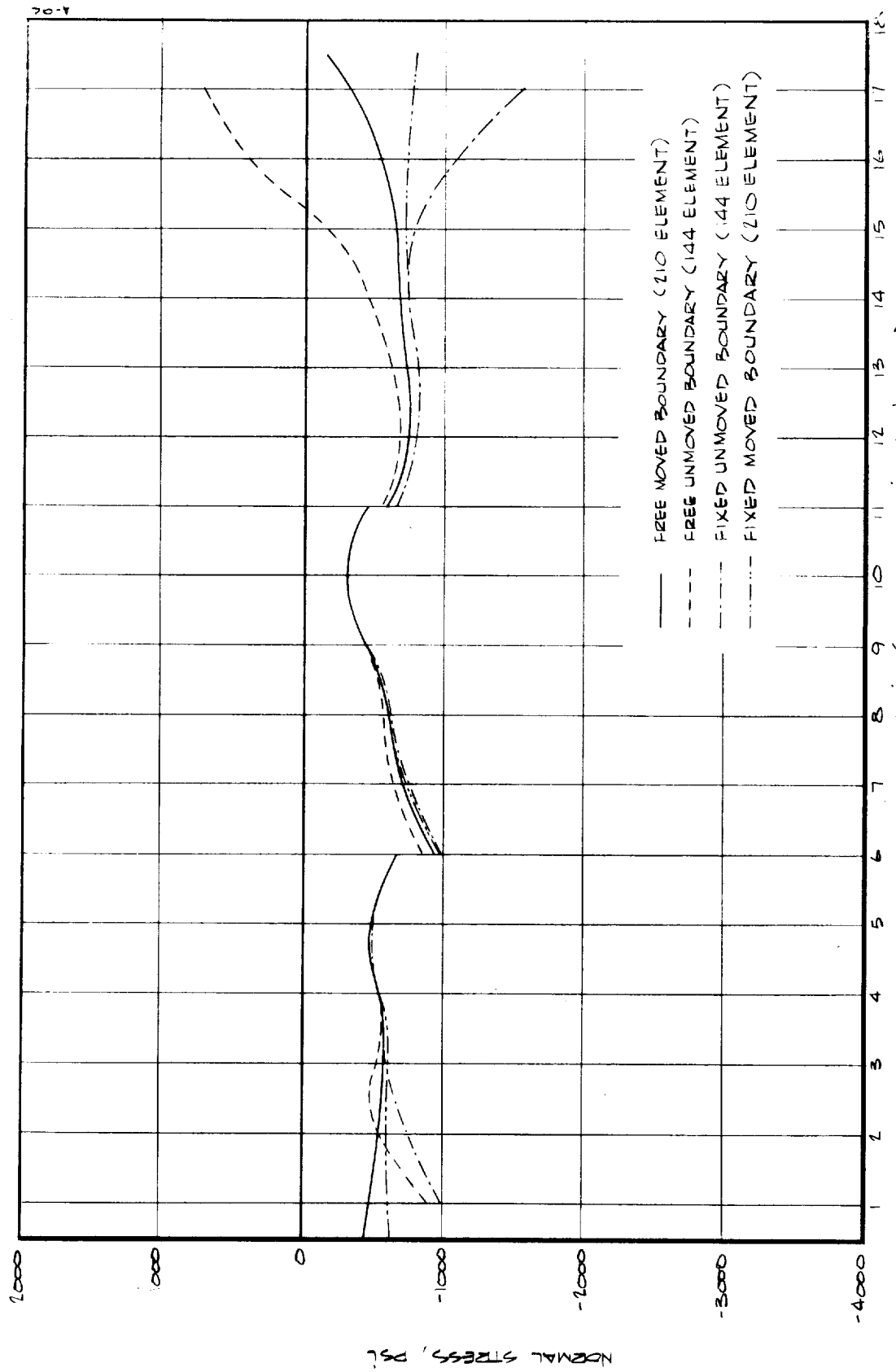

FIGURE 2-29 STRESSES ACROSS THE TAPE DIRECTION FOR ROW OF ELEMENTS BOUNDED BY ISOTHERMS T = 3460 & T = 960 °R (J = 2-3)

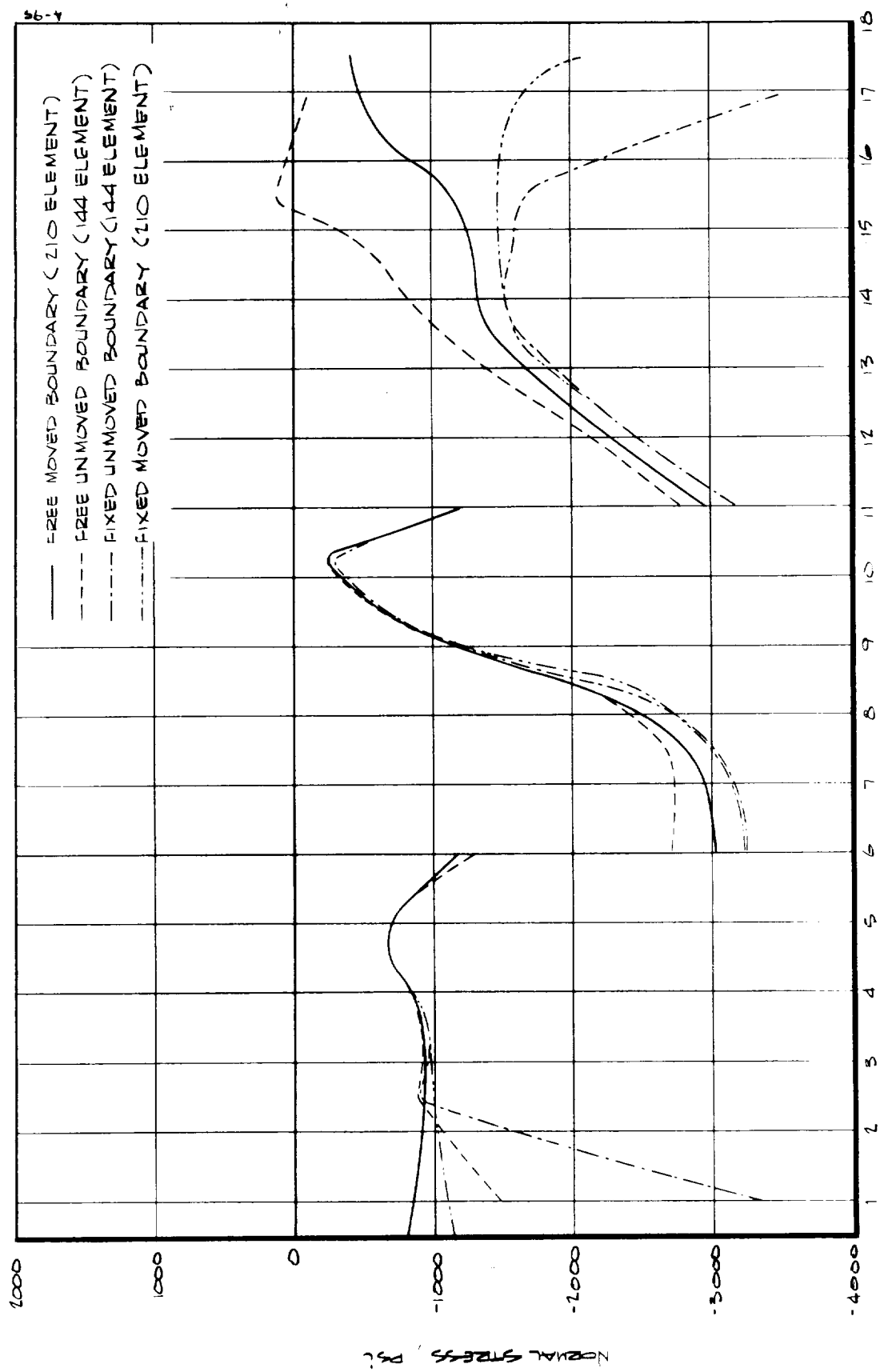

FIGURE 2-30 STRESSES ACROSS THE TAPE DIRECTION FOR ROW OF ELEMENTS BOUNDED BY ISOTHERMS T=960 & T=580 °F (J=3-4)

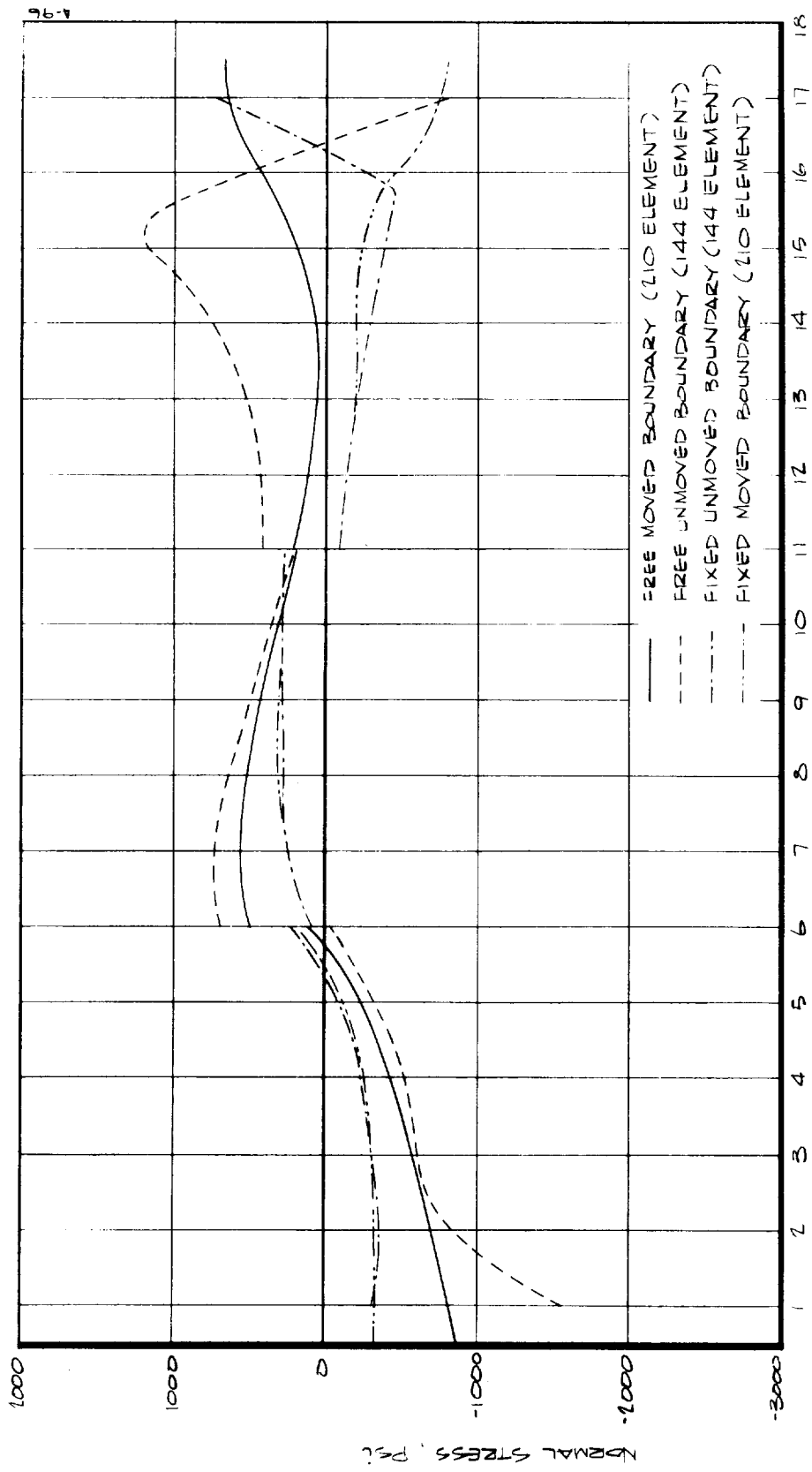

FIGURE 2-31 STRESS ACROSS THE TAPE DIRECTION FOR ROW OF ELEMENTS BOUNDED BY J=5 & J=6 (T=530°R)

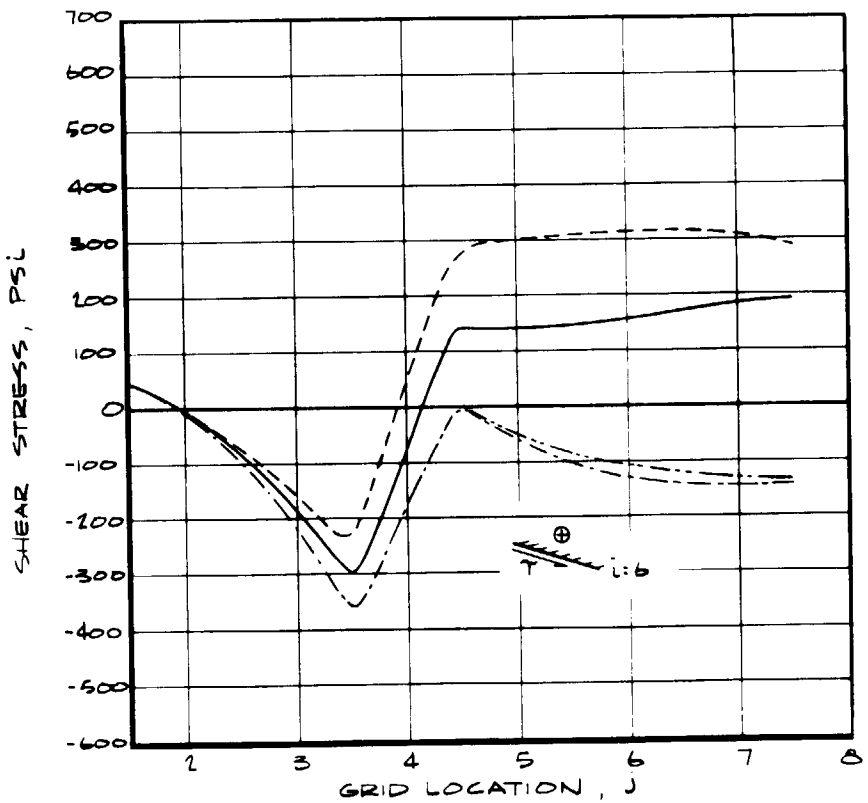

(a) $i = 6$ ($\phi = 0 - 90$)
(SEE FIGURES 2-20 & 2-21)

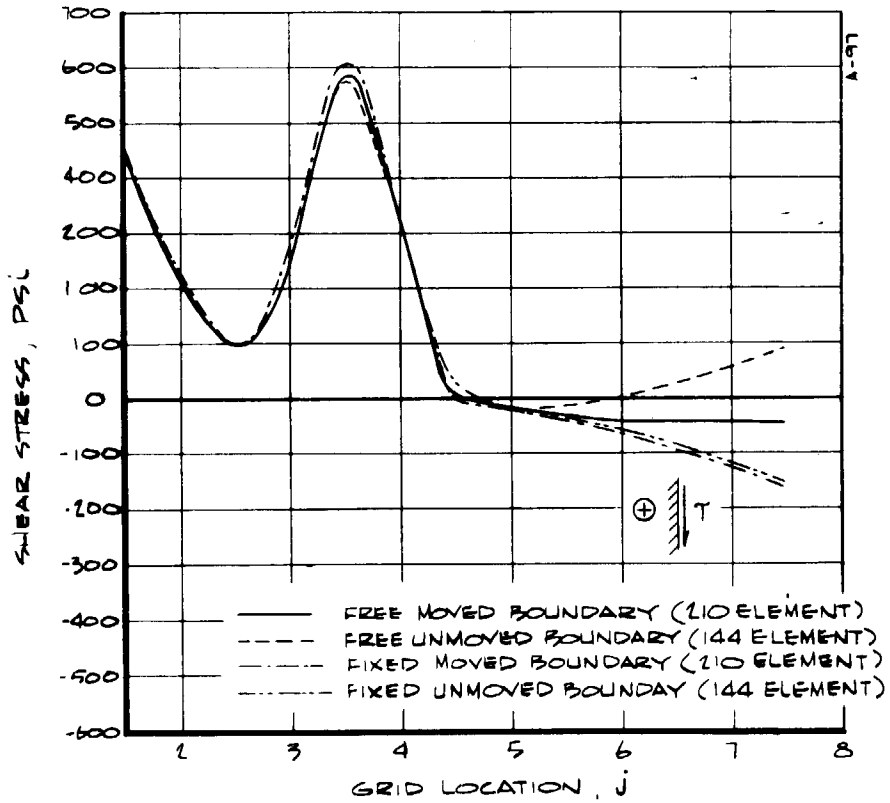

(b) $i = 11$ ($\phi = 90 - 8$)
(SEE FIGURES 2-20 & 2-21)

FIGURE 2-32 SHEAR STRESS ALONG THE BOND LINES.

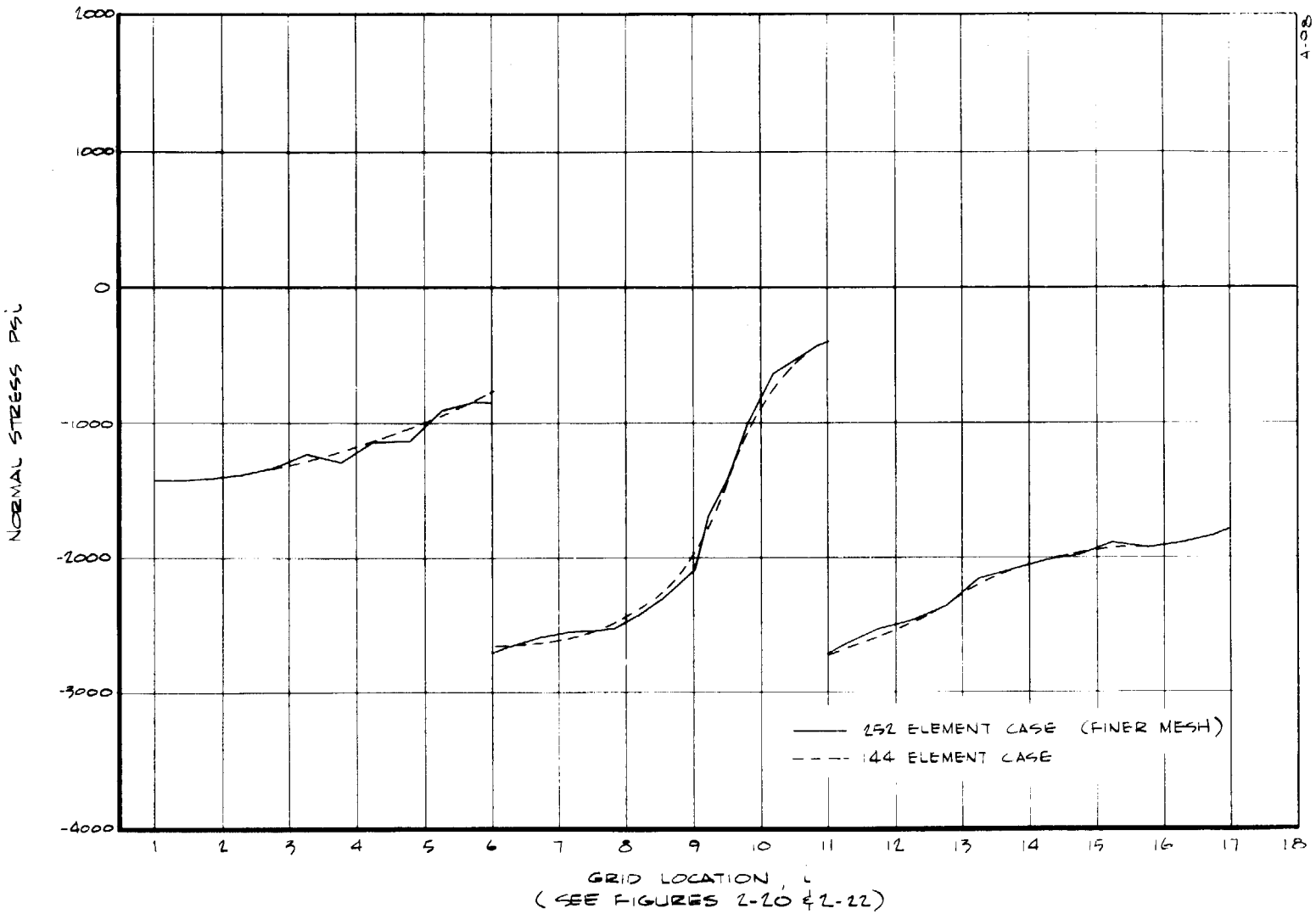

FIGURE 2-33 STRESSES ACROSS THE TAPE DIRECTION FOR ROW OF ELEMENTS BOUNDED BY ISOTHERMS T = 5112 & T = 3460 °R (J = 1-2)

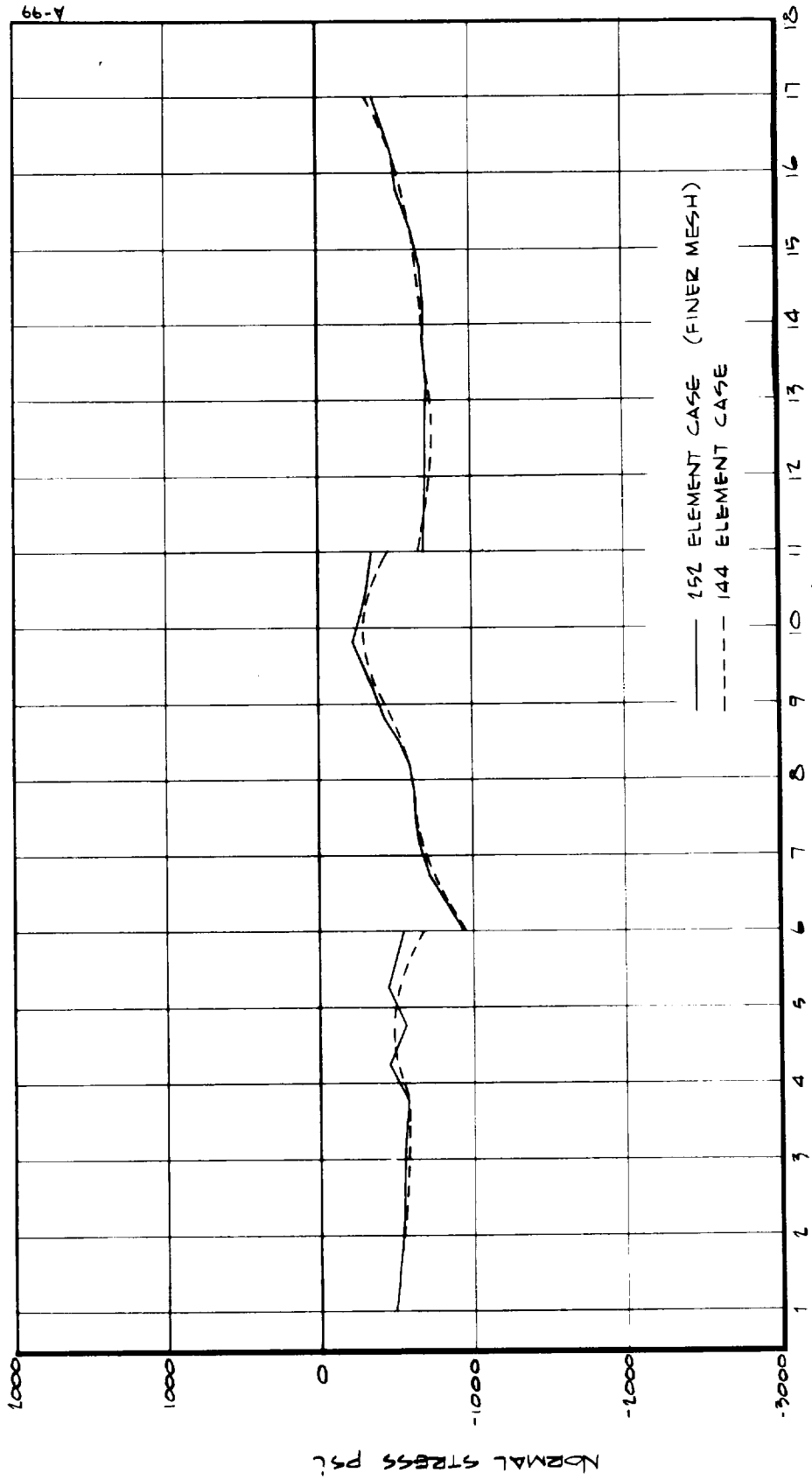

FIGURE 2-34 STRESSES ACROSS THE TAPE DIRECTION FOR ROW OF ELEMENTS BOUNDED BY ISOTHERMS T=3460 & T=960 °R (J = 2-3)

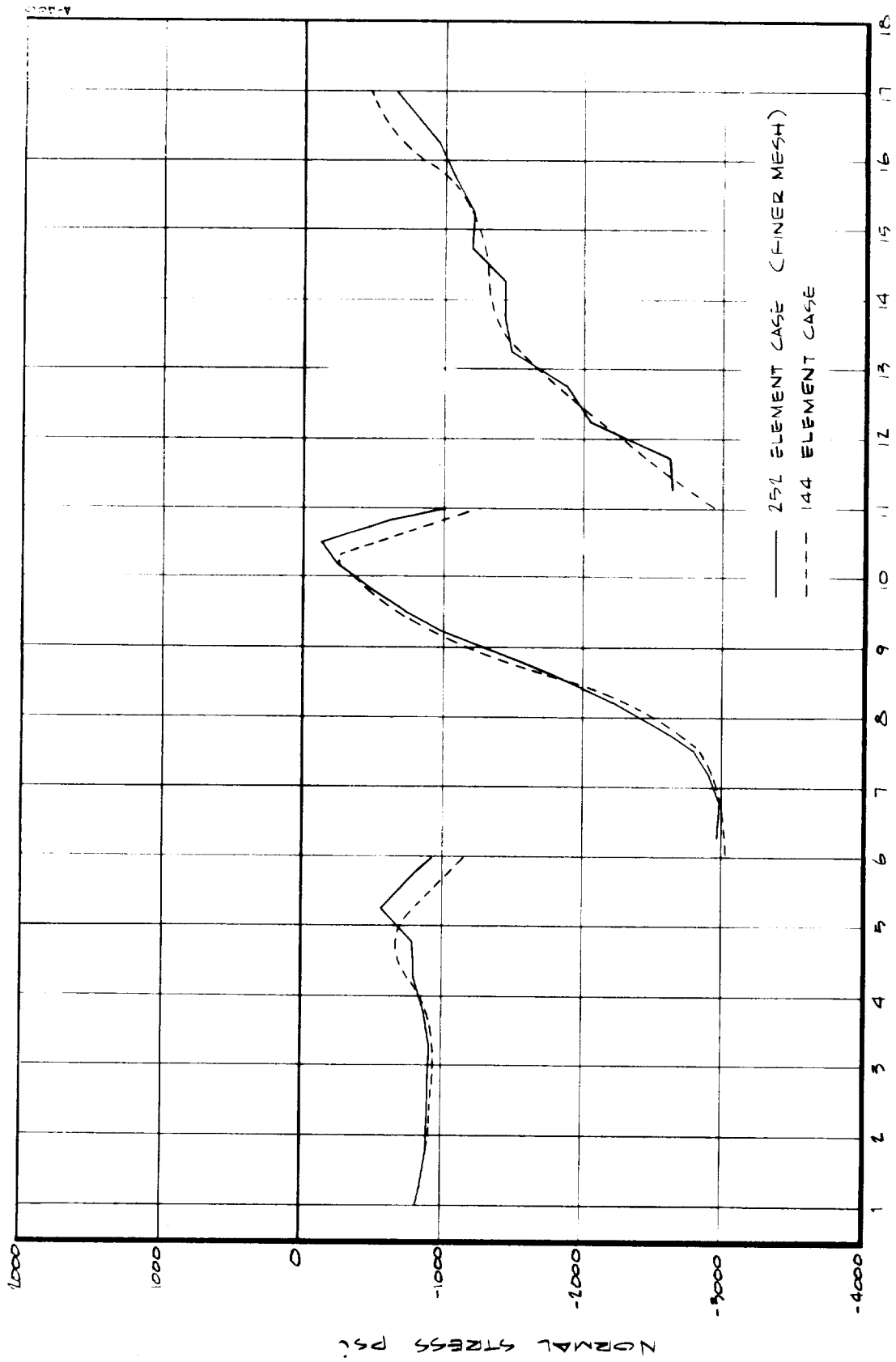

FIGURE 2-35 STRESSES ACROSS THE TAPE DIRECTION FOR ROW OF ELEMENTS BOUNDED BY ISOTHERMS T=960 & T=560 °R (J=3-4)

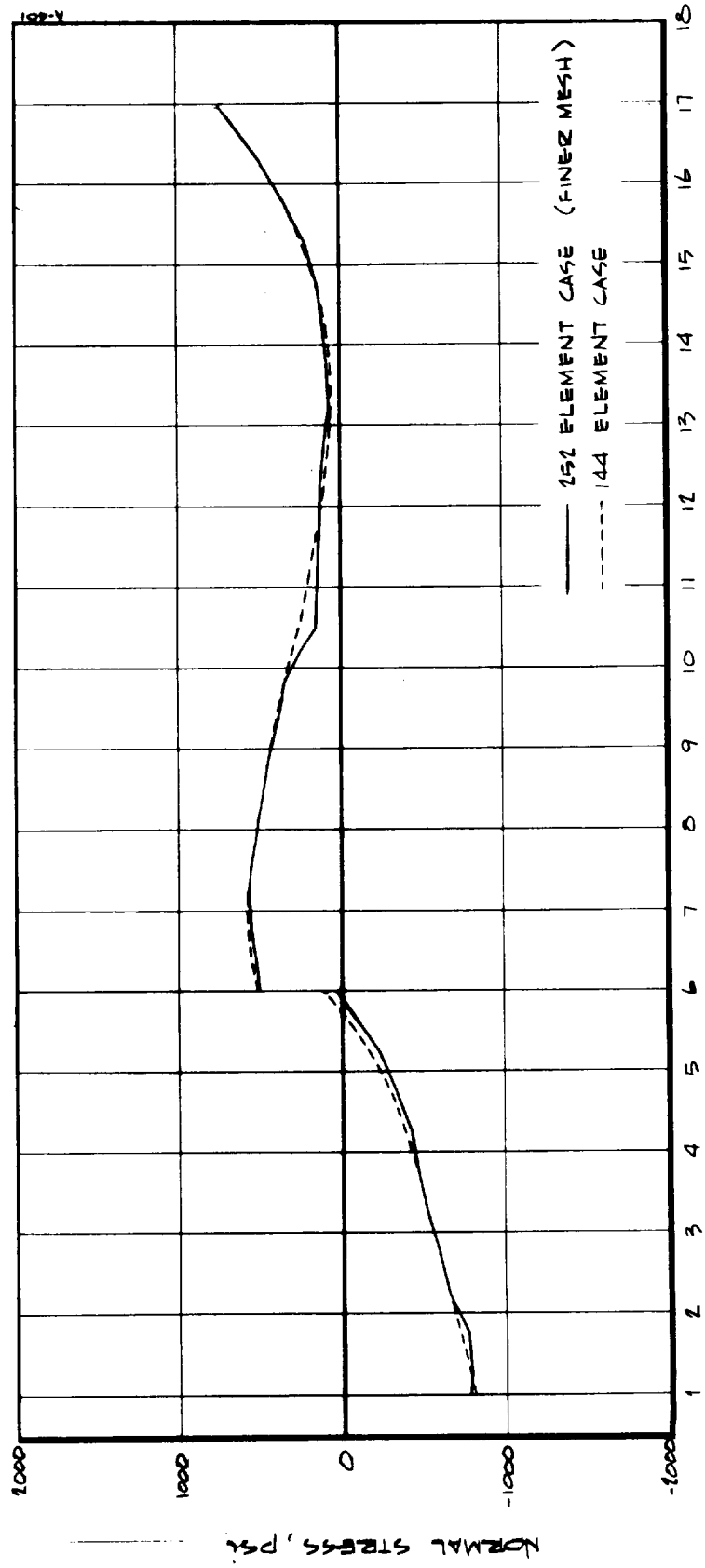

FIGURE 1.36 STRESSES ACROSS THE TAPE DIRECTION FOR ROW OF ELEMENTS BOUNDED BY J=5 & J=6 (T = 530 °R)

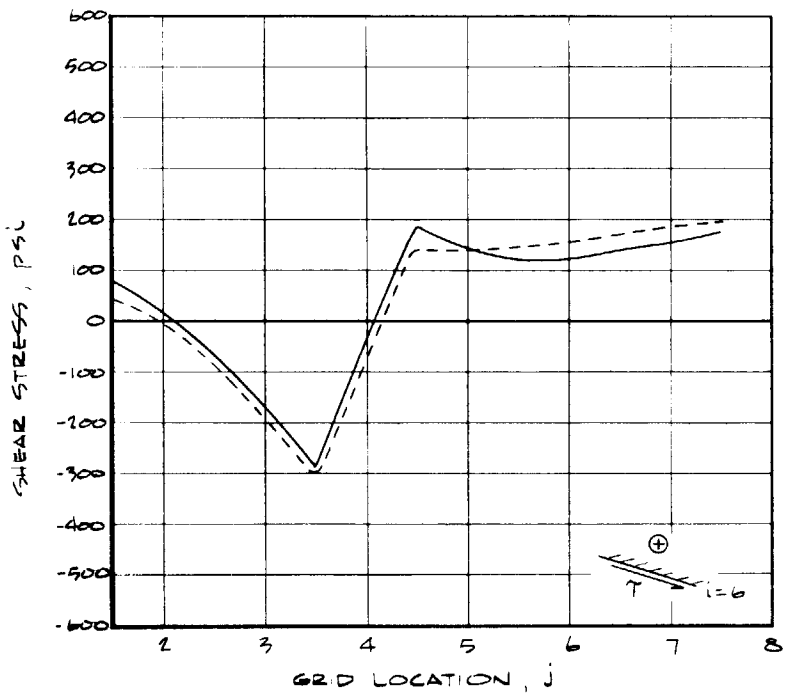

(a) $i = 6$ ($\phi = 0-90$)
(SEE FIGURES 2-20 & 2-22)

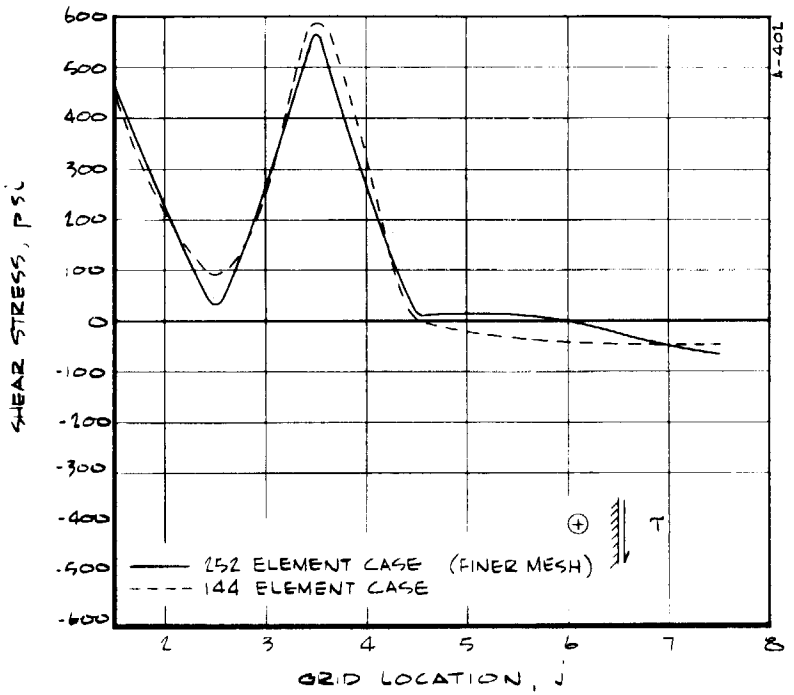

(b) $i = 11$ ($\phi = 90-8$)
(SEE FIGURES 2-20 & 2-22)

FIGURE 2-37 SHEAR STRESS ALONG THE BOND LINES

properties. The isotropic case was calculated for constant property values at both the median and maximum values of the orthotropic properties. The realistic orthotropic treatment of material properties yields a stress picture somewhat different from the isotropic treatment although, if median properties are used with the isotropic assumption, the results for the case considered here are generally reasonably close. Since a generalization of this result may not be valid and since the orthotropic properties must be known to establish median properties for an isotropic approximation anyway, it is recommended that an orthotropic analysis be performed wherever the property data are available.

Figures 2-28 through 2-32 illustrate the effect of the boundary conditions at the artificial boundaries used to isolate the nose region of the nozzle structure. Both completely free and completely fixed boundary constraints were studied. Also, two different locations of the boundaries were studied. First, the nose region was analyzed with artifical boundaries located between bond lines as shown in Figure 2-20. Second, the size of this region was expanded with the artifical boundaries moved so as to coincide with bond lines as shown in Figure 2-21. The effects of the approximate boundary conditions were found to damp out rather quickly away from the boundary location, and, generally speaking, critical stresses in the nose region could be determined with a relatively high degree of confidence from the boundaries assumed in Figure 2-20.

For the smaller of the regions previously analyzed (Figure 2-20), the finite element mesh was subdivided into a network of finer elements as shown in Figure 2-22. Boundary conditions were obtained from the coarse grid analysis of the larger domain (Figure 2-21) and the stress analysis for the specified loading conditions was repeated. The results of this study are shown in Figures 2-33 through 2-37. The stresses given by the coarse grid analysis are seen to be in good agreement with the results of the fine grid study.

Based on these results, the grid size and boundaries of Figure 2-20 (which were used in the pre-fire stress analysis) were adequate and the conclusions drawn therefrom are valid within the constraints of the material property data used to perform and interpret the calculations. These results also provide the necessary criteria for mesh size selection and definition of artificial boundary locations and constraints for future stress calculations.

REFERENCES - SECTION 2

2-1 Two Hundred Sixty-In.-Dia. Motor Program, NASA CR-72287, Aerojet General Corp., June 5, 1967.

2-2 Schaefer, J. and Dahm, T., Studies of Nozzle Ablative Material Performance for Large Solid Boosters. NASA CR-72080, Aerotherm Report No. 66-2, December 15, 1966.

2-3 Kendall, R., A General Approach to the Thermochemical Solution of Mixed Equilibrium-Nonequilibrium, Homogeneous or Heterogeneous Systems. Aerotherm Final Report No. 66-7, Part V, March 14, 1967.

2-4 User's Manual, Aerotherm Charring Material Ablation Program, Version 2, Aerotherm Corporation, January 1966.

2-5 McCuen, P., Schaefer, J., Lundberg, R. and Kendall, R., A Study of Solid-Propellant Rocket Motor Exposed Materials Behavior. Report Number AFRPL-TR-65-33, Vidya Report No. 149, Vidya Division of Itek Corp., February 26, 1965.

2-6 Rindal, R., Clark, K., Moyer, C., and Flood, D. T., Experimental and Theoretical Analysis of Ablative Material Response in a Liquid-Propellant Rocket Engine. NASA CR-72301, Aerotherm Report No. 67-15, Sept. 1, 1967.

2-7 Dergazarin, E., et al., JANAF Thermochemical Tables. Thermal Laboratory, The Dow Chemical Co., Midland, Mich., December 1960 and supplements to date.

2-8 Salmi, R. and Pelouch, J. Jr., Investigation of a Submerged Nozzle on a 1/14.2-Scale Model of the 260-Inch Solid Rocket, NASA TM X-1388, May 1967.

2-9 Private communication with R. J. Salmi, NASA Lewis Research Center, Cleveland, Ohio, January 1967.

2-10 Salmi, R. and Pelouch, J. Jr., Investigation of a Submerged Nozzle for Solid Rockets, Vol. of Papers Presented at ICRPG/AIAA 2nd Solid Propulsion Conference, June 1967, pp. 193-197.

2-11 Dahm, T., A Theoretical Model for Solid Propellant Motor Grain Discharge Pressure Losses. Vidya Technical Note No. 53/C-TN-38, Vidya Division of Itek Corp., November 1962.

2-12 Private communication with R. J. Salmi, NASA Lewis Research Center, Cleveland, Ohio, February 1967.

2-13 Dahm, T. and Schaefer, J., Preliminary Analysis of Ablation Material Performance for Two Lockheed 156-Inch Solid Rocket Motor Nozzles. Vidya Technical Note 8032-TN-1, Vidya Division of Itek Corp., May 21, 1965.

2-14 Back, L., Massier, P. and Gier, H., Comparison of Measured and Predicted Flows through Conical Supersonic Nozzles, with Emphasis on the Transonic Region. AIAA Journal, September 1965.

2-15 Dahm, T. and Schaefer, J., Comparison of Predicted Ablation Material Performance with Firing Results for Two Lockheed Propulsion Company 156-Inch Solid Rocket-Motor Nozzles (U). Aerotherm Technical Note 8032-TN-3, Aerotherm Corp., May 1966. CONFIDENTIAL

2-16 Becker, E. and Brisbane, J., Applications of the Finite Element Method to Stress Analysis of Solid Propellant Rocket Grains, Vols. I and II, Parts 1 and 2, Report No. S-76, Rohm & Haas Company, Redstone Arsenal, Research Div., Huntsville, Alabama, January 21, 1966.

2-17 Wilson, E., Thermal Strain Analysis of Advanced Manned Spacecraft Heat Shields, NASA CR-65062, Aerojet General Corp., September, 1964.

2-18 Pears, C., Engelke, W., and Thornburgh, J., The Thermal and Mechanical Properties of Five Ablative Reinforced Plastics from Room Temperature to 750°F. Technical Report No. AFML-TR-65-133, Southern Research Institute, April 1965.

2-19 Schneider, P., Dolton, T., and Reed, G., Char-Layer Structural Response in High-Performance Ballistic Reentry. AIAA Paper No. 66-424, Presented at 4th Aerospace Sciences Meeting, Los Angeles, California, June 27-29, 1966.

2-20 Private letter communication with J. J. Notardonato, NASA-Lewis Research Center, Cleveland, Ohio, June 9, 1967.

SECTION 3

STUDY OF PROPERTIES AND PERFORMANCE MECHANISMS FOR SILICA PHENOLIC

The properties and performance mechanisms of silica phenolic were studied through the use of the Aerotherm arc-plasma generator as a rocket simulator. This study was performed for three materials:

MX2600 Silica Phenolic

MX2600-96 Silica Phenolic, double thick cloth

MXS-113 Silica Phenolic, random fiber tape

The properties determined were char thermal conductivity at both 0° and 90° layup angles for all three materials. The performance mechanisms studied were surface chemical reactions (including material decomposition), liquid layer run-off, and solid phase chemical reactions.

The results of this study are presented in the following sections. Section 3.1 presents the experimental apparatus and instrumentation. The test conditions are discussed in Section 3.2. Finally, Section 3.3 presents and discusses the properties and performance results.

The scope of the program presented herein was originally planned to include more extensive thermal properties measurements and a more detailed analysis of the test results and performance mechanisms. Experimental problems, which were eventually eliminated, precluded these additional studies, however.

3.1 EXPERIMENTAL APPARATUS AND INSTRUMENTATION

The experimental apparatus consisted of the arc-plasma generator used to simulate the solid propellant combustion products environment, the ablative material test models that were subjected to this environment, and the instrumentation used to measure the test conditions and the material response. The test set-up is shown in Figure 3-1 and discussed below. The arc-plasma generator and support equipment are discussed first in Section 3.1.1. The test models and materials are discussed next in Section 3.1.2. Finally, the instrumentation and data reduction procedures are presented in Section 3.1.3.

3.1.1 Arc-Plasma Generator and Facility

The Aerotherm 1 megawatt constricted arc-plasma generator (APG) shown in Figure 3-2 was used to perform the tests. In the APG, energy is added to the primary test gas via a steady electric arc discharge, the arc striking from

Arc Plasma Generator

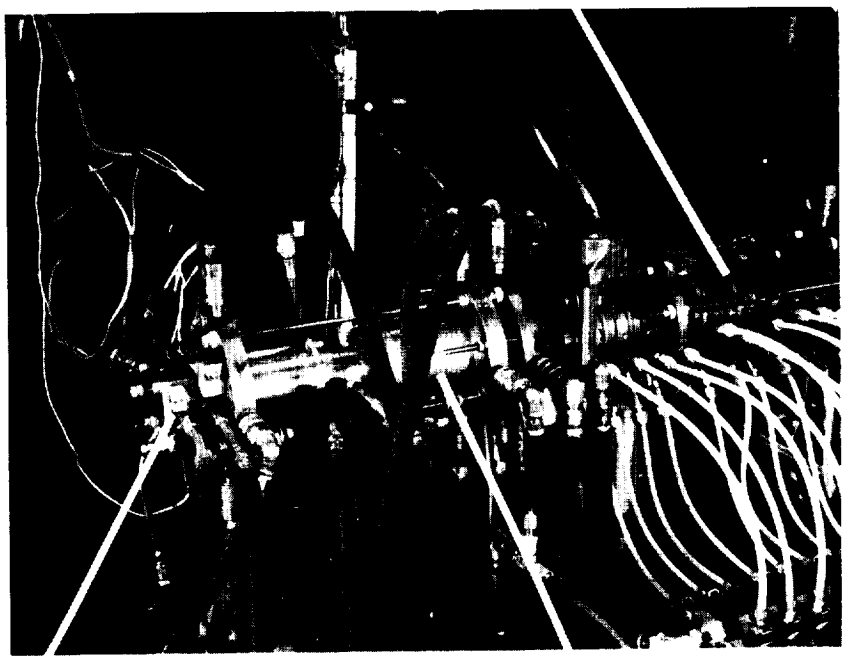

2D Nozzle

Plenum
and Mixing
Chamber

a) Overall View

Figure 3-1 Test Set-Up

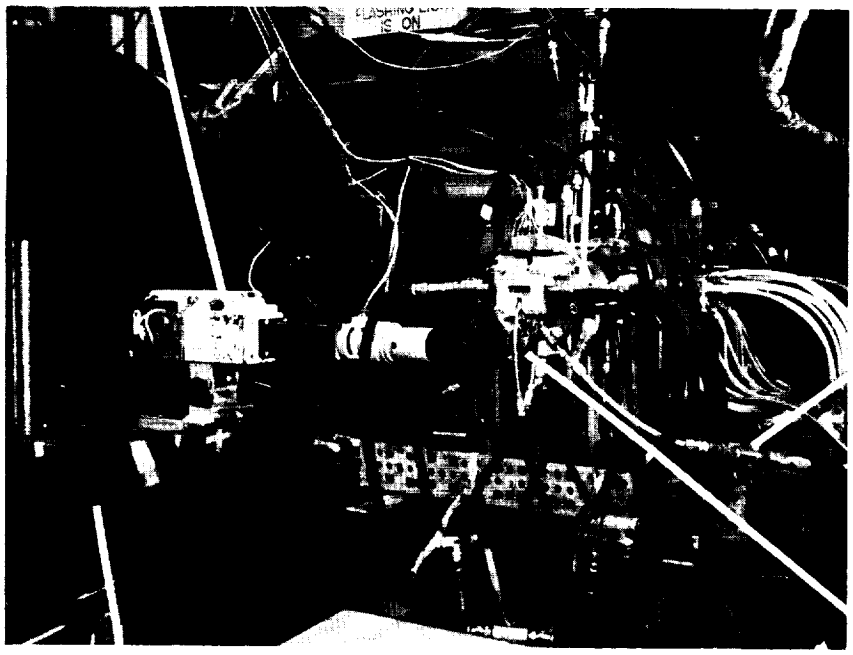

(b) Surface Photography Set-Up

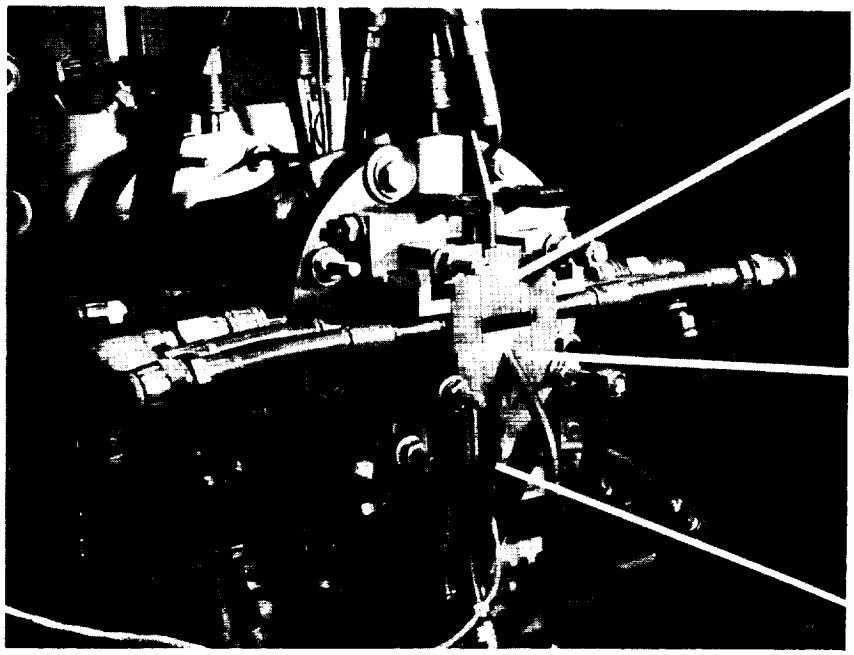

c) 2D Nozzle

Figure 3-1 Concluded

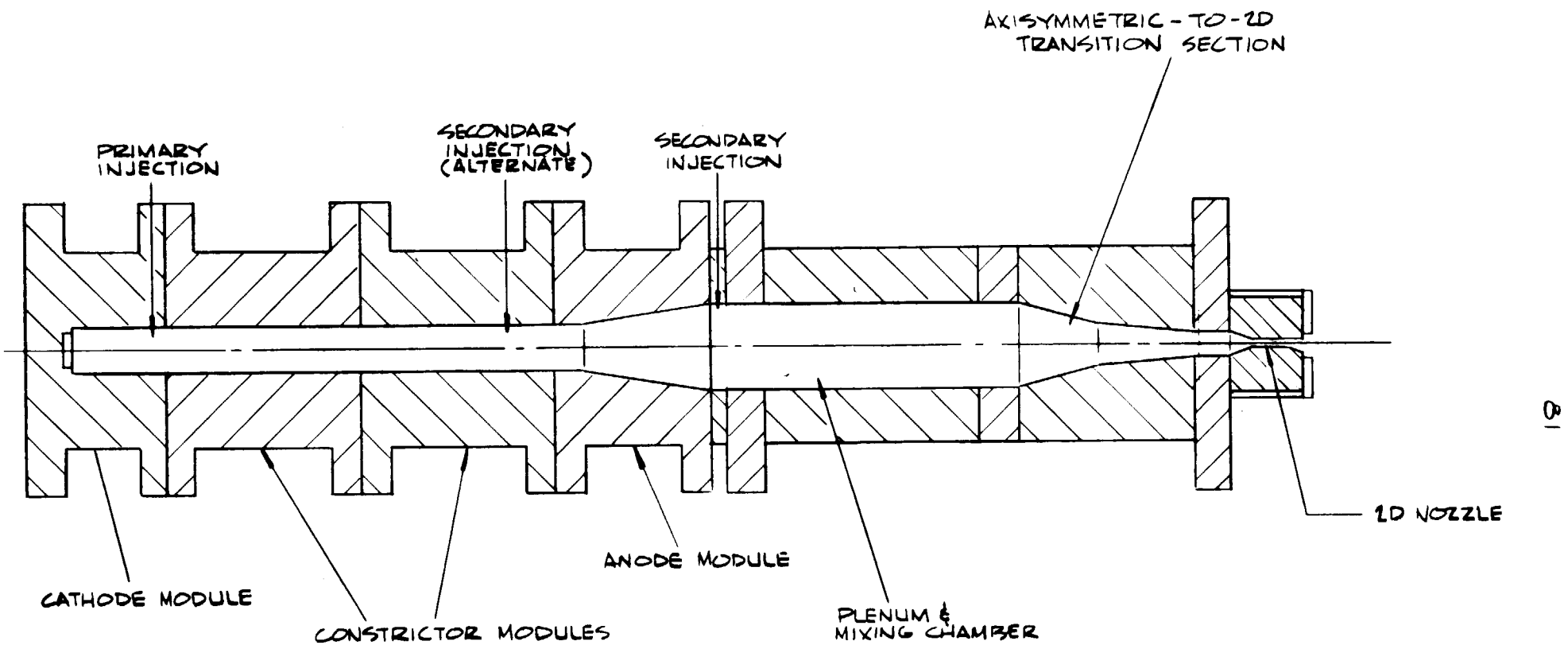

FIGURE 3-2 AEROTHERM CONSTRICTOR ARC,
ROCKET SIMULATOR CONFIGURATION

the tungsten cathode in the cathode well to the downstream converging-diverging anode. The primary gas is introduced tangentially through an insulator separating the cathode well from the first insulated constrictor segment to provide stable, high voltage operation. The secondary gas is introduced in the upstream end of the plenum-mixing chamber downstream of arc heating to yield the desired final gas composition and to insure equilibration of the primary and secondary gases before they exhaust through the two-dimensional test section. The actual gases used in this test program are presented in Section 3.2, Test Conditions.

The arc unit is water cooled with high pressure deionized water. The electric power for the tests performed under this program was supplied by a direct current diesel electric generator. This unit has a maximum rated output level of 746 kilowatts of dc power (1000 brake horsepower) for continuous operation. The power output and open circuit voltage are continuously variable, the maximum open circuit voltage being 1000 volts. A step-wise variable ballast resistor in series with the arc provides the necessary arc electrical stability.

Arc starting is accomplished by generating a high frequency discharge (RF) across the insulating ring separating the cathode from the first constrictor disk. Upon starting in this region, the arc automatically jumps to the cathode button and is forced to transfer to the anode downstream. Starting is usually accomplished at a lower power level and gas flow rate than desired for the final test conditions. After starting, final power and flow rate adjustments are made to achieve the desired test conditions. This is accomplished within 8 seconds of arc ignition.*

The constrictor arc in its present configuration is capable of 12 atmosphere chamber pressures for arc-heated nitrogen, helium, nitrogen-helium mixtures. This chamber pressure limit is associated with the tungsten cathode; degradation in the form of material loss at the surface occurs at higher chamber pressures.

3.1.2 Test Materials and Models

Three silica phenolic materials were used in the test program: MX2600, MX2600-96, MXS-113, the last two being low cost materials. The MX2600 material is a nominal 30 percent resin content material while the MX2600-96 material is basically the same although the cloth is double-thickness thus reducing

*A new technique has recently been developed by Aerotherm under Contract NAS3-10291 which eliminates this starting transient. The flow by-passes the test section until the desired test conditions are reached; the by-pass system is then closed and the test section system opened to start the test.

the time required to wrap a given part. The MXS-113 material is a random fiber tape which provides a cost reduction through the use of fibers instead of a cloth. The nominal resin content is high, 60 percent, to provide the required fiber wetting by the phenolic resin and the necessary tape wrapping characteristics. The two lower cost materials therefore represent cost reduction in fabrication and cost reduction in raw materials, respectively. The MX2600-96 material has been used successfully on an Air Force low cost materials program (Reference 3-1); the MXS-113 material has not been similarly evaluated to our knowledge.

The materials were obtained in the form of tape wrapped rings which were wrapped and cured by large ablative part standards by the Fiberite Corporation. The rings were approximately 8 inches in inside diameter and approximately 10 inches in outside diameter (see Figure 3-3). This approach eliminated the non-representative fabrication technique, the layup angle limitations and other problems noted in Reference 2-2 and associated with the small axisymmetric nozzle configuration in that study.

The test configuration was a two-dimensional (2D) nozzle in which the ablative material test section formed one side of the nozzle as shown in Figures 3-4 and 3-5. This test configuration allowed the test section to have a geometric configuration similar to and to be fabricated in the same fashion as a large ablative nozzle part. The side plates on either side of the model that, together with the model, formed the top flow surface were of the same material as the test material and eliminated edge effects in the actual test model. Each model contained either 1 or 4 thermocouples in depth; the thermocouple installation details are presented in Figure 3-4. Layup angles of 0° and 90° were used in char thermal conductivity determination for all 3 materials. For the study of performance mechanisms, a 20° layup angle was used for all tests for the 3 materials.

3.1.3 Instrumentation and Data Reduction

Instrumentation for the test program had two functions: determination of the test conditions and measurement of the material response.

The test conditions are defined by the gas total enthalpy, the chamber pressure, and, from these two, the chamber temperature. The enthalpy was determined from an energy balance on the arc-plasma generator. The power input to the arc unit was measured every 0.72 seconds through measurements of arc current, with a precision shunt, and arc voltage, with a calibrated voltage divider. These outputs were fed to an analog-to-frequency converter with paper tape digital readout. The energy loss to the cooling water was determined from the measurement of flow rate and temperature rise of the water

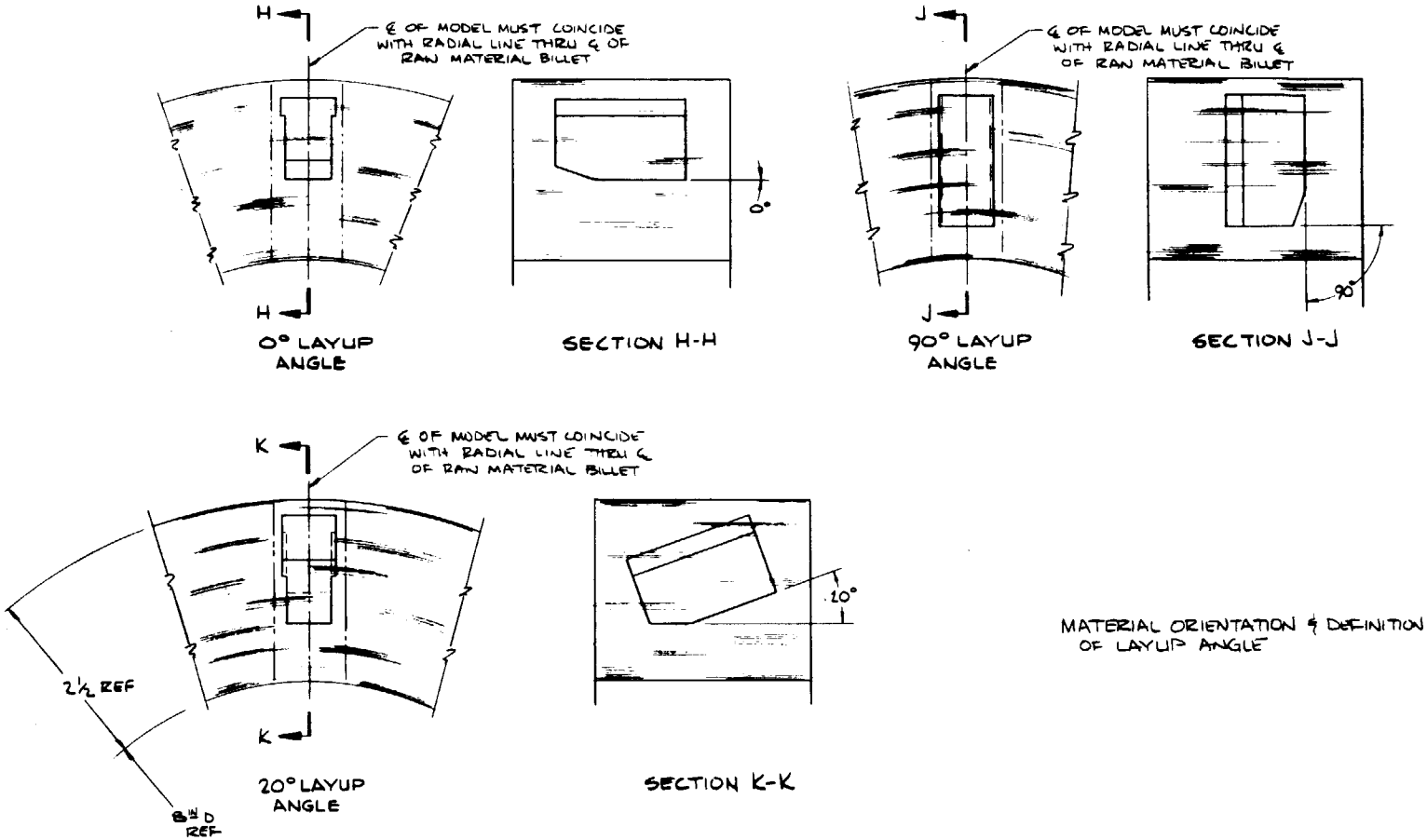

FIGURE 3-3 TAPE WRAPPED RING AND MODEL FABRICATION SCHEMATIC.

A88

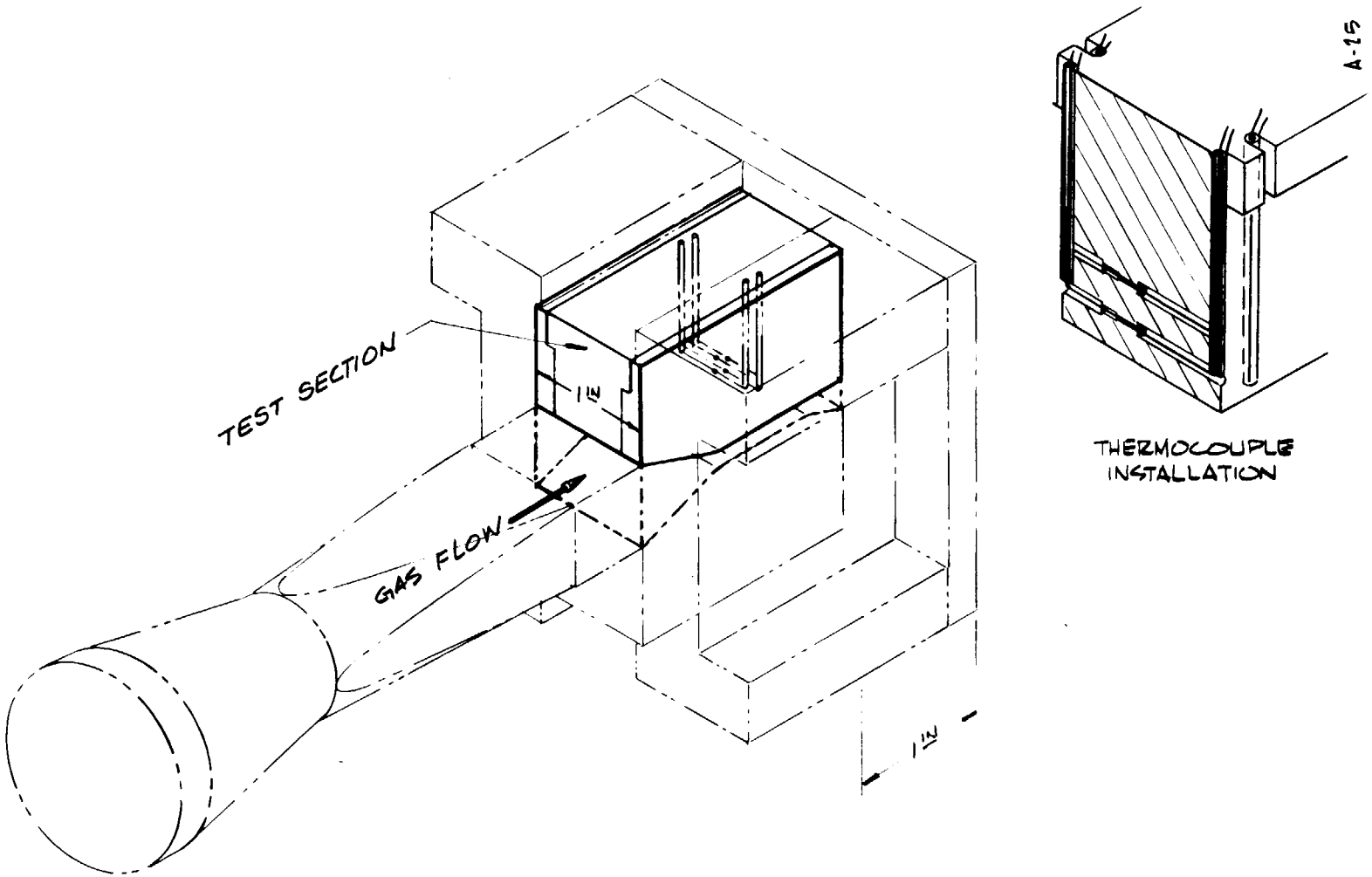

FIGURE 3-4 TYPICAL INSTRUMENTED TWO-DIMENSIONAL NOZZLE TEST SECTION.

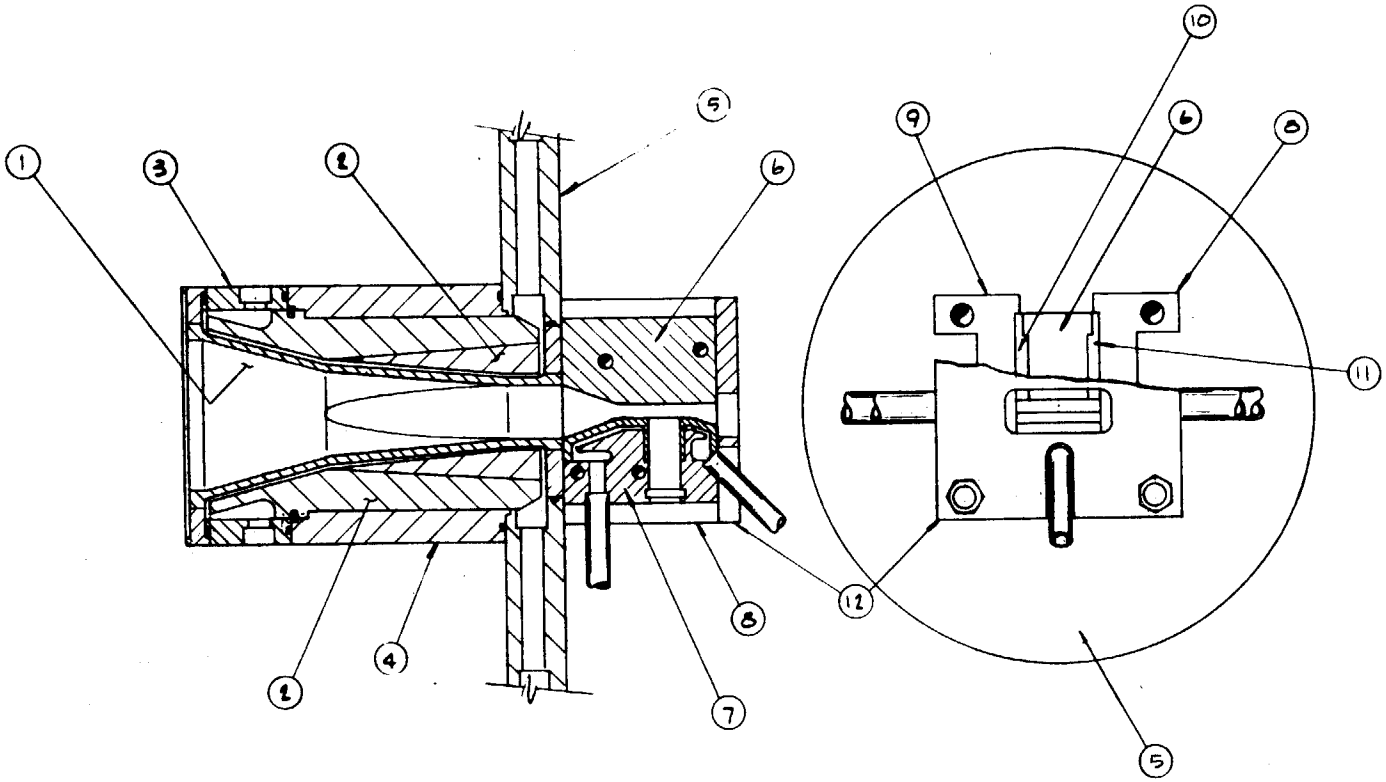

1. AXISYMMETRIC-TO-2D TRANSITION SECTION
6. TEST MODEL
7. CALORIMETER & VIEWPORT HOUSING
10. SIDE PLATE
11. SIDE PLATE

FIGURE 3-5 AXISYMMETRIC-TO-2D TRANSITION SECTION AND TEST SECTION

passing through the arc heater assembly (see Figure 3-2). The cooling water flow rate was measured by a calibrated standard ASME orifice meter whose pressure drop was observed during tests. The water temperature rise was measured by a differential thermopile, the output of which was recorded on a 36-channel oscillograph. The total gas flow rate was measured by visual readings of the differential pressures across calibrated standard ASME orifice meters, one for the primary and one for the secondary gas. The gas total enthalpy was then calculated from the following energy balance equation

$$h_o - h_{ref} = \frac{EI - \dot{m}_{coolant}\left[c_p(\Delta T) - \frac{\Delta p}{\rho}\right]}{\dot{m}_{gas}} \qquad (3\text{-}1)$$

where h_{ref} is the ambient or room temperature enthalpy of the test gases.

The chamber pressure was measured by a calibrated strain gauge total pressure transducer, the output of which was recorded continuously on the oscillograph. The pressure tap was located at the downstream end of the plenum chamber. The chamber temperature was determined from the calculated enthalpy and measured chamber pressure through equilibrium Mollier charts that were developed for the test gas mixtures (Reference 2-5). The time base for each firing was determined from the oscillograph record which accurately defined on-time and off-time and included a correlation signal between the digital output and the oscillograph output.

Prior to the model tests, calibration tests were performed in which static pressure and cold wall heat flux were measured in the test section. A water cooled pressure tap section identical to the model was used for these tests. Pressure was measured in the throat region of the 2D nozzle at the same axial location as the thermocouple instrumentation in the test models (see Figure 3-4). The method of pressure measurement was identical to the chamber pressure measurement discussed above. Directly opposite from the pressure tap, a Gardon-type calorimeter measured heat flux by continuously recorded output on the oscillograph. For some model tests this calorimeter was interchanged with a quartz window viewing port to allow detailed motion picture photography of the surface response. The view port details are presented in Figure 3-6. The window was made from a quartz microscope glass slide and the window surface was protected by a small bleed flow of nitrogen. A number of rather remarkable motion pictures were obtained at 100 psia chamber pressure showing the liquid layer runoff.

The ablative material response at the throat of the test section was measured directly or indirectly in terms of surface temperature history, surface erosion history, and internal temperature histories at either one or

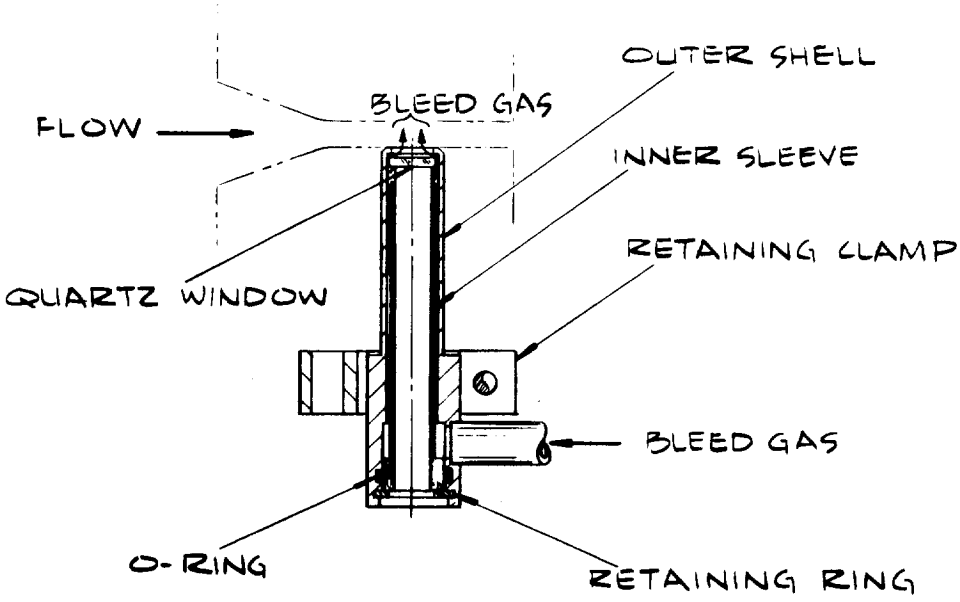

FIGURE 3-6 VIEW PORT ASSEMBLY (USED INTERCHANGEABLY WITH CALORIMETER).

four locations in depth (see Figure 3-4). Also, measurements of surface recession were made and measurements of char depths and pyrolysis zone depths were made on the sectioned test models. The surface temperature was measured continuously with a recording optical pyrometer. The pryometer senses brightness temperature in the near infrared at a wavelength of about 800 millimicrons. The pyrometer was sighted up the test section exit to a point on the model at or close to the axial location of the thermocouple instrumentation. The view field was a spot approximately 0.085 inch in diameter. The brightness temperature recorded corresponded to a surface emissivity of 1.0; the recorded data were corrected to an emissivity of 0.85 for reporting herein. The pyrometer output was recorded continuously on the oscillograph.

Internal temperatures were measured utilizing an instrumentation technique developed to yield accurate temperature data in low conductivity materials such as those considered herein. The thermocouple wires were inserted into the test models so that they were aligned with the isotherms and the thermocouple wires were of small diameter, 0.005 inch. This minimized thermal conduction away from the thermocouple junction, an effect which results in a lower-than-actual indicated temperature. Also, to insure intimate contact of the thermocouple junction and the material, the thermocouple beads were bottomed against a counterbored hole in the material as shown in Figure 3-4. Finally, to minimize the disturbance to the heat flow caused by the wire holes, the smallest drills as practical were used.

Ceramic insulators 0.035 inch in diameter enclosed the wire for the two thermocouples closest to the model surface in the direction of heat flow. This protected the first two thermocouples from shorting to the second two thermocouples, and also prevented short circuits to the conducting char. Similar ceramic insulators were not needed for the two deep thermocouples since the material char depth never reached as deep as the third thermocouple. The nominal thermocouple locations for all instrumented nozzles were presented as in the table below (also see Figure 3-4). The exact locations were determined

THERMOCOUPLE DEPTHS FROM EXPOSED SURFACES
(inch)

Thermal Conductivity Models	Performance Mechanisms Models
0.060	0.200
0.120	
0.200	
0.300	

from an X-ray photograph of the model. The maximum error in these measured locations is felt to be $\pm$0.004 inch. The technique used for accurately

defining the locations from the X-ray photographs was as presented in Reference 2-5 and is not repeated here. At the two nearest-to-the-surface locations (Figure 3-4), tungsten 5% rhenium-tungsten 26% rhenium thermocouples were used; they are accurate at temperatures up to about 4200°F (4660°R). At the other two locations, Chromel-Alumel thermocouples were used; they are accurate at temperatures up to about 2500°F (2960°R). The thermocouple outputs were recorded continuously through each firing and for 2 to 3 minutes into the cool-down period.

3.2 TEST CONDITIONS

In the study of the performance mechanisms of silica phenolic, it was desired to duplicate as nearly as possible the material response that would actually occur in the rocket nozzle application. The rocket nozzle condition and material response to these conditions were therefore defined for a typical exit cone application. The test conditions and test gases were then selected to provide a close duplication of these actual conditions and material response. The 260-SL-3 motor was used as a basis for definition of the test conditions and gases; typical exit cone conditions for the 260-SL-3 nozzle (locations I and J of Figure 2-3) are summarized in Table 3-1.

Several gas mixtures were considered for the test gases in the two phases of the experimental program. These mixtures are presented in Table 3-2 together with the chemical composition of the ANB-3254 propellant.* Mixtures 4 and 3A simulate the thermodynamic and chemical aspects of the Aerojet ANB-3254 propellant whereas the other mixtures simulate only the thermodynamic aspects. Chemical simulation corresponds to duplication of the available oxygen in the propellant and, for Mixture 3A, the available hydrogen as well (see References 2-2 and 2-5). Calculations were performed using the ACE computer program to define the response of the three silica phenolic materials to the above environments. In all calculations, surface chemical reactions and melt removal were considered as the surface recession mechanisms. The results of these calculations are presented in Figure 3-7 for the two MX2600 materials in terms of the dimensionless char removal rate, $\dot{m}_c/\rho_e u_e C_M (=\dot{s}\rho_c/\rho_e u_e C_M)$, versus surface temperature. The steady state surface recession rate and surface temperature were also determined through the use of the Steady State Charring Material Ablation Computer Program (SSCMA).** These results are

*The aluminum and appropriate amount of oxygen have been eliminated from this composition since essentially all the aluminum is tied up in condensed phase Al_2O_3.

**Background information on the steady state solution technique and the SSCMA program is presented in Section 4.1.

TABLE 3-1

TYPICAL EXIT CONE CONDITIONS FOR THE 260-SL-3 NOZZLE

Gas System	Chamber Pressure (psia)	Area Ratio	Local Conditions			
			Static Pressure (psia)	Static Temperature (^{o}R)	Heat Transfer Coefficient (lb/ft^2sec)	Wall Shear (psi)
ANB-3254 propellant	500	1.9	68	4550	0.18	0.20
		2.8	39	4200	0.11	0.14

TABLE 3-2

SIMULATION TEST GASES CONSIDERED IN THE STUDY OF SILICA PHENOLIC PERFORMANCE

Gas System	Elemental Mass Fractions					
	H	He	C	N	O	Cl
ANB-3254 propellant	0.056	-	0.172	0.120	0.360	0.292
Mixture 3A	0.052	-	-	0.815	0.133	-
Mixture 4	-	0.228	-	0.619	0.153	-
Mixture 5	-	0.224	-	0.776	-	-
Mixture 6	-	0.231	-	0.539	0.230	-
Mixture 7	-	0.226	-	0.699	0.075	-

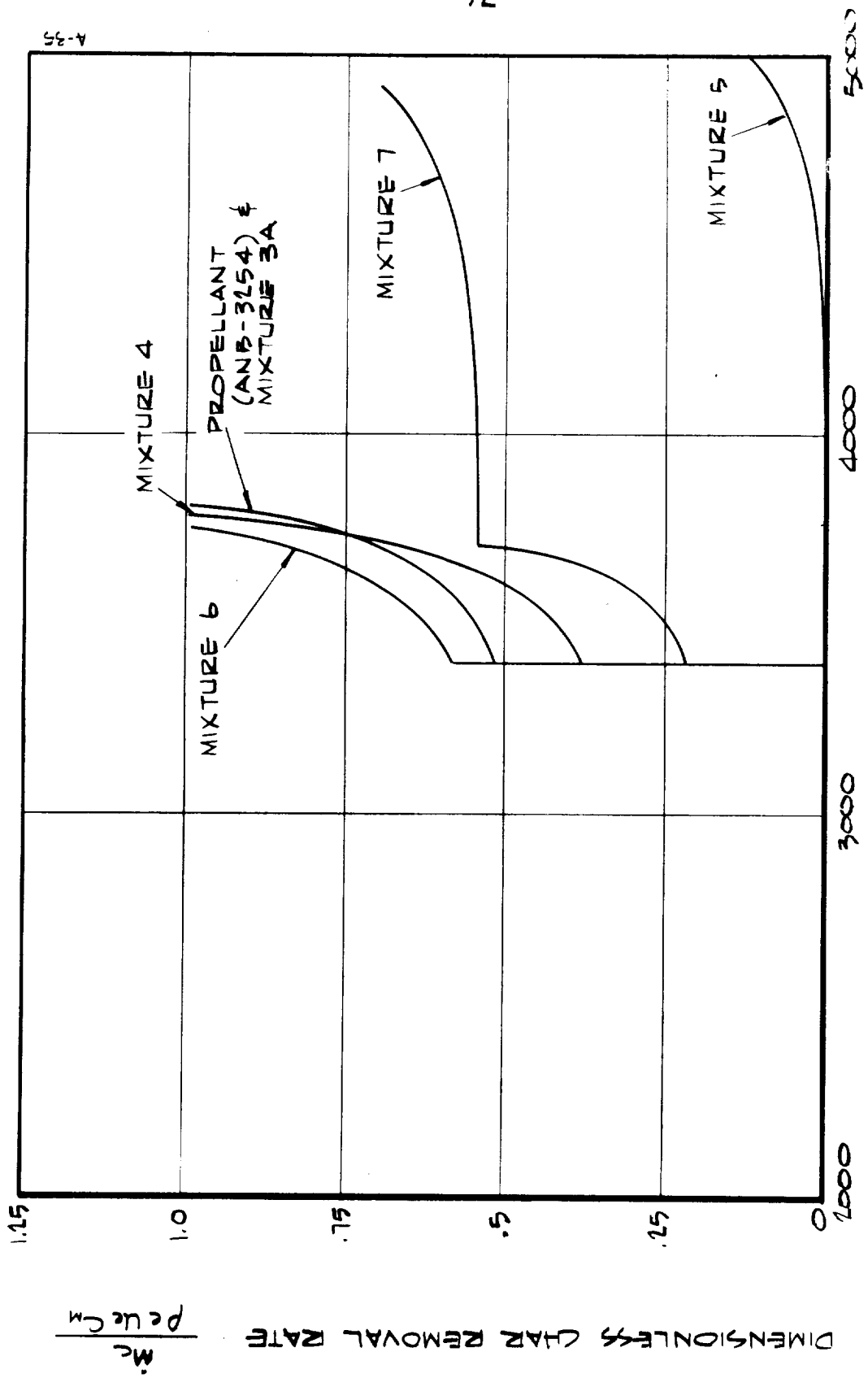

FIGURE 3-7 RESPONSE OF SILICA PHENOLIC (32 PERCENT RESIN FRACTION TO THE ANB-3154 PROPELLANT AND SEVERAL GAS MIXTURES

presented in Table 3-3. On the basis of the comparisons available in Table 3-3 and Figure 3-7, Mixture 4 was selected as the test gas for the material performance tests. The response of silica phenolic to this gas mixture is close to that of the actual propellant, exhibiting a slightly lower surface recession rate for Mixture 4. Note that Mixture 3A is an alternate choice but was not used because of the safety hazards involved with hydrogen.*

In the tests to define char thermal conductivity, the surface recession rate must be known as part of the data reduction procedure. This is, of course, most accurately defined if the recession rate is zero or small. On this basis, Mixture 5 was selected for use in the thermal conductivity tests; as seen from Table 3-3 and Figure 3-7, the anticipated recession rate was zero.

The nominal test conditions selected for the test program are presented in Table 3-4; comparison with the conditions for the 260-SL-3 nozzle demonstrates the expected close duplication of exit cone conditions. Wall shear was also considered in defining the test conditions since, for silica, it may affect the liquid layer runoff. Note that the Mixture 5 inert environment test results of the thermal conductivity study provide "off condition" information for the performance mechanisms study. In all tests, the firing times were approximately 60 seconds.

3.3 MATERIALS PROPERTIES AND PERFORMANCE RESULTS

The test results under the study of the properties and performance mechanisms for silica phenolic are presented and discussed in the following sections. The char thermal conductivity results are presented in Section 3.3.1 and the performance mechanisms results are presented in Section 3.3.2. The test models, the test conditions, and the test results for both program phases are summarized in Table 3-5.

3.3.1 Char Thermal Conductivity

The char thermal conductivity was determined for:

MX2600 Silica Phenolic
MX2600-96 Silica Phenolic
MXS-113 Silica Phenolic

at the extremes in layup angle, 0° and 90°. Before presenting the test results, some background comments are appropriate. The conductivity was determined by the dynamic technique presented and used in Reference 2-2. In this technique, arc plasma generator test firings are performed on test models instrumented with several thermocouples in-depth at conditions typical of the

*No other operational problems exist for Mixture 3A, however.

TABLE 3-3

STEADY STATE SILICA PHENOLIC PERFORMANCE
(32 PERCENT RESIN FRACTION) FOR THE VARIOUS GAS MIXTURES

Gas System	Local Pressure (psia)	Static Temperature (^{o}R)	Surface Recession Rate[a] (mils/sec)	Surface Temperature[a] (^{o}R)
ANB-3254 propellant	55	4550	11.5	3640
Mixture 3A			9.7	3430
Mixture 4			9.4	3610
Mixture 5			0	4410
Mixture 6			15.5	3610
Mixture 7			0	4590

a) Heat transfer coefficient = 0.20 $lb/ft^2 sec$.

TABLE 3-4

NOMINAL ARC PLASMA GENERATOR TEST CONDITIONS

Mixture	Chamber Pressure (psia)	Chamber Temperature (^{o}R)	Enthalpy (Btu/lb)	Test Section Conditions: Static Pressure (psia)	Static Temperature (^{o}R)	Heat Transfer Coefficient ($lb/ft^2 sec$)	Wall Shear (psia)
4	100	5600	2700	56[a]	4550[a]	0.20[d]	0.19[d]
5	|	|	2550	54[a]	|	|	0.20[d]
4	50	5500	2700	28[a]	4500[a]	0.12[d]	0.11[d]
5	|	|	2550	27[a]	|	|	|
260-SL-3 Nozzle - ANB 3254 Propellant				68[b]	4550[b]	0.18[e]	0.20[e]
				39[c]	4200[c]	0.11[e]	0.14[e]

a) Sonic conditions
b) $A/A_* = 1.9$
c) $A/A_* = 2.8$
d) Estimated
e) Calculated average value

TABLE 3-5

SUMMARY OF TEST CONDITIONS AND TEST RESULTS

Program Phase	Model No.	Silica Phenolic Material Specs Type	Layup Angle	Enthalpy (Btu/lb)	Chamber Pressure (psia)	Cold Wall Heat Flux (Btu/ft^{2}sec)	Hot Wall Heat Transfer Coefficient (lb/ft^{2}sec)	Wall Shear (psi)	Chemical Environment Gas Mixture	Exposure Time (sec)	Surface Recession (inch)	Average Surface Recession Rate (mils/sec)	Char Thickness (inch)	Pyrolysis Zone Thickness (inch)	Average Surface Temperature ($^\circ$R)	Mass Loss (gm)	Instrumentation[a]
Performance Mechanisms	10d	MX2600	20°	2500	105.0	251	.074	.072	4	60.5	0.014	0.2	0.305	0.025	3525	2.651	1TC, Cal
	12d			2630		264				60.3	-0.007	--	0.240	0.020		1.500	1TC, Photo
	11d			2840	56.1	173	.045	.044		60.9	-0.020	--	0.255	0.025	3575	1.025	1TC, Cal
	8d			2590	57.8	159				60.8	-0.011	--	0.240	0.040	3550	1.230	1TC, Photo
	7d			2600	100.0	252	.071	.069	5	60.7	-0.017	--	0.200	0.035	3400	1.093	
	9d			2780	54.5	169	.045	.044			-0.016	--	0.220	0.030	3125	0.961	
	17d	MX2600-96		2530	108.0	261	.076	.074	4	60.3	-0.010	--	0.275	0.035	3200	1.505	1TC, Cal
	19			2650	104.0	264	.073	.071		60.5	-0.007	--	0.260	0.025	3450	1.306	1TC, Photo
	15d			2560	57.4	157	.045	.044		60.4	-0.016	--	0.240	0.040	3525	1.053	1TC, Cal
	16d			2530	63.8	170	.049	.047		60.6	-0.017	--	0.280	0.030	3475	1.243	1TC, Photo
	24d	MXS-113		2620	89.8	233	.065	.063		60.1	0.098	1.6	0.200	--	3800	3.907	1TC, Cal
	21d			2700	90.2	240				60.6	0.085	1.4	0.210	--	3675	3.788	1TC, Photo
	22d			2650	49.3	145	.040	.039		60.8	0.031	0.5	0.205	--	3500	2.338	1TC, Cal
	26			2880	48.2	155				60.6	0.030		0.200	--	3300	2.300	1TC, Photo
Thermal Conductivity	1	MX2600	0°	2520	104.0	251	.073	.071	5	61.0	-0.008	--	0.255	0.025	3625	1.703	4TC, Cal
	2		90°	2600	98.8	252	.071	.069		60.7	0.022	0.4	0.260	0.060	4000	1.874	
	3	MX2600-96	0°	2540	101.0	248	.072	.070		60.8	-0.014	--	0.230	0.035	3450	1.176	
	4		90°	2480	102.0	244				60.7	0.018	0.3	0.290	0.030	3800	1.654	
	27		20°	2450	97.6	231	.069	.067		60.2	-0.017	--	0.260	0.045	3900	1.467	
	5d	MXS-113	0°	2410	96.7	225				60.7	0.010	0.2	0.240	--	3675	3.483	
	6d		90°	2420	89.8	215	.065	.063		60.5	0.014		0.270	--	3500	3.049	

a) TC indicates thermocouple, Cal indicates heat flux calorimeter, and Photo indicates surface motion picture photography

material application in a rocket nozzle. In the tests performed herein the models formed one wall of a two-dimensional nozzle which was the exit nozzle of the APG (Figures 3-2 and 3-4), four in-depth thermocouples were used (Figure 3-4), and the test conditions simulated the exit cone conditions of a large solid booster (Tables 3-4 and 3-5). The data reduction procedure is a parametric input of conductivity (as a function of temperature) to the Charring Material Ablation (CMA) Computer Program, with the measured surface temperature and surface recession rate histories also input, until the predicted internal temperature histories agreed closely with those measured. The technique is discussed further in Reference 2-2.

For low conductivity composite materials such as silica phenolics, the material conductivity in the partially degraded state is typically lower than that in the virgin and fully-charred states.* For example, the thermal conductivity "history" for a given in-depth location during transient heating might look as shown in the sketch below. In order to handle this effect

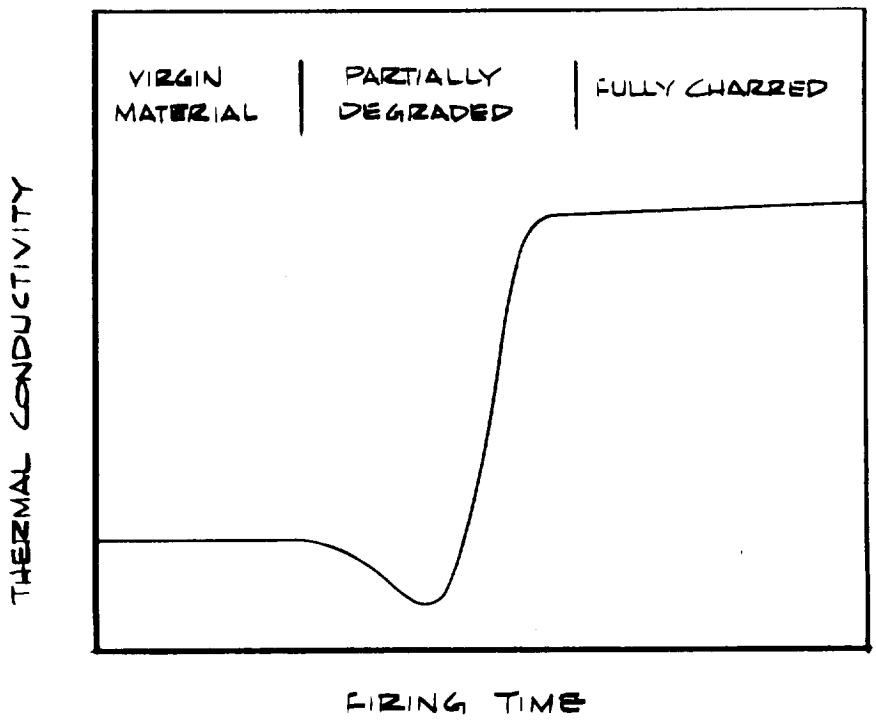

computationally, weighting functions on the virgin material and char conductivity values that are related to the degradation state (e.g., density) were

*The results of References 3-2 and 3-3 exhibit this effect for nylon phenolic and for Avcoat 5026-39HCG (the Apollo heat shield material), respectively.

proposed and used in the program of Reference 2-6. This conductivity model is physically reasonable and was the model used herein.

The virgin material and char thermal conductivities for MX2600, MX2600-96, and MXS-113 silica phenolic are presented in Figures 3-8 through 3-10, respectively, and in Table 3-6. The weighting functions on the virgin material and char conductivities are also included. The general expression for conductivity which applies to these results is

$$k = f_1(x)\ k_p(T) + f_2(x)\ k_c(T) \qquad (3\text{-}1)$$

where k_p and k_c are the temperature dependent virgin material and char conductivities, respectively, x is the undegraded material mass fraction (x = 1 for virgin material, x = 0 fully-charred material), and f_1 and f_2 are the degradation dependent weighting functions on the virgin material and char conductivities, respectively. Note that the conductivities are functions of layup angle whereas the weighting functions f_1 and f_2 are not. The virgin material conductivity was obtained for MX2600 silica phenolic directly from Reference 2-18. The virgin material conductivity for the other two materials was assumed to be the same as that for MX2600. The char conductivities and weighting functions were determined from the test results by the dynamic technique discussed above. These results are valid to about 3500°R and have been extrapolated to 5000°R. Note that Table 3-6 contains all chemical, physical, and thermal property data used as input to the CMA program and provides the necessary data for future calculations of material response.

The comparison of calculated and measured internal temperature histories using the conductivity results presented above is shown in Figure 3-11 through 3-13 for all three materials at 0° and 90° layup angles in each. The agreement between predicted and measured temperatures is good in all cases. Based on this agreement the conductivity results of Figures 3-8 through 3-10 and Table 3-6 are felt to be adequate for engineering calculations of material performance.

The three materials exhibit quite different variations of conductivity. For MX2600 and MX2600-96, the char conductivities at the 90° layup angle are the same but for the 0° layup angle the MX2600-96 conductivity is lower. Apparently the thicker cloth in MX2600-96 represents a greater barrier to heat flow in the cross-ply direction than the thinner cloth in MX2600. The MXS-113 random fiber material exhibits a high char conductivity close to that of carbon phenolic (Table 2-3); at 0°, it exhibits a low conductivity typical of the other two silica phenolics.

The conductivity of MXS-89 silica phenolic at 90° layup angle was also determined in the program of Reference 2-6 by the same technique as used

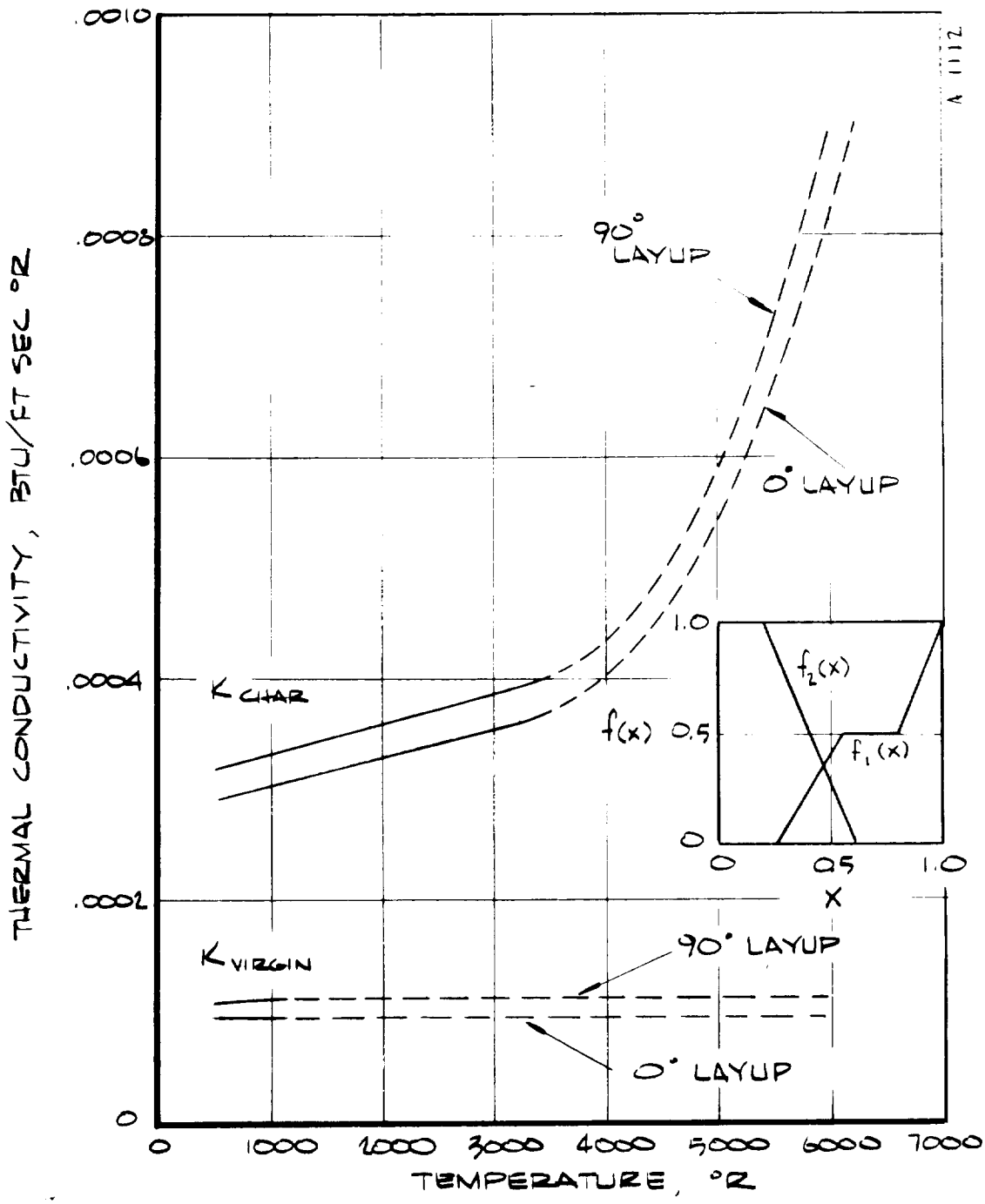

FIGURE 3-8 THERMAL CONDUCTIVITY FOR MX2600 SILICA PHENOLIC

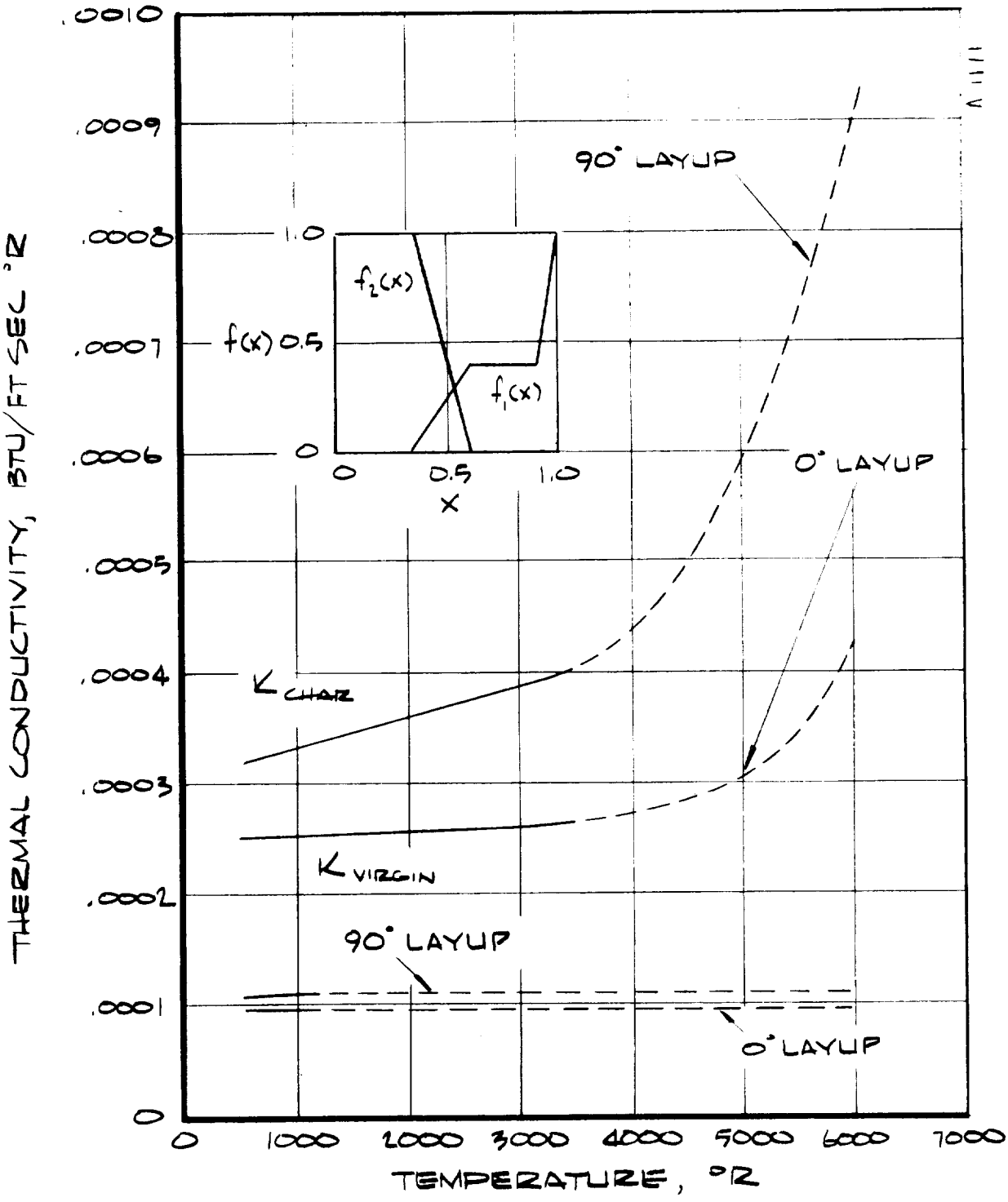

FIGURE 3-9 THERMAL CONDUCTIVITY FOR MX2600-96 SILICA PHENOLIC

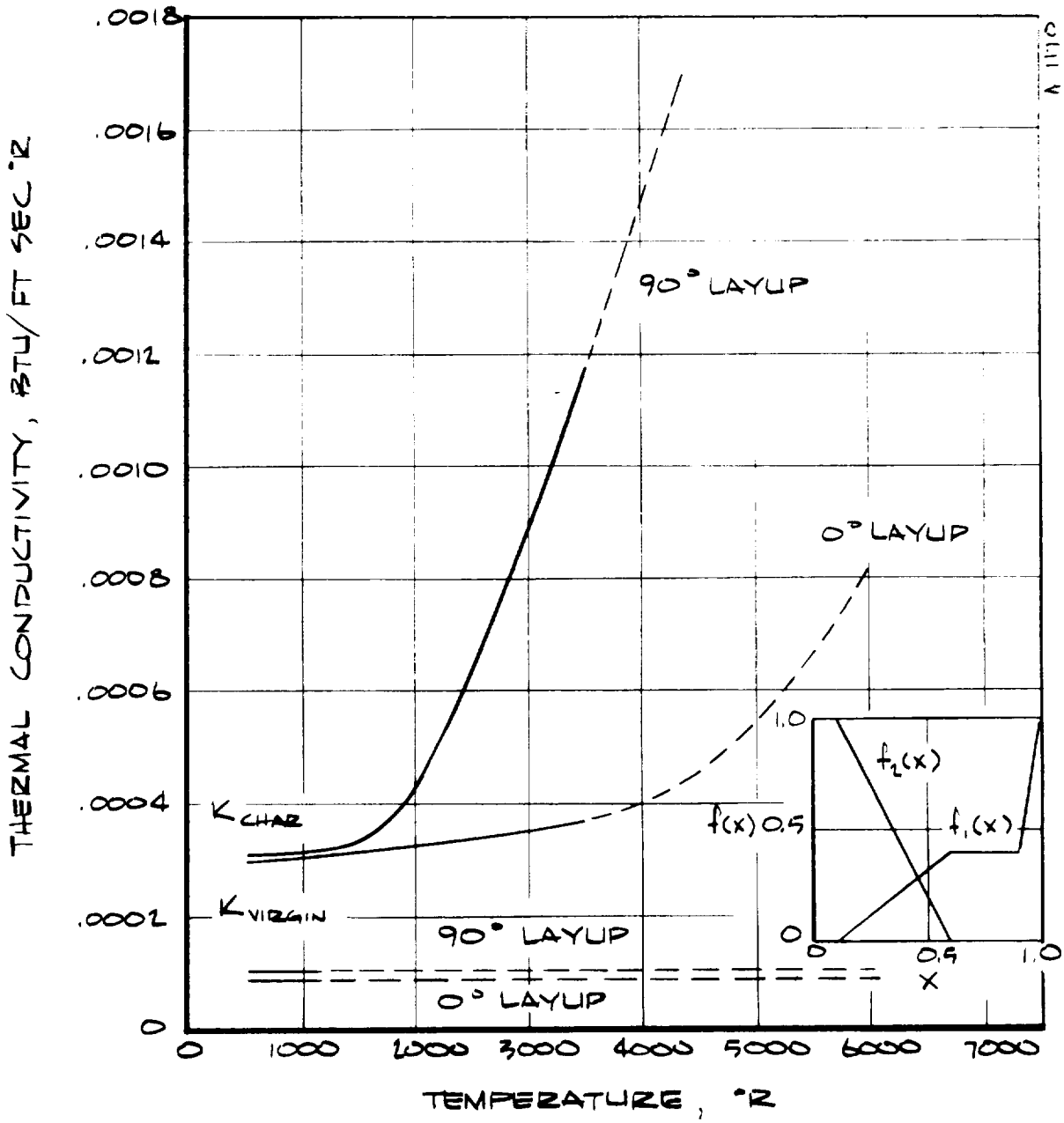

FIGURE 3-10 THERMAL CONDUCTIVITY FOR MXS-113 SILICA PHENOLIC

Table 3-6 Thermal and Physical Properties of MX2600, MX2600-96, and MXS-113 Silica Phenolics.

Material	Nominal Density (lb/ft^3)	Nominal Resin Mass Fraction	Resin Residual	Resin Elemental Formula (Phenolic)	Reinforcement Elemental Formula	Fail Temperature (^oR)	Virgin Material: Temperature (^oR)	Virgin Material: Specific Heat ($Btu/lb\ ^oR$)	Virgin Material: Thermal Conductivity $\times 10^4$ ($Btu/ft\ sec\ ^oR$) 0° Layup	Virgin Material: Thermal Conductivity $\times 10^4$ ($Btu/ft\ sec\ ^oR$) 90° Layup	Virgin Material: Emissivity	Char: Specific Heat ($Btu/lb\ ^oR$)	Char: Thermal Conductivity $\times 10^4$ ($Btu/ft\ sec\ ^oR$) 0° Layup	Char: Thermal Conductivity $\times 10^4$ ($Btu/ft\ sec\ ^oR$) 90° Layup	Char: Emissivity	Virgin Material Mass Fraction	Thermal Conductivity Weighting Function: Virgin Material	Thermal Conductivity Weighting Function: Char
MX2600 Silica Phenolic	108.7	0.315	0.50	C_6H_6O	SiO_2	3600	530	.260	.940	1.07	0.85	0.210	2.94	3.20	0.85	1.0	1.0	0.0
							800	.275	.943	1.09		--	--	--		0.8	0.5	0.0
							1000	--	--	--		0.430	3.06	3.32		0.55	0.5	0.0
							1160	.310	.944	1.10		--	--	--		0.25	0.0	1.0
							1500	.472	|	|	|	0.472	3.20	3.48	|	0.0	0.0	1.0
							2000	.484	|	|	|	0.484	3.31	3.60	|			
							3000	.493	|	|	|	0.493	3.57	3.88	|			
							3500	--	|	|	|	0.495	3.68	4.00	|			
							4000	.498	|	|	|	0.498	3.96	4.30	|			
							5000	.500	|	|	|	0.500	5.45	5.92	|			
MX2600-96 Silica Phenolic	108.7	0.315	0.50	C_6H_6O	SiO_2	3600	530	.260	0.940	1.07	0.85	0.210	2.50	3.20	0.85	1.0	1.0	0.0
							800	.275	0.943	1.09		--	--	--		0.9	0.4	0.0
							1000	--	--	--		0.430	2.52	3.32		0.6	0.4	0.0
							1160	.310	0.944	1.10		--	--	--		0.35	0.0	1.0
							1500	.472	|	|	|	0.472	2.54	3.48	|	0.0	0.0	1.0
							2000	.484	|	|	|	0.484	2.56	3.60	|			
							3000	.493	|	|	|	0.493	2.60	3.88	|			
							3500	--	|	|	|	0.495	2.64	4.00	|			
							4000	.493	|	|	|	0.498	2.72	4.30	|			
							5000	.500	|	|	|	0.500	3.00	5.92	|			
MXS-113 Silica Phenolic	95.6	0.590	0.50	C_6H_6O	SiO_2	3600	530	.260	0.850	1.00	0.85	0.210	2.94	3.11	0.85	1.0	1.0	0.0
							800	.275	|	|	|	--	--	--	|	0.9	0.4	0.0
							1000	--	|	|	|	0.430	3.06	3.15	|	0.6	0.4	0.0
							1160	.310	|	|	|	--	--	--	|	0.1	0.0	1.0
							1500	.472	|	|	|	0.472	3.10	3.30	|	0.0	0.0	1.0
							2000	.484	|	|	|	0.484	3.31	4.15	|			
							3000	.493	|	|	|	0.493	3.57	8.90	|			
							3500	--	|	|	|	0.495	3.68	11.70	|			
							4000	.498	|	|	|	0.498	3.96	14.70	|			
							5000	.500	|	|	|	0.500	5.45	21.25	|			

a) The decomposition kinetic constants for phenolic resin are tabulated below. The residual densities tabulated for

Reaction	Initial Density (lb/ft^3)	Residual Density (lb/ft^3)	Pre-exponential Factor (sec^{-1})	Activation Energy Factor (^oR)	Density Factor Exponent
A	20.25	0	1.40×10^4	15,400	3
B	60.75	{32.40 / 40.50}	4.48×10^9	36,800	3

reaction B corresponds to a resin residual of 0.40 and 0.50, respectively.

b) The following equation is suggested for layup angles other than 0^o and 90^o

$$k_\theta = k_{0^o}\left[1 + \left(\frac{k_{90^o}}{k_{0^o}} - 1\right)\sin\theta\right]$$

where θ is the layup angle referenced to a tangent to the surface.

c) The conductivity is given by

$$k = f_1(x)\ k_p(T) + f_2(x)\ k_c(T)$$

where x is the virgin material mass fraction, $f_1(x)$ and $f_2(x)$ are the virgin material and char weighting functions, respectively, and k_p and k_c are the virgin material and char conductivities, respectively.

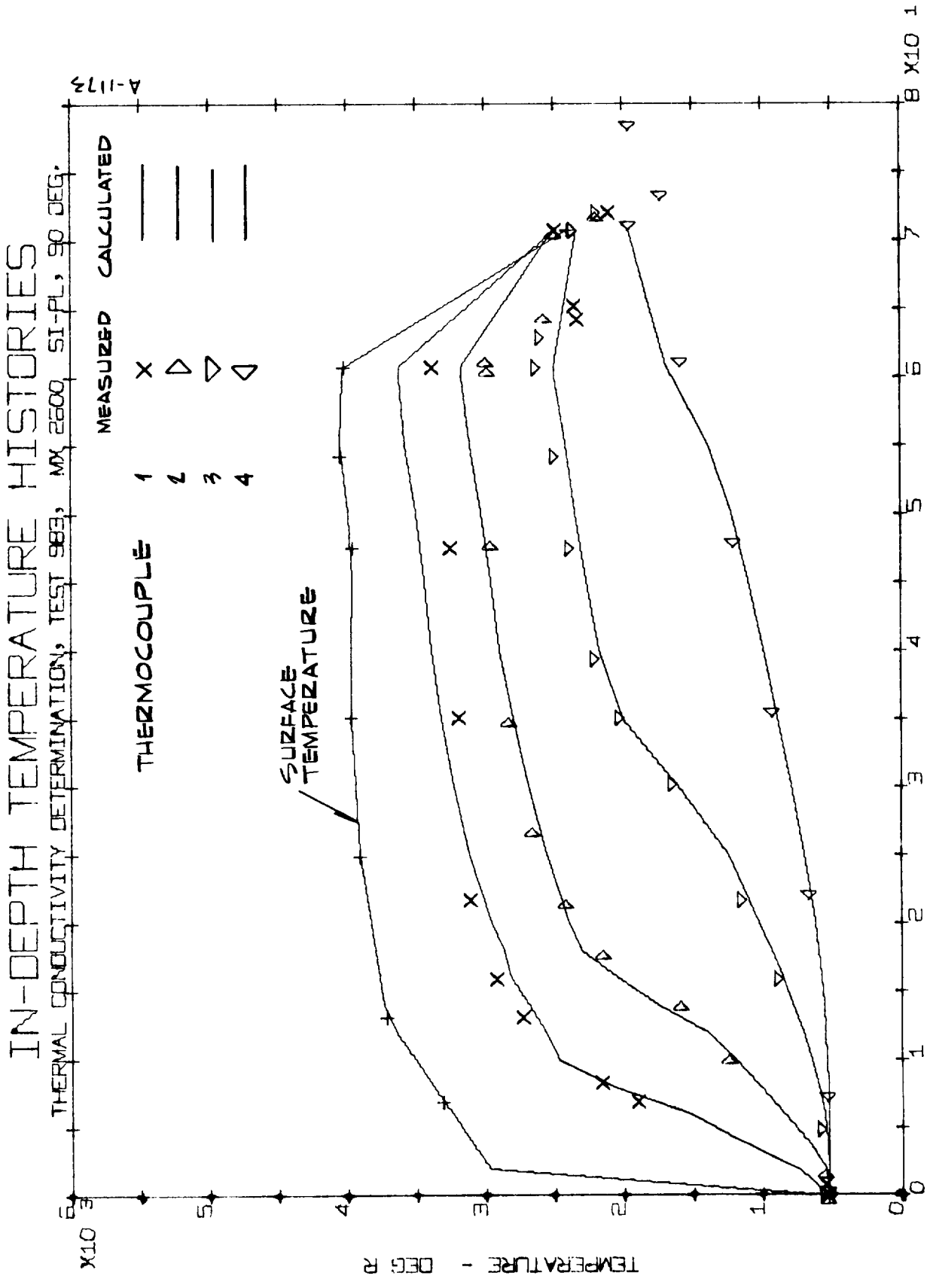

a) 90° LAYUP ANGLE

FIGURE 3-11 COMPARISON OF MEASURED AND CALCULATED IN-DEPTH TEMPERATURE HISTORIES FOR MX2600 SILICA PHENOLIC

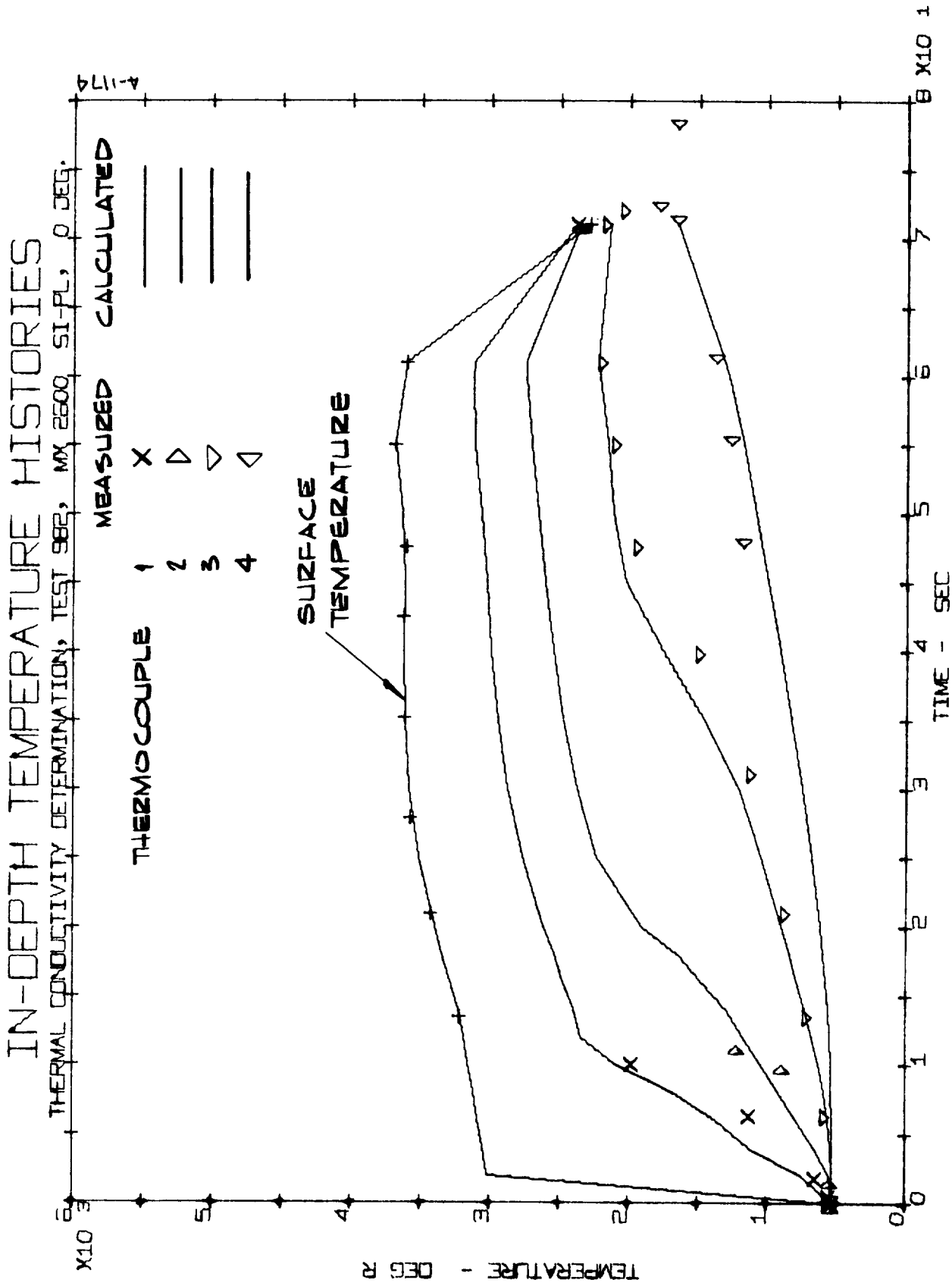

FIGURE 3-11 CONCLUDED

b) 0° LAYUP ANGLE

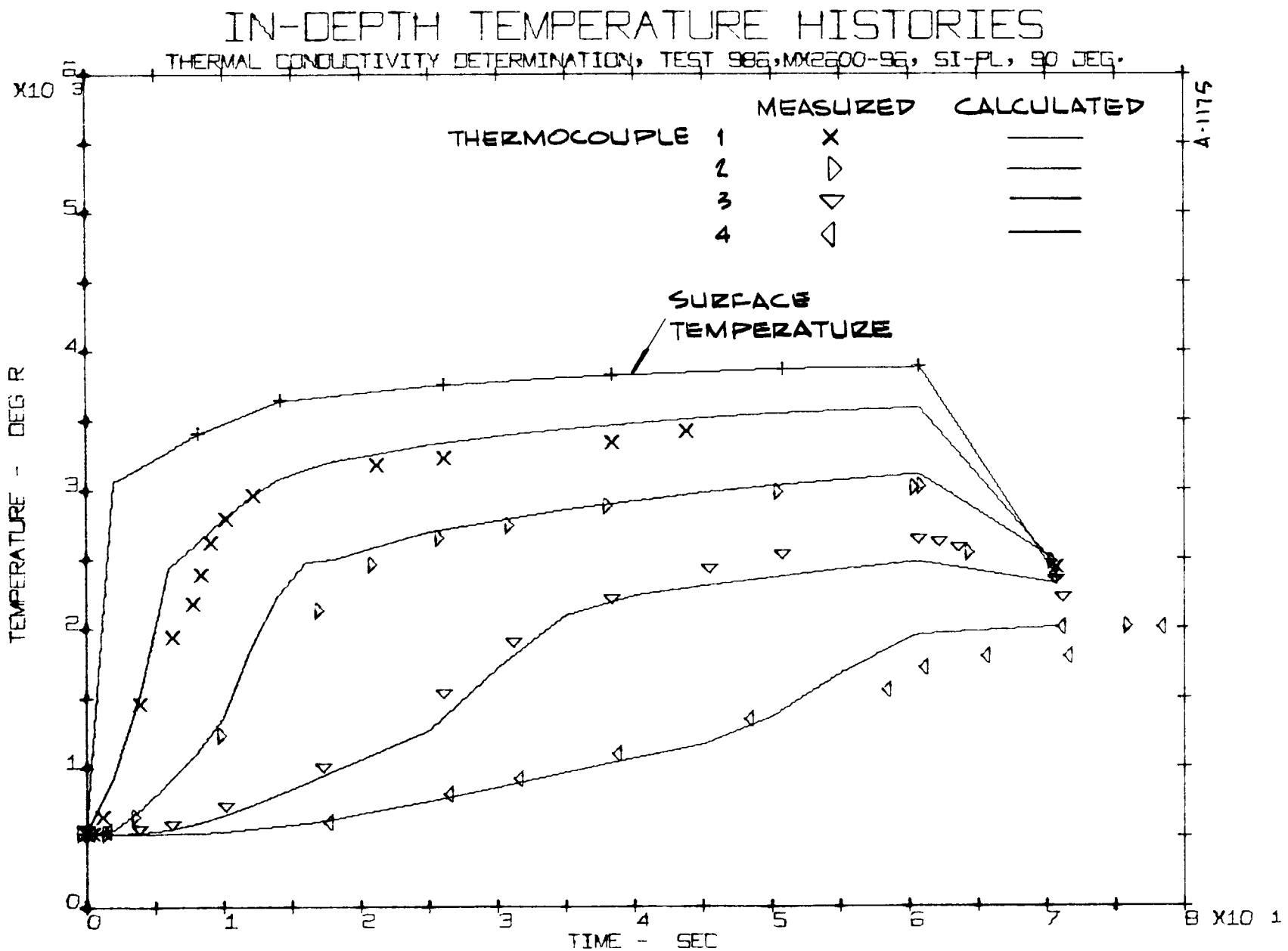

a) 90° LAYUP ANGLE

FIGURE 3-12 COMPARISON OF MEASURED AND CALCULATED IN-DEPTH TEMPERATURE HISTORIES FOR MX2600-96 SILICA PHENOLIC

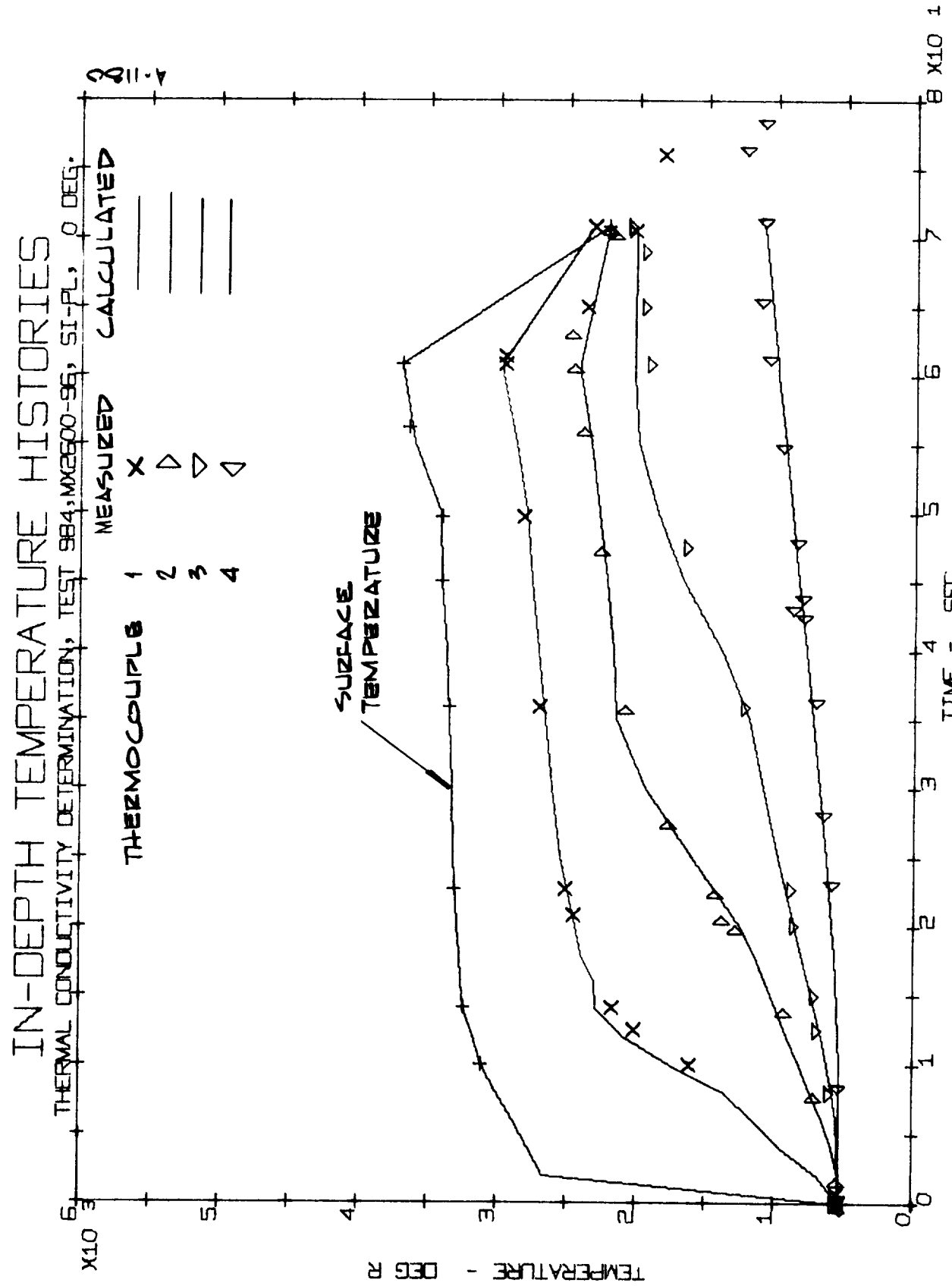

b) 0° LAYUP ANGLE

FIGURE 3-12 CONCLUDED

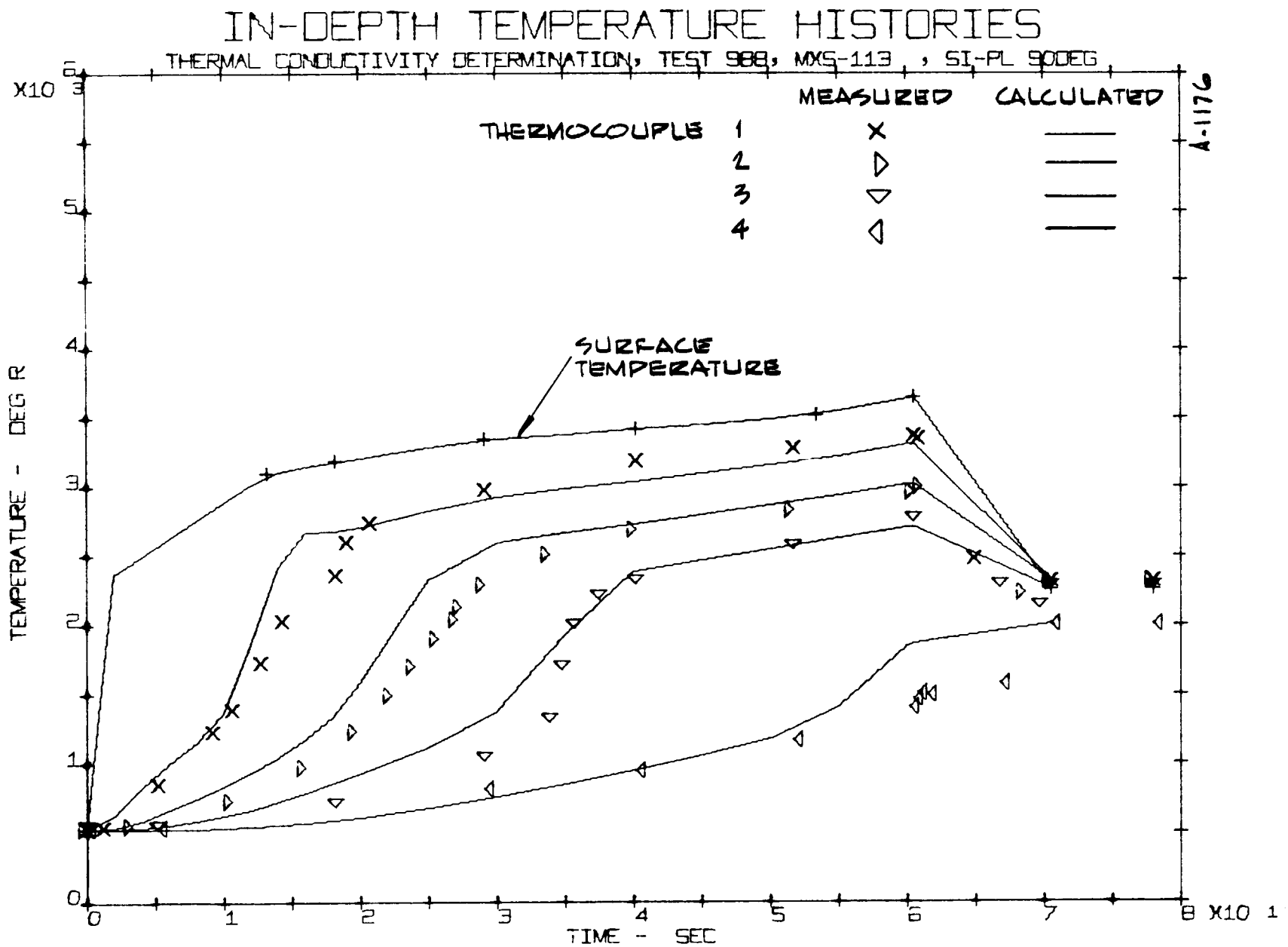

a) 90° LAYUP ANGLE

FIGURE 3-13 COMPARISON OF MEASURED AND CALCULATED IN-DEPTH TEMPERATURE HISTORIES FOR MXS-113 SILICA PHENOLIC

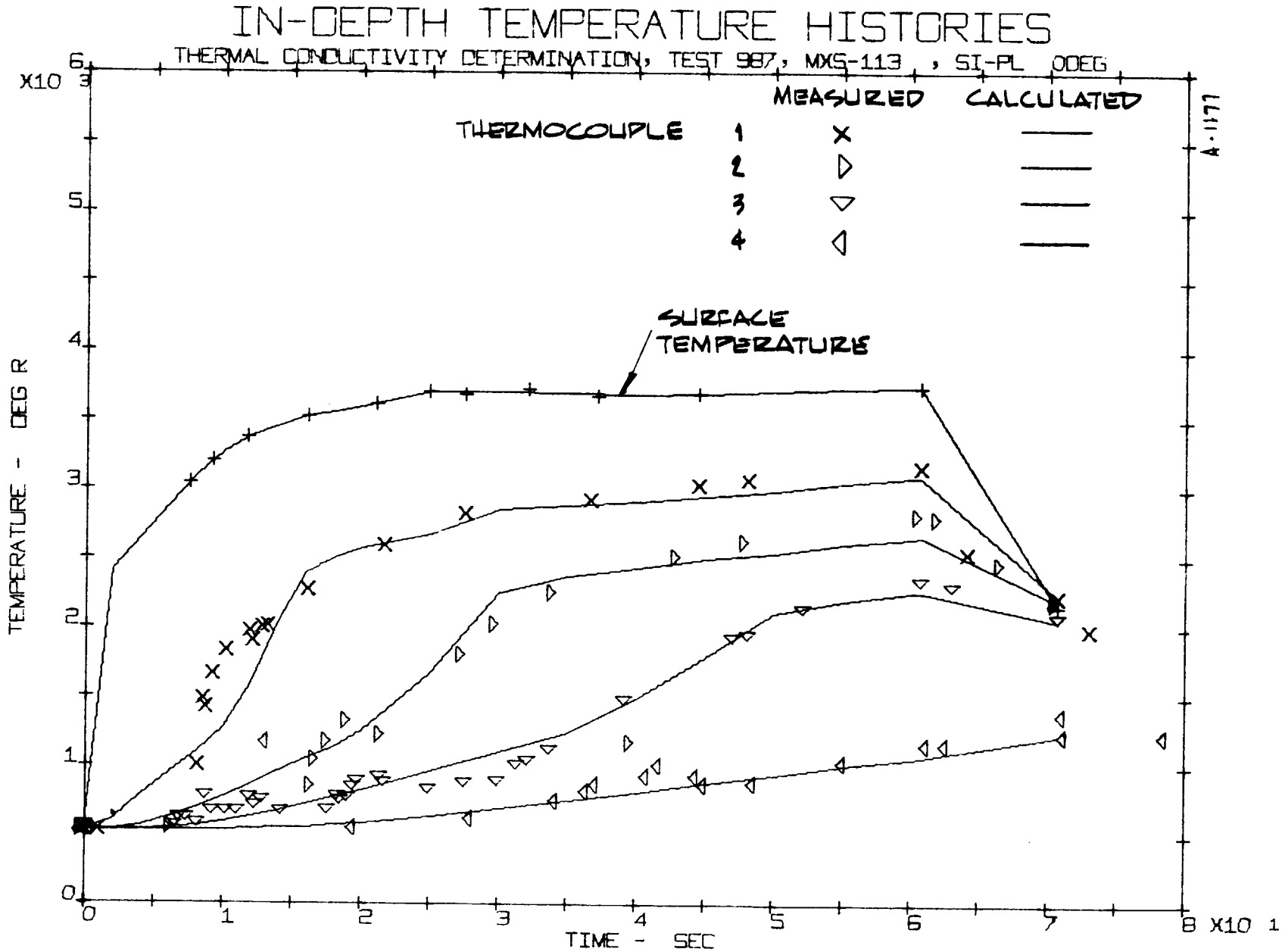

b) 0° LAYUP ANGLE

FIGURE 3-13 CONCLUDED

herein. This material is essentially identical to MX2600, the only difference being the manufacturer of the phenolic resin. The conductivity for these two materials is compared in Figure 3-14. The conductivity obtained herein is somewhat lower than that of Reference 2-6, although based on the similarity of materials no such difference should be expected. In the tests of Reference 2-6, surface recession occurred and the temperature was measured at three locations in depth instead of four. Also, the MXS-89 test nozzle was compression die molded whereas the MX2600 test models were obtained from a tape-wrapped part. On this basis, it is felt that the results of this program are more representative of large nozzle parts of MX2600 or MXS-89 silica phenolics.

A thermal conductivity test was also performed at a 20° layup angle for MX2600-96 silica phenolic (Table 3-5). This test was performed as a check on the method for accounting for layup angle on conductivity. From Reference 2-2, the conductivity for a given layup angle may be determined from

$$k = k_{0^\circ}\left[1 + \left(\frac{k_{90^\circ}}{k_{0^\circ}} - 1\right)\sin\theta\right] \qquad (3\text{-}2)$$

where θ is the layup angle referenced to a tangent to the surface. Using the conductivity data of Figure 3-9 and Equation (3-2), the internal temperature histories were calculated for the 20° layup angle model test and compared with measurement. This comparison is presented in Figure 3-15. The agreement is quite favorable, thus supporting the validity of Equation (3-2) and the basic conductivity results as well.

3.3.2 Performance Mechanisms

The performance mechanisms of silica phenolic materials were studied through arc plasma generator test firings at conditions typical of a large solid booster exit cone. Particular emphasis was placed on the surface response including liquid layer runoff, surface chemical reactions, and near surface condensed phase reactions. The materials for which tests were performed were:

MX2600 Silica Phenolic
MX2600-96 Silica Phenolic
MXS-113 Silica Phenolic

A 20° layup angle referenced to the surface, was used in all tests to simulate the exit cone application. Before presenting the test results some background comments are appropriate. The primary surface removal mechanisms for silica phenolic are liquid layer runoff and surface chemical reactions. The ACE

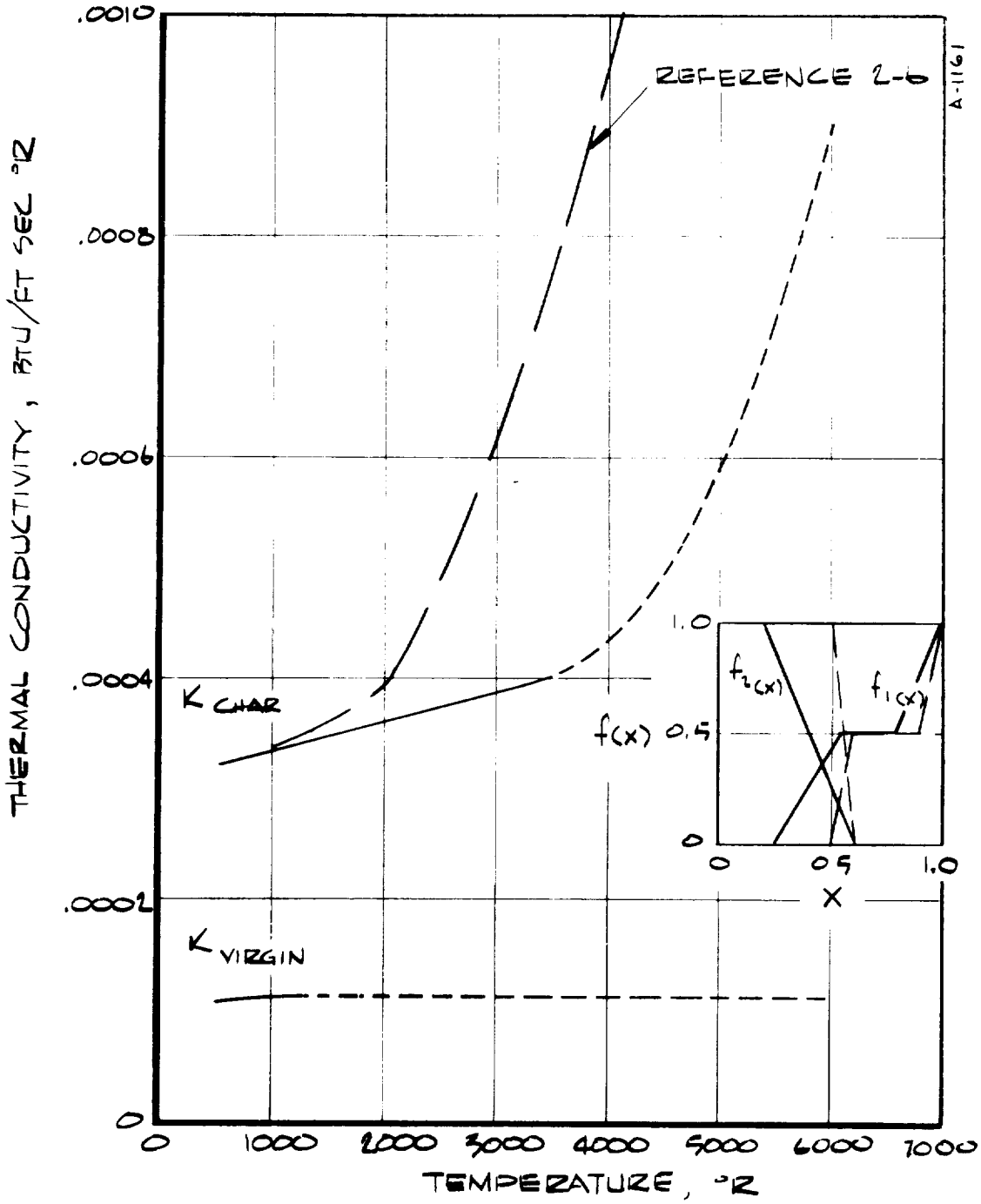

FIGURE 3-14 COMPARISON OF THERMAL CONDUCTIVITY FOR MX2600 SILICA PHENOLIC (FIGURE 3-8) AND MXS-89 SILICA PHENOLIC (REFERENCE 2-6), 90° LAYUP ANGLE.

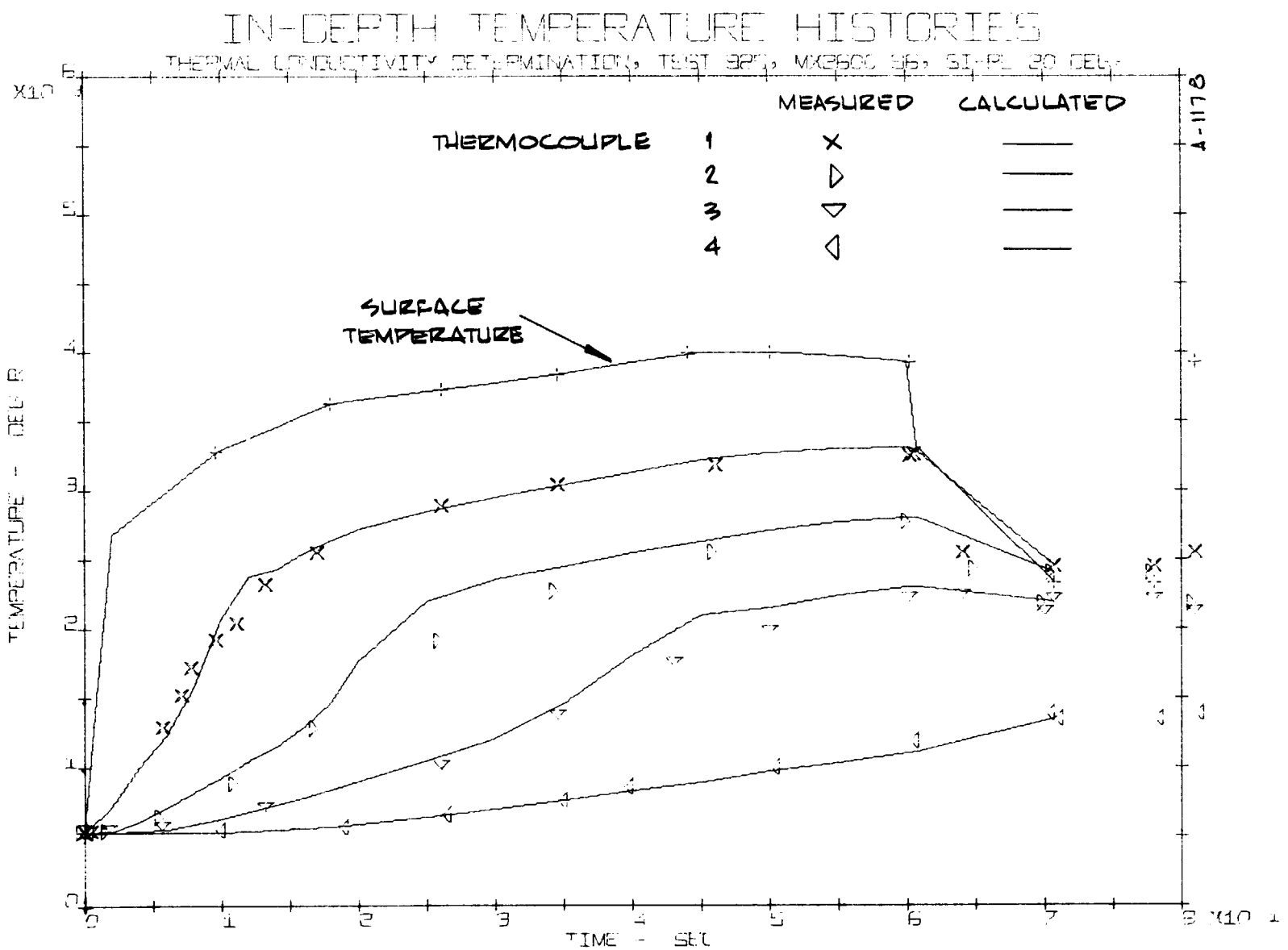

FIGURE 3-15 COMPARISON OF MEASURED AND PREDICTED IN-DEPTH TEMPERATURE HISTORIES FOR MX-2600-96 SILICA PHENOLIC AT 20° LAYUP ANGLE USING THE THERMAL CONDUCTIVITY FOR 0° AND 90° LAYUP ANGLES.

computer program models both of these removal mechanisms: liquid layer runoff through the use of a "fail" temperature above which runoff will occur and surface chemical reactions through the constraints of chemical equilibrium. Liquid layer runoff occurs once the surface temperature becomes high enough for the silica surface "melt" to flow under the action of wall shear. Silica however does not exhibit a discrete melt temperature but rather becomes less viscous with increasing temperature; therefore, the definition of a "fail" temperature for silica is not straightforward. This temperature was therefore defined approximately under this program for typical exit cone conditions.

The surface removal may also be affected by near-surface condensed phase chemical reactions. Two of the most likely reactions are

$$SiO_2^* + C^* \rightarrow SiC^* + O_2$$

$$SiO_2^* + C^* \rightarrow SiO + CO$$

where the asterisk indicates condensed phase. There are a number of other possible reactions but the net result is the same - a loss of material by partial or complete conversion to gas phase. The char density therefore decreases and the char may then become susceptible to mechanical failure. It should be noted that the above reactions are in-depth reactions; at the surface in an oxidizing environment the reverse reaction, e.g.,

$$SiO + \frac{1}{2} O_2 \rightarrow SiO_2^*$$

can occur and thus the silica is reformed at the surface. In the program herein, the results were briefly analyzed in the light of these possible reactions.

The test results under the performance mechanisms study are summarized in Table 3-5. Qualitative results were also available from the motion pictures of the ablating surface and through visual inspection of the fired models. The motion pictures present a very graphic description of the surface response and are available at Aerotherm, NASA Lewis Solid Rocket Technology Branch, and NASA Headquarters Solid Propulsion Experimental Engineering Branch. Pre-fire and post-fire photographs of three representative models are shown in Figure 3-16. The test results are discussed below.

In the calibration tests prior to the start of the material tests, valid heat flux data were obtained only at the 50 psia chamber pressure conditions. A check calibration of the heat flux calorimeter after completion of this test series revealed an erratic calibration shift at high heat flux. The heat flux for the 100 psia conditions presented in Table 3-5 was therefore calculated from the measurements at the 50 psia conditions. These calibration tests

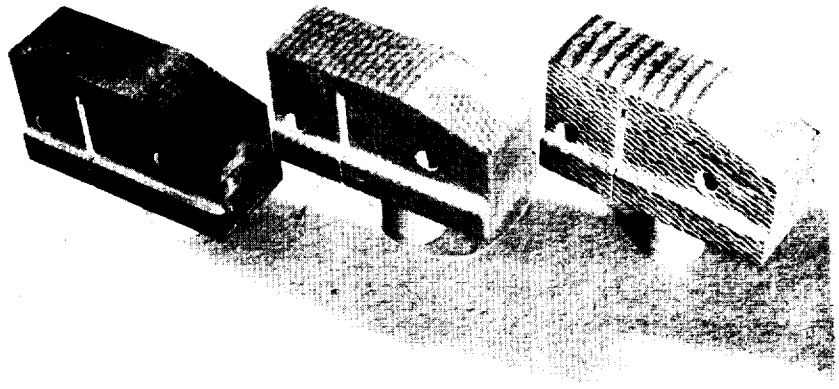

MXS-113 MX2600 MX2600-96

a) Pre-Fire

MXS-113 MX2600 MX2600-96

b) Post-Fire

Figure 3-16 Typical Silica Phenolic Test Models

also revealed that the measured heat flux and therefore the heat transfer coefficients and wall shears were significantly lower than anticipated. This is apparent from a comparison of Tables 3-4 and 3-5. The low measured fluxes are apparently associated with the 2D nozzle configuration. (The projected conditions of Table 3-4 were determined from axisymmetric nozzle test results which were related to the 2D nozzle through the hydraulic radius.) Tests verified that there were no unusual flow patterns or flow separation in the nozzle that might have caused the low measured heat fluxes. The explanation must await further analysis. The low (and even negative) recession noted in Table 3-5 is due primarily to the lower than expected heat and mass transfer coefficients and wall shear. The water-cooled wall opposite the model which was required for the surface motion picture photography also contributed to this low recession by providing a radiation sink for the ablating surface.

In the performance mechanisms tests of the silica phenolic materials, all materials exhibited liquid layer runoff (Figure 3-16) even though the net surface recession was negative for the MX2600 and MX2600-96 materials. The liquid flow as shown by the motion pictures is somewhat difficult to describe, both verbally and theoretically. The silica melt flows along the surface in an erratic fashion much like the flow of lava. The flow cannot be characterized simply by droplet or rivulet flow. The local surface temperature appears to vary significantly with time, the maximum temperature coinciding with a burst of melt issuing from the local region. There was no qualitative difference in the observed surface melt response of the three materials. It should be pointed out that the above observations apply to conditions of incipient or moderate melt removal and may not be representative of conditions for which the surface recession is high.

Note from Table 3-5 that the surface recession is actually negative for the MX2600 and MX2600-96 materials although a flowing melt was observed in the surface motion pictures and a weight loss occurred in all cases. Post-test inspection of the cross-sectioned models showed no evidence of char warping or swelling and therefore this mechanism does not provide an explanation for the observed performance. The negative recession is therefore apparently associated with the formation of the surface melt; the melt forms on top of the char surface and apparently has a lower density, and therefore occupies a larger volume than in the parent material. Another potential explanation is the formation of melt through the reaction

$$SiO + \frac{1}{2} O_2 \rightarrow SiO_2^*$$

where the SiO gas is available from silica decomposition or condensed phase reactions in depth and the O_2 is available from the free stream. However,

the quantitatively similar performance for the inert test gas (Mixture 5) in which there is no oxygen apparently precludes this mechanism as being important in the firings performed herein.

For the MXS-113 material, the surface recession was significant. Since in the inert environment at 0° and 90° layup angle the surface recession was small, the observed recession in the oxidizing environment (Mixture 4) is probably due to oxidation of the char through the reaction

$$C^* + \frac{1}{2} O_2 \rightarrow CO$$

where the C* is the carbon residue of resin pyrolysis. This mechanism can be important in this material, as opposed to the other materials, since the resin percent is 59 by mass, almost twice that of the other materials.

Predictions of the response of MX2600-96 at the conditions corresponding to the Model 19 test (Table 3-5) were performed using the ACE and CMA computer programs. The fail temperature chosen to characterize melt removal was first taken as 3390°R, the value from Reference 2-7. The predicted surface recession was 0.080 inch compared to the measured recession of -0.007 inch. The predominent surface recession mechanism was melt removal and therefore it was apparent that the actual fail temperature was higher than the assumed 3390°R. A prediction was therefore made for a fail temperature of 3600°R, this being the approximate maximum surface temperature measured which hopefully corresponded to a burst of melt issuing from the surface as noted in the motion pictures. These results are presented and compared with the measured performance in Figures 3-17 and 3-18. The predicted surface recession is still positive but low, 0.005 inch. A higher fail temperature cannot be justified since it would result in a predicted surface temperature higher than that measured. This discrepancy between measurement and prediction must therefore be due to a phenomenon not accounted for in the prediction, probably the density decrease effect postulated above. This effect would be expected to be small relatively speaking where the melt removal (and therefore surface recession) is high. Based on the above results, 3600°R appears to be a reasonable value for the fail temperature of silica in MX2600-96 silica phenolic and is probably applicable to other high density silica phenolic materials as well.

The qualitative in-depth performance of the MXS-113 material, based on observation of the cross-sectioned test models, was characterized by small delaminations in the heat-affected region and a structurally weak char - pyrolysis zone boundary. The char could be broken away from the model quite easily. No failure or gross char loss occurred during any of the test firings of the MXS-113 models, however. No such delaminations or char weakness was observed for the MX2600 or MX2600-96 materials.

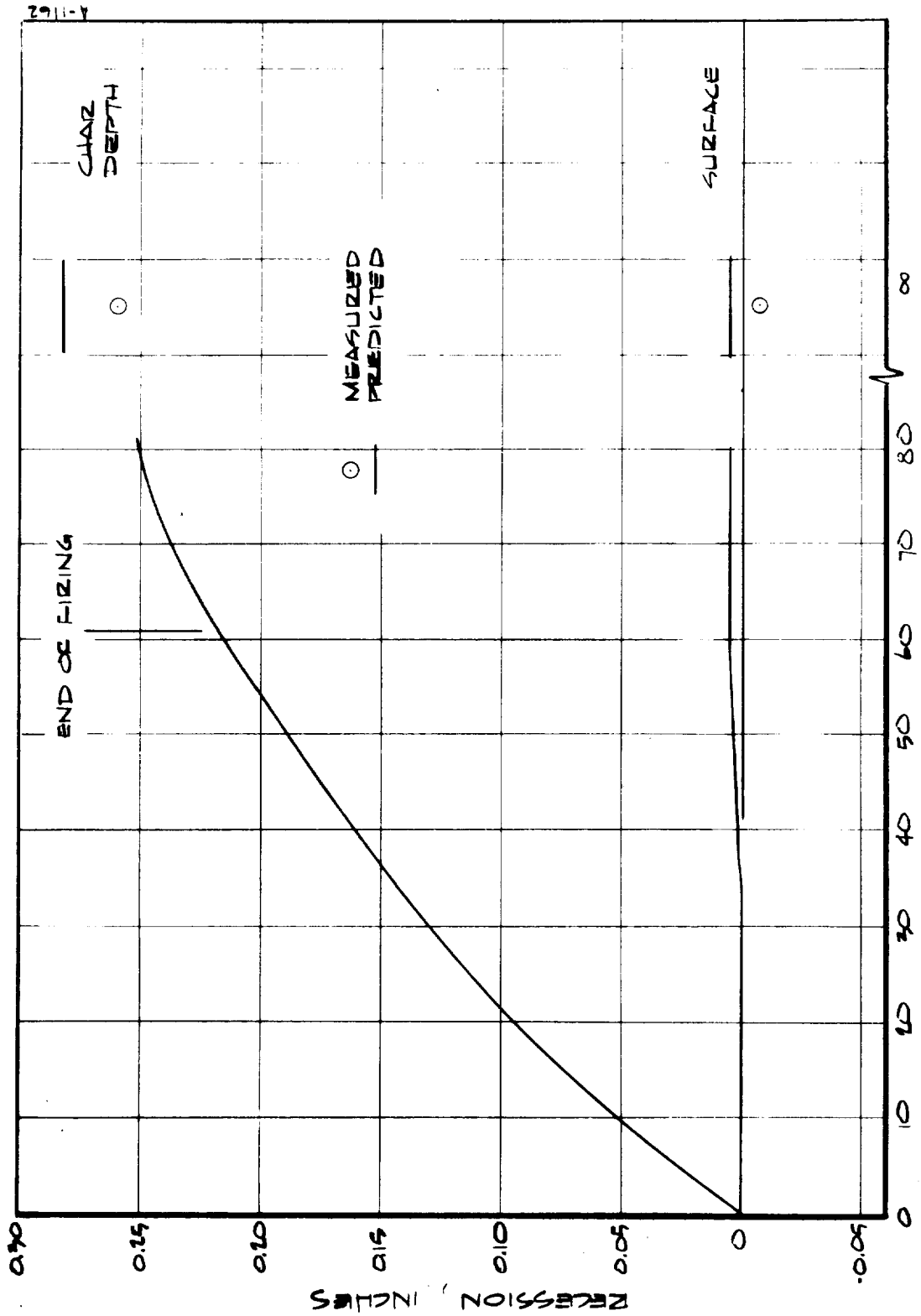

FIGURE 3-17 COMPARISON OF MEASURED AND PREDICTED SURFACE RECESSION AND CHAR DEPTH FOR MX 2600-96 SILICA PHENOLIC; 20° LAYUP ANGLE, MIXTURE 4, 3600°R FAIL TEMPERATURE.

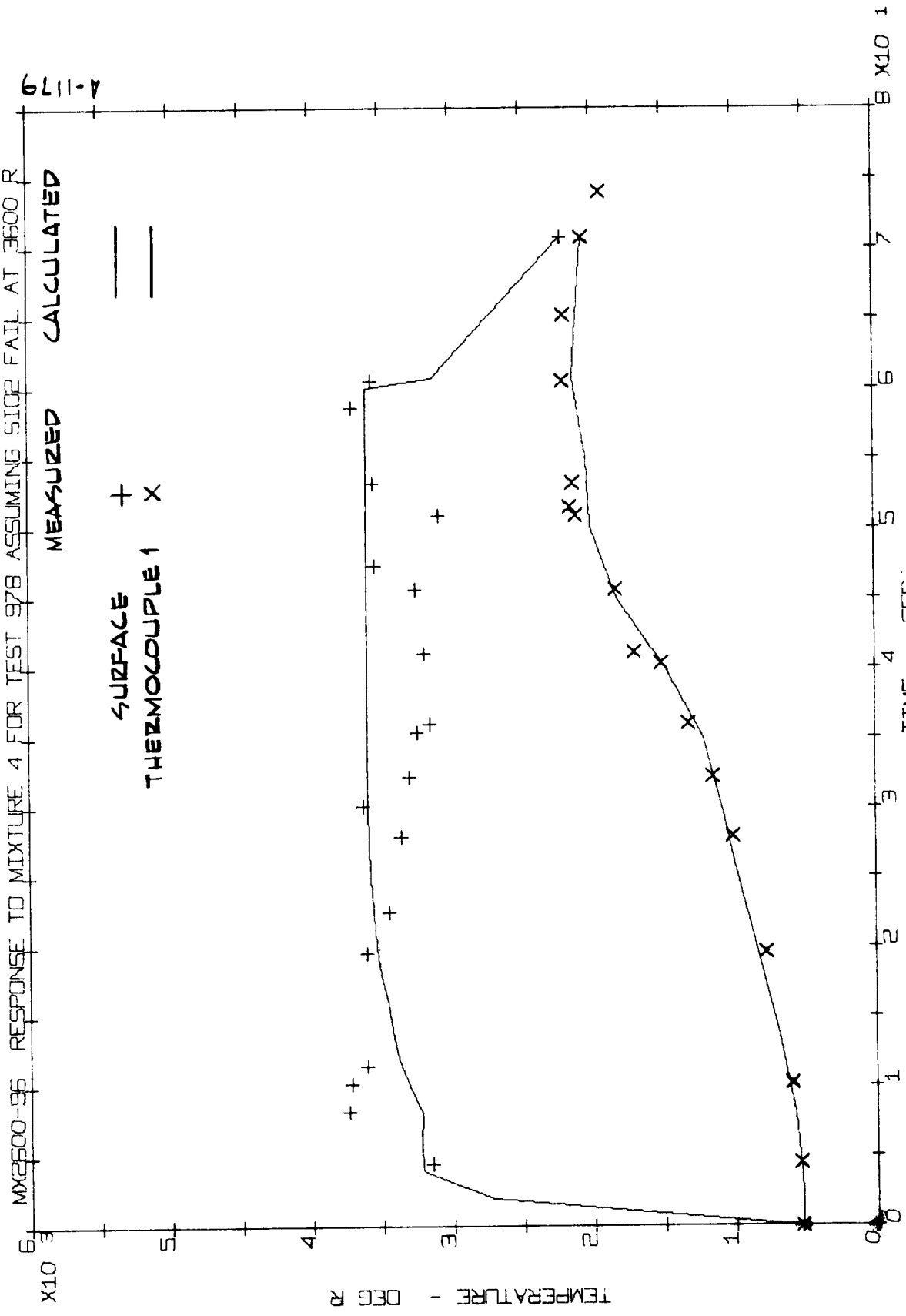

FIGURE 3-18 COMPARISON OF MEASURED AND PREDICTED SURFACE AND IN-DEPTH TEMPERATURE HISTORIES FOR MX 2600-96 SILICA PHENOLIC; 20° LAYUP ANGLE, MIXTURE 4, 3600°R FAIL TEMPERATURE.

The test models were also examined for evidence of any in-depth condensed phase reactions. The existence of such reactions would be manifested primarily by a char density decrease through a depletion of both carbon and silica. Visual inspection exhibited no evidence of in-depth chemical reactions; chemical and physical properties tests to verify this conclusion were beyond the scope of the contract.

The MX2600-96 and MXS-113 materials are low cost materials, the former by virtue of its double thick tape and the resultant decrease in wrapping time to fabricate a part and the latter by virtue of its random fiber instead of cloth reinforcement. The MX2600-96 material exhibited a performance which was qualitatively and quantitatively similar to that of MX2600. Therefore, there appears to be no performance disadvantage associated with the cost-saving advantage of MX2600-96. The MXS-113 material exhibited inferior performance to that of MX2600 although its performance appeared adequate. Therefore this material also appears attractive from a cost/performance standpoint at least for some applications.

REFERENCES - SECTION 3

3-1 Warga, J., Davis, H., DeAcetis, J., and Lampman, J.: Evaluation of Low-Cost Materials and Manufacturing Processes for Large Solid Rocket Nozzles. AFRPL-TR-67-310, Aerojet-General Corp., December 1967.

3-2 Kratsch, K. M., Hearne, L. F., and McChesney, H. R.: Thermal Performance of Heat-Shield Composites During Planetary Entry. Presented at the AIAA-NASA National Meeting, Palo Alto, California, Sept. 30 - Oct. 1, 1963.

3-3 Clark, K.: Thermal Conductivity Model for Avcoat 5026-39, Technical Memorandum 6007-TM-2R, Aerotherm Corporation, February 1, 1967.

SECTION 4

EVALUATION OF HEAT AND MASS TRANSFER COEFFICIENTS

The values of heat and mass transfer coefficient input to the Charring Material Ablation (CMA) Computer Program are critical to the successful prediction of material response. The transfer coefficient calculational approach used in previous studies (e.g., References 2-2, 4-1, and 4-2) and in Section 2 herein has resulted in accurate predictions of material response. In this approach, the transport properties required in these calculations were estimated. Recent calculations indicated that these estimates were not accurate, and therefore the calculated heat and mass transfer coefficients were inaccurate or were correct only because of some other compensating inaccuracy. A study was therefore initiated to define parametrically the effects of transfer coefficients and other input variables on the prediction of material performance. The results of this study are presented in Section 4.1. These results were then applied to the prediction of performance at the throat of the 260-SL-3 nozzle. The results of this study are presented in Section 4.2.

4.1 PARAMETRIC STUDY AND RESULTS

In order to conveniently determine the effects of boundary condition input variables on calculated surface response, the Charring Material Ablation (CMA) Computer Program was modified to give surface recession rates and surface temperatures for conditions corresponding to "steady state" ablation. The steady state treatment provides meaningful surface response results without a detailed calculation of in-depth response, the calculated results corresponding to infinite time in a transient calculation. For this case, the surface, char, and pyrolysis zone recession rates are equal and constant with time. In addition, the in-depth temperature distribution referenced to the instantaneous surface is invariant with time.

In the steady state CMA (SSCMA) program, surface recession rate and surface temperature are defined by mass and energy balances on the control volume in the sketch below. The control volume in the sketch extends from just above the surface into the virgin material, enclosing the char, pyrolysis zone, and temperature-affected virgin material. The surface recession rate and surface temperature is therefore defined by the consumption of virgin material only; the mass and energy balances need only consider the steady state consumption of virgin material. The necessary SSCMA input information is heat and mass transfer coefficients, wall emissivity, incident radiation energy, recovery enthalpy, and virgin material density and heat of formation. No material thermal properties are required as input.

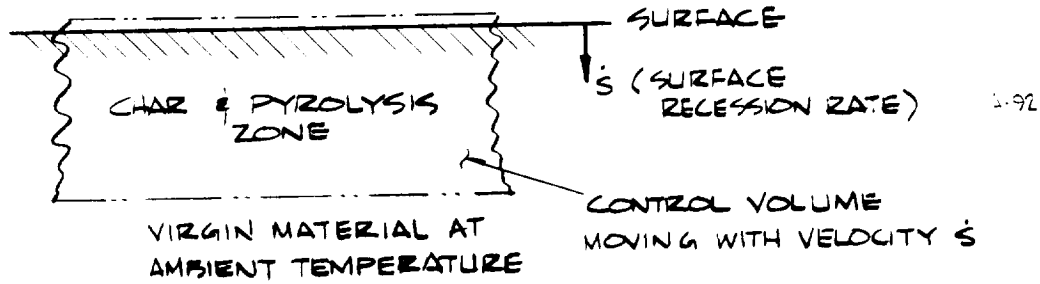

In order to determine the effects of the variation of each of these parameters, the SSCMA program was run several times varying one input parameter about a standard calculation point. The standard calculation point chosen for this parametric study corresponded to approximate throat conditions for 260-SL-3 nozzle and the MX4926 carbon phenolic material. These standard calculation input values were:

Nonablating wall heat transfer coefficient	=	0.34 lb/ft^2 sec
Ratio of mass to heat transfer coefficients	=	1.00
Wall emissivity	=	0.85
Stream emissivity	=	1.00
(Incident radiation energy	=	570 Btu/ft^2 sec)
Recovery factor	=	1.00
(Recovery enthalpy	=	706 Btu/lb)
Material density	=	89.4 lb/ft^3
Material heat of formation	=	-379.5 Btu/lb

For these input conditions, the calculated steady state surface recession rate and surface temperature were 7.7 mils/sec and 5,060°R, respectively.

The results of the parametric study are given in Figures 4-1 and 4-2. Note that ξ is the value of an input variable divided by its standard calculation value above. From Figure 4-1, the mass transfer coefficient has the greatest influence on surface recession rate. For example, an increase of $\rho_e u_e C_M$ from 1/2 to 2 times its standard calculation value produces an increase of surface recession rate from 4.6 to 12.3 mils/sec. The other parameters have a considerably less significant effect on recession rate.

From Figure 4-2, the mass transfer coefficient, stream emissivity, and wall emissivity have a significant influence on surface temperature. Increasing mass transfer coefficient and decreasing emissivities correspond to decreasing surface temperature. For example, a decrease in stream emissivity from 1.0 to 0 results in a decrease in surface temperature from 5060°F to 4090°R. The fact that lowering wall emissivity decreases surface temperature is apparently due to the reasonable assumption that surface emissivity and surface absorptivity are equal; hence, incident radiant energy is effectively decreased with decreasing wall emissivity.

The parametric study results are, of course, completely accurate only at infinite time. However, the steady state calculation is simply a limiting case of the transient calculations, so that the parametric study results may be applied qualitatively to most situations. For example, the steady state surface recession rate calculated for the end of the 260-SL-3 nozzle firing is within 15 percent of the transient value which is lower as expected.

4.2 APPLICATION TO THE 260-SL-3 NOZZLE THROAT

The parametric study results allowed the possible errors in input information to a material performance prediction to be directly related to surface recession. Such an error analysis was performed for the throat of the 260-SL-3 nozzle with primary emphasis on the effect of transport properties on the heat and mass transfer coefficients as presented below.

The transport properties which most significantly affect the calculated heat and mass transfer coefficients are Prandtl number and Lewis number* where the functional relationships are

$$\rho_e u_e C_H \propto \frac{1}{Pr^{2/3}}$$

$$\rho_e u_e C_M \propto \frac{1}{Sc^{2/3}} = \rho_e u_e C_H \left(\frac{Pr}{Sc}\right)^{2/3} = \rho_e u_e C_H Le^{2/3}$$

*The recovery factor is also a function of Prandtl number ($R = Pr^{1/3}$ for turbulent flow). However, the parametric study (Figures 4-1 and 4-2) shows that a variation of recovery factor has very little effect on recession rate so this is not discussed here.

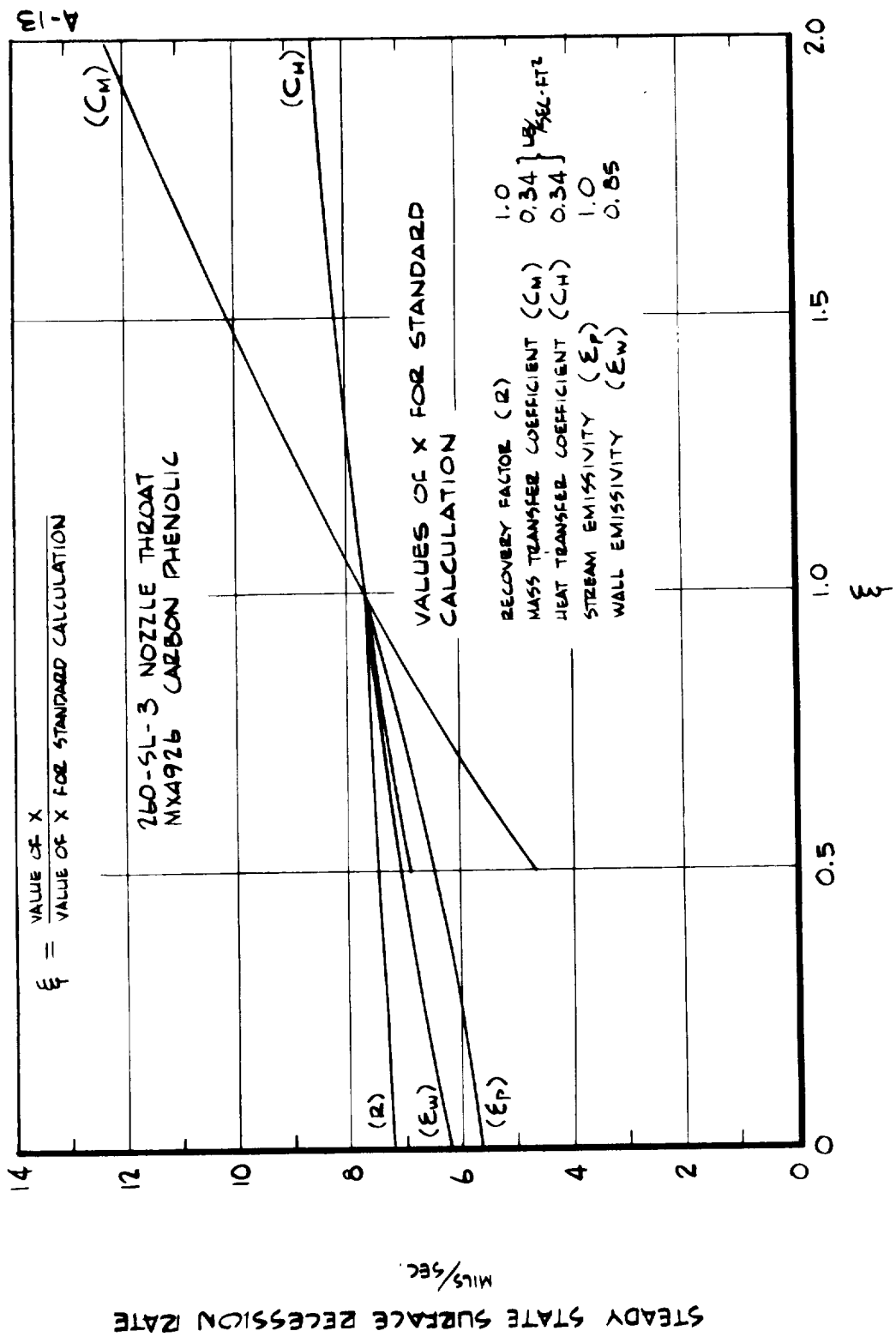

FIGURE 4-1 EFFECT OF VARIATION OF A SINGLE VARIABLE ON STEADY STATE SURFACE RECESSION RATE.

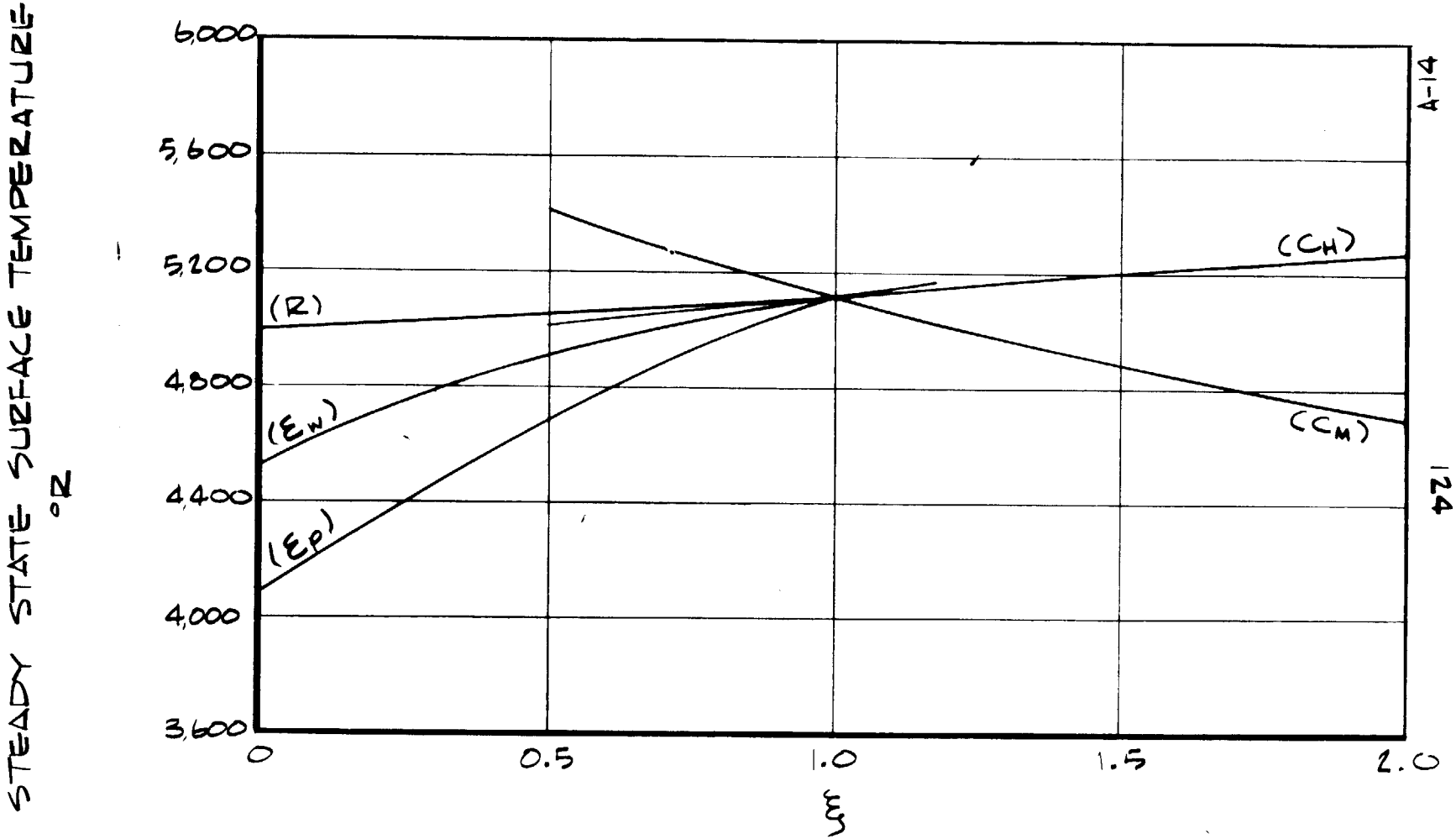

FIGURE 4-2 EFFECT OF VARIATION OF A SINGLE VARIABLE ON STEADY STATE SURFACE TEMPERATURE.

The Prandtl and Lewis numbers (and other transport properties) were calculated using the Aerotherm Chemical Equilibrium (ACE) Computer Program and were compared with the estimates used in the predictions of Section 2. In Figure 4-3, the calculated Prandtl and Lewis numbers for the ANB-3254 propellant are shown as functions of temperature for various pressures. The broad range of conditions considered included those of the 260-SL-3 nozzle. Typical values in Figure 4-3 are Prandtl number = 0.38 and Lewis number = 0.56; previous calculations of transfer coefficients have assumed Prandtl number = 1.0 and Lewis number = 0.93.

The discrepancy between actual and assumed values is large and the effect on the heat and mass transfer coefficients and surface response is therefore significant. The table below summarizes how the improved Prandtl and Lewis numbers affect the calculated surface recession rates; the calculated ablation rate is higher by 30 percent. The standard calculations, however, have been

	Pr	Le	$\rho_e u_e C_H$	$\rho_e u_e C_M$	ε_p	ξ_{CH}	ξ_{CM}	$\xi_{\varepsilon p}$	$\dot{s}$
			(lb/ft^2 sec)						(mils/sec)
Values for standard calculations	1	1	0.34	0.34	1.0	1.0	1.0	1.0	7.7
Values with new ACE data	0.38	0.56	0.65	0.44	1.0	1.9	1.3	1.0	10

shown to yield accurate predictions; 7.7 mils/sec is the recession that can be expected to occur in the real situation. Apparently, then, errors associated with the heat transfer coefficient calculation technique or with other inputs must have balanced the errors in transfer coefficients due to Prandtl and Lewis number inaccuracies.

First consider the possibility that the basic technique for calculating heat transfer coefficient (Reference 2-5) consistently overpredicts the coefficient by a constant value. In order to drop the recession rate value back to 7.7 mils/sec, this multiplier on heat transfer coefficient must be 0.75. The calculation parameters corresponding to this assumption are given in the table below. This requirement of decreasing the calculated heat transfer

	Pr	Le	$\rho_e u_e C_H$	$\rho_e u_e C_M$	ε_p	ξ_{CH}	ξ_{CM}	$\xi_{\varepsilon p}$	$\dot{s}$
			(lb/ft^2 sec)						(mils/sec)
Values for reduced heat transfer coefficient assumption	0.38	0.56	0.49	0.33	1.0	1.4	0.97	1.0	7.7

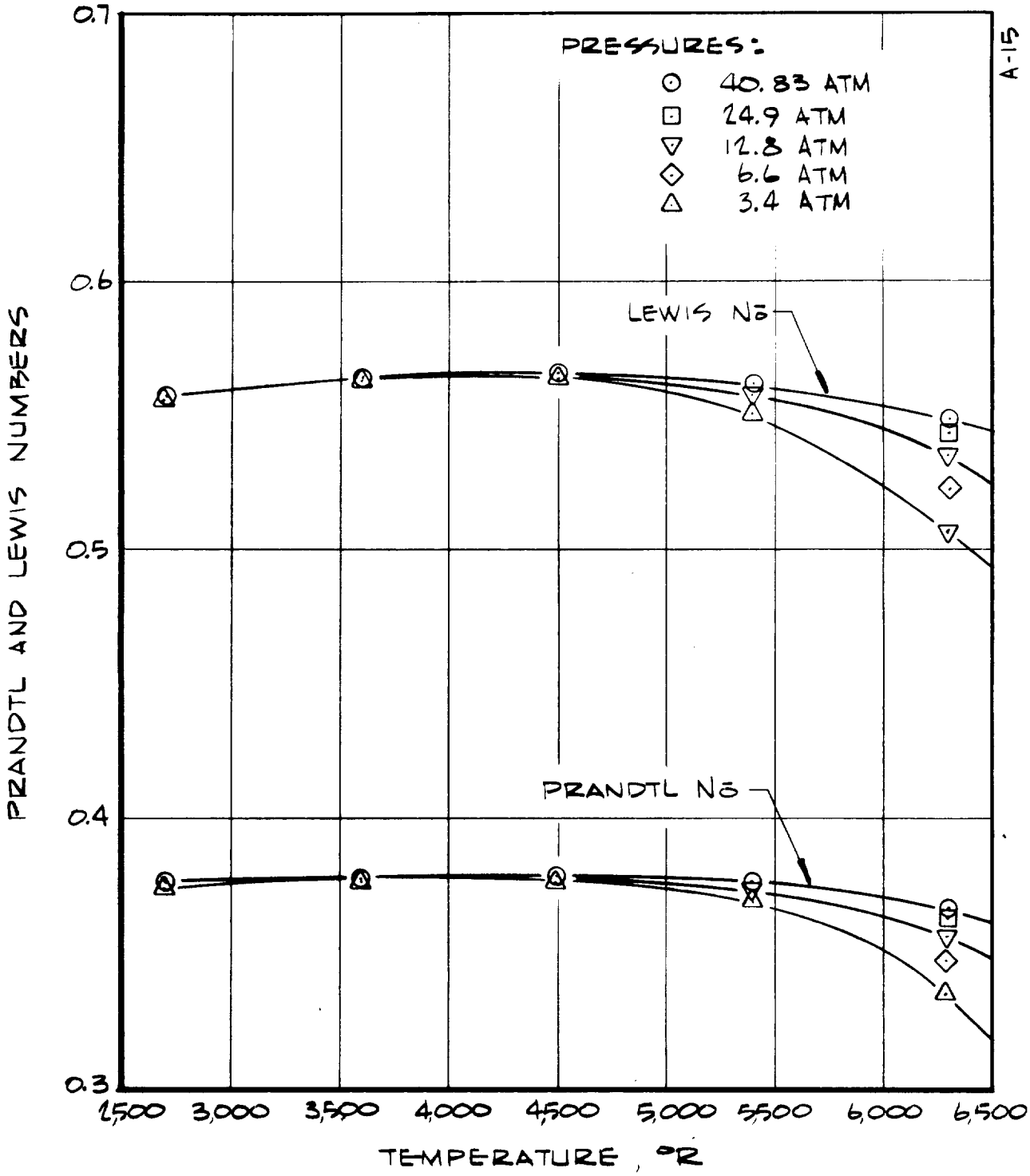

FIGURE 4-3 PRANDTL AND LEWIS NUMBERS VS TEMPERATURE, AEROJET ANB-3254 PROPELLANT

coefficient to achieve agreement with experiment has been observed in heat flux measurements made by Aerotherm in the program of Reference 2-6. The chemical environment was the combustion products of nitrogen tetroxide-50/50 hydrazine UDMH and the determined constant analogous to 0.75 above was 0.83. Based on these results it appears that the reduction of the calculated heat transfer coefficient and therefore mass transfer coefficient, is reasonable and may well be the explanation for past success using improper transport properties.

The other possibility is an error in other boundary condition input. For example, a decrease in the stream emissivity from the assumed value of 1.0 to a value of 0.25 will yield the desired surface recession as shown in the table below. The effective emissivity of particle-laden streams in a

	Pr	Le	$\rho_e u_e C_H$	$\rho_e u_e C_M$	ε_p	ξ_{CH}	ξ_{CM}	$\xi_{\varepsilon p}$	$\dot{s}$
			($lb/ft^2 sec$)						(mils/sec)
Values for $\varepsilon_p = 0.25$	0.38	0.56	0.65	0.44	0.25	1.9	1.3	0.25	7.7

rocket nozzle is certainly subject to some doubt and a value of 0.25 may not be unreasonable. Note that no other variable affords the leverage on the final answer that stream emissivity does (Figure 4-1); the effect of recovery factor is small and the wall emissivity is certainly at least close to 0.85.

On the basis of the above analysis, the technique used to calculate heat transfer coefficient (and therefore mass transfer coefficient) overpredicts its value or the particle-laden stream emissivity is considerably less than unity, or both. On the basis of past success in predicting material response over a wide range in firing conditions and for which the stream emissivity was assumed unity, overprediction of the heat transfer coefficient appears to be the more likely explanation.

Other possible mechanisms not considered herein may also provide an explanation for the apparently high predictions. One such possibility is condensed phases within the boundary layer which alter its character (their existance would at least alter the local scale of turbulence). From the direction of the required change of heat transfer coefficient (i.e., a reduction) it is suggested that the boundary layer velocity profile may be somewhere between those typical of laminar and turbulent boundary layers. Another possible mechanism is re-laminarization of the boundary layer in the vicinity of the throat. This mechanism is improbable because the applicable throat Reynolds numbers are at least an order of magnitude higher than the maximum where throat re-laminarization has been observed (e.g., Reference 4-3).

Another mechanisms for reduced material recession rates not considered in the above analysis is kinetically controlled reactions at the surface. Surface response under kinetically controlled conditions is typically very temperature sensitive, such that the discrepancy between measured and predicted surface recession would be strongly influenced by the material surface temperature, in apparent conflict with experience.

In any case, the existing evidence is certainly a nebulous base on which to make a firm conclusion. More detailed analyses are required to resolve wherein the cause for the discrepancy lies.

REFERENCES - SECTION 4

4-1 Schaefer, J. and Dahm, T., Analysis of Ablative Material Erosion for the Thiokol 156-2C-1 Motor Nozzle (U). Vidya Report No. 206, Vidya Div. of Itek Corp., November 15, 1965. CONFIDENTIAL

4-2 Dahm, T. and Schaefer, J., Analysis of Subscale Results and Final Prediction of Ablation Material Performance for Two Lockheed Propulsion Company 156-Inch Solid Rocket Motor Nozzles (U). Vidya Technical Note 8032-TN-2, Vidya Div. of Itek Corp., July 26, 1965. CONFIDENTIAL

4-3 Back, T. H., Massier, P. F., and Cuffel, R. F., Flow Phenomena and Convective Heat Transfer in a Conical Supersonic Nozzle, Journal of Spacecraft and Rockets, August 1967.

SECTION 5

NOZZLE MATERIALS PERFORMANCE FOR A BERYLLIUM PROPELLANT MOTOR

A special studies program was performed which encompassed the study of materials performance in the nozzle of an upper stage beryllium propellant motor.* The study was broken down into two basic phases:

Calculation of the material ablation and thermal response for a typical nozzle and duty cycle, including a restart

Analytical screening of several different materials for potential nozzle applications

The results of these efforts are presented below by phase in Sections 5.1 and 5.2, respectively.

5.1 ANALYSIS OF A TYPICAL NOZZLE DESIGN

The surface and in-depth transient material response for a typical nozzle for an upper stage beryllium propellant motor was calculated at the throat and at a supersonic area ratio of 2.5. A primary firing and a subsequent restart firing were considered. The nozzle configuration assumed for the calculations is shown in Figure 5-1. The nozzle is submerged and has a contoured exit cone. The throat region is made up of pyrolytic graphite washers and the entire exit cone region downstream of the throat is a graphite cloth phenolic. Both regions have silica cloth phenolic as the backup material which in turn is backed up by a steel shell. The pyrolytic graphite washer configuration results in high thermal conductivity in the radial direction. For purposes of analysis, the graphite phenolic was assumed to be MX4500 and the silica phenolic to be FM5131.

The propellant was assumed to be a standard Thiokol beryllium propellant with a 6291°R (5831°F, 3495°K) chamber temperature at 550 psia chamber pressure. The above values and the actual propellant chemical composition were supplied by Thiokol Chemical Corporation. The following duty cycle was assumed for the upper stage application considered:

40 second primary burn, 550 psia chamber pressure
10 second natural cooldown
20 second quench, surface temperature assumed to be 1000°R (540°F)
1730 second natural cooldown after quench
8 second secondary burn, 550 psia chamber pressure

*This study and the general ground rules were defined by William Cohen, NASA Headquarters.

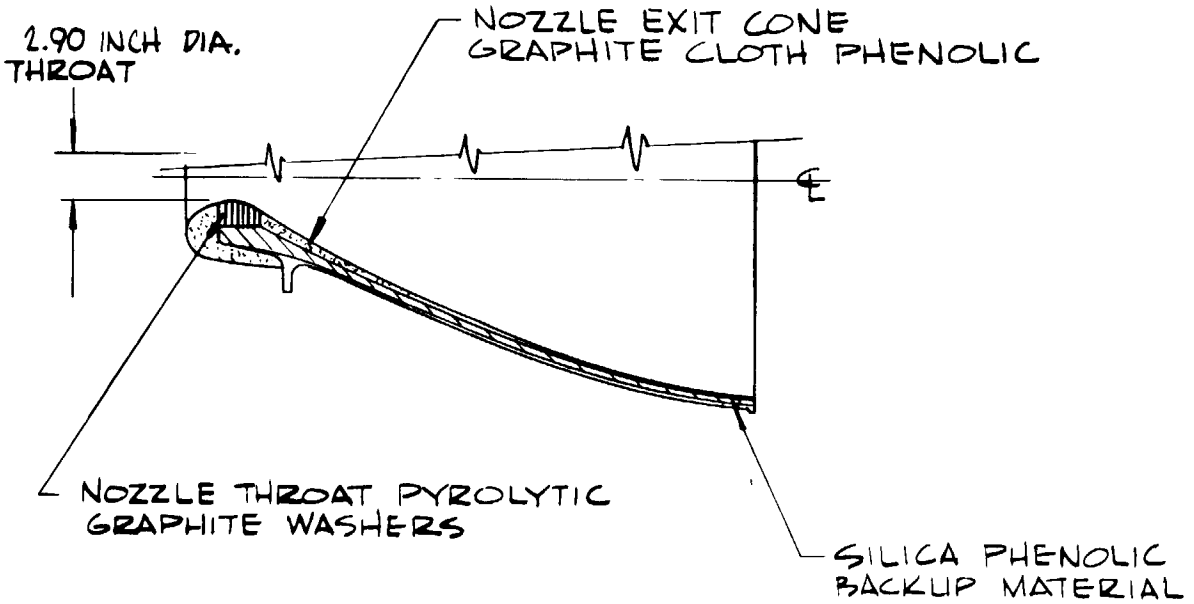

FIGURE 5-1 TYPICAL BERYLLIUM PROPELLANT MOTOR NOZZLE CONFIGURATION

The quench assumption is completely arbitrary and was not defined with any specific system in mind. Actually, subsequent to the calculations, it was learned that the quench could have been heated more realistically by assuming it to start right at shutdown.* This difference should not affect the general conclusions reached, however. The nominal 30-minute cooldown was chosen as a computational convenience; the actual results for the secondary burn are also valid for much longer cooldown periods.

The calculation of material response was performed as presented in Section 2 and Reference 2-2. However, a few exceptions and comments should be noted. In the surface thermochemistry calculations, unequal diffusion coefficients were assumed as opposed to the less accurate equal diffusion coefficient assumption normally used for aluminized propellants.** The heat and mass transfer coefficients used in the response calculations were estimated; no detailed flow-field analysis and boundary layer integration compuation were performed. The actual values used should be within 20 percent of those that would be obtained by the more exact procedures. In the surface thermochemistry calculation, beryllium oxide particle deposition was assumed not to occur and no beryllium condensed phases were allowed to occur at the surface. These assumptions are discussed further in Section 5.2.

In the response calculations for pyrolytic graphite, the surface recession was assumed to be diffusion rate controlled (equilibrium). This recession may, in fact, be kinetically controlled, however. If so, the equilibrium assumption would result in a higher than actual predicted recession. Since the necessary reaction rate data to allow consideration of kinetically controlled surface reactions are not available, it was not possible to consider reaction rate controlled surface reactions.*** The calculated surface temperatures were sufficiently high that diffusion rate control may well be a realistic assumption anyway. In any case, the diffusion control assumption yields the maximum surface recession which would be expected and, therefore, if not realistic, at least provides the upper limit on surface recession.

---

*Since the surface temperature is high at shutdown and the quench fluid is typically water, the surface thermochemical response during quench may be important for this case.

**Because of precedence and because, for aluminized solid propellants, there is no major effect on calculated response between the equal and unequal diffusion coefficients assumptions, equal diffusion coefficients are used as the "standard" for aluminized propellants.

***A recent program performed by Aerotherm (Reference 5-1) has measured the kinetic rate constants for the reactions of H_2O, H_2, and CO_2 with pyrolytic graphite for the orientation in which the low conductivity direction is normal to the surface.

The pyrolytic graphite thermal response was calculated assuming one-dimensional, axisymmetric conduction (CMA computer program); this is perfectly reasonable for the washer configuration since the high conductivity direction is radial and the low conductivity direction is axial. The silica phenolic backup material was not treated as a charring material in the calculations presented herein although this capability exists in the current CMA computer program.

The predicted surface and in-depth response for the typical beryllium propellant motor nozzle of Figure 5-1 is presented in Figures 5-2 through 5-9 for the throat and for $A/A_* = 2.5$. The surface recession response as a function of firing time at both locations is shown in Figure 5-2. The pyrolytic graphite throat recession at the end of the primary burn is just over 0.4 inch and at the end of the secondary burn just under 0.5 inch; the total initial pyrolytic graphite thickness is about 1.6 inches. The recession for the graphite phenolic at $A/A_* = 2.5$ is about 0.25 inch at the end of the primary burn and just over 0.30 inch at the end of the secondary burn; the total initial graphite phenolic thickness at this location is about 0.9 inch. The throat recession corresponds to a throat diameter increase from the initial 2.9 inches to a final value after the secondary burn of about 3.9 inches. Recall that, because of the diffusion rate control assumption, this is a maximum value.

The surface temperature history for the throat is presented in Figure 5-3. The maximum surface temperature is in excess of $5000^{\circ}F$. The pyrolytic graphite - silica phenolic interface temperature is presented in Figure 5-4. Because of the high conductivity of the pyrolytic graphite in the radial direction, this interface temperature exceeds $4000^{\circ}R$ prior to quench. Under these conditions the silica phenolic will definitely char and produce off-gases which must vent between the washers. Note that the quench is very effective in pulling the interface temperature down and, therefore, limiting the char penetration in the backup material. Based on the temperature distribution presented in Figure 5-5, this char penetration should not exceed 0.25 inch prior to the secondary burn. The relatively small temperature gradient through the pyrolytic graphite and the significant effect of the quench are also apparent from Figure 5-5.

The surface temperature history for the graphite phenolic at $A/A_* = 2.5$ is presented in Figure 5-6. The surface temperature reaches a maximum of $5000^{\circ}R$ at the end of the primary burn. The interface temperature history between the graphite phenolic and silica phenolic backup material is shown in Figure 5-7. This interface temperature is well below that at the throat because of the significantly lower thermal conductivity of graphite phenolic. On the basis of this result and the temperature distributions presented in Figure 5-8, very little charring of the silica phenolic would be expected.

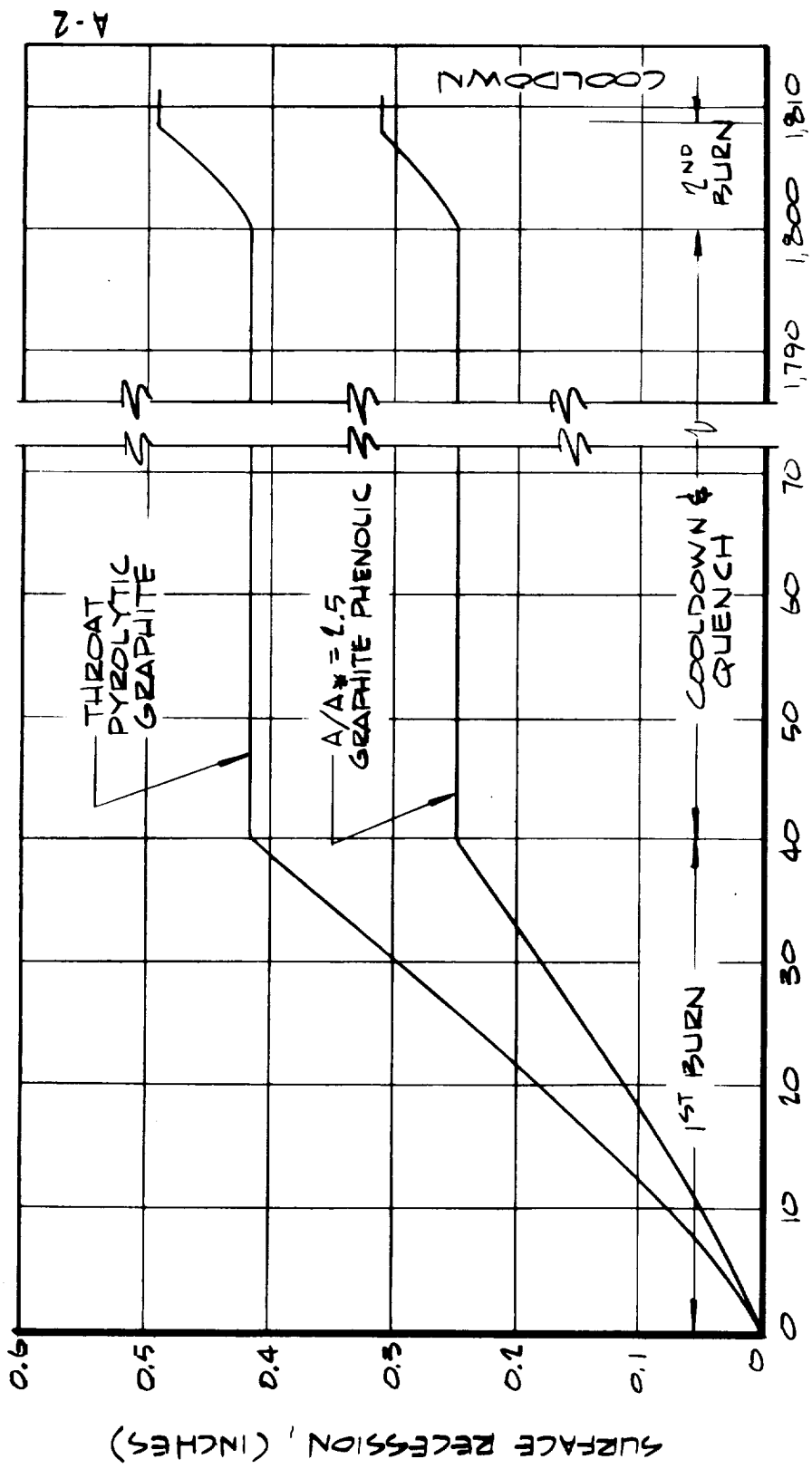

FIGURE 5-2 PREDICTED SURFACE RECESSION FOR THE THROAT AND A/A* = 1.5, BERYLLIUM PROPELLANT MOTOR

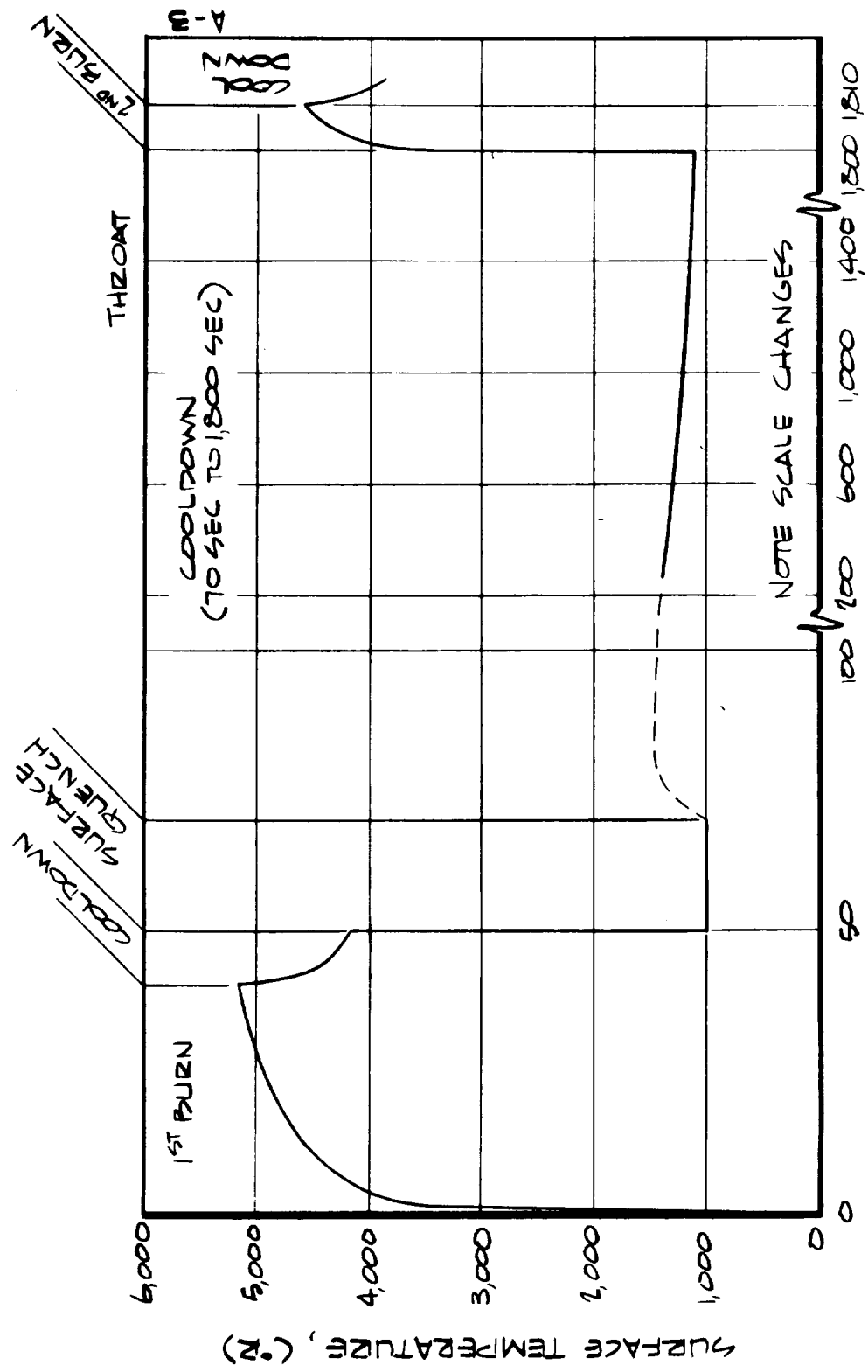

FIGURE 5-3 PREDICTED SURFACE TEMPERATURE HISTORY FOR THE PYROLYTIC GRAPHITE THROAT, BERYLLIUM PROPELLANT MOTOR.

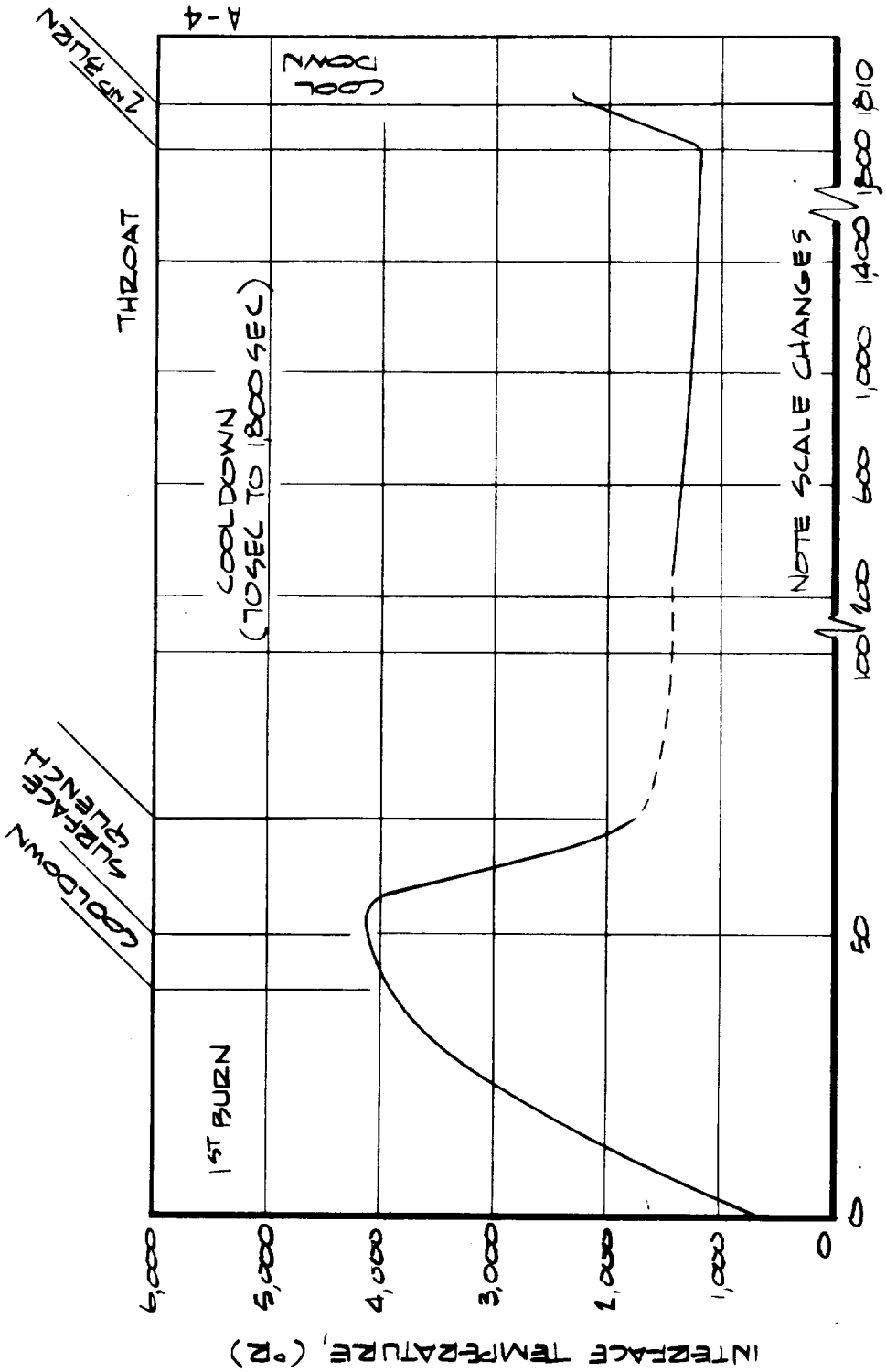

FIGURE 5-4 PREDICTED PYROLYTIC GRAPHITE/SILICA PHENOLIC INTERFACE TEMPERATURE HISTORY AT THE THROAT, BERYLLIUM PROPELLANT MOTOR.

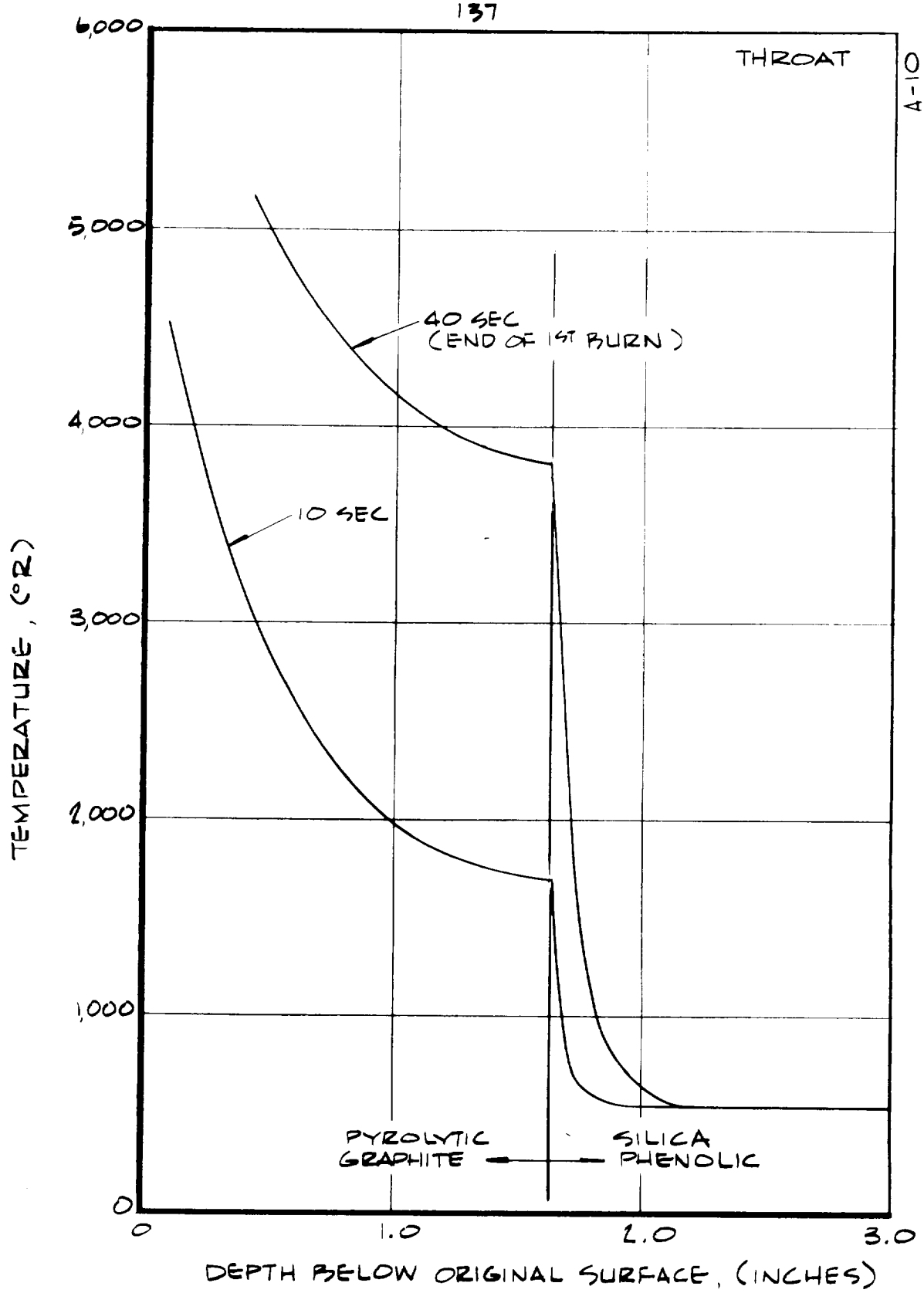

a) PRIMARY BURN

FIGURE 5-5 PREDICTED TEMPERATURE DISTRIBUTIONS FOR THE PYROLYTIC GRAPHITE THROAT, BERYLLIUM PROPELLANT MOTOR.

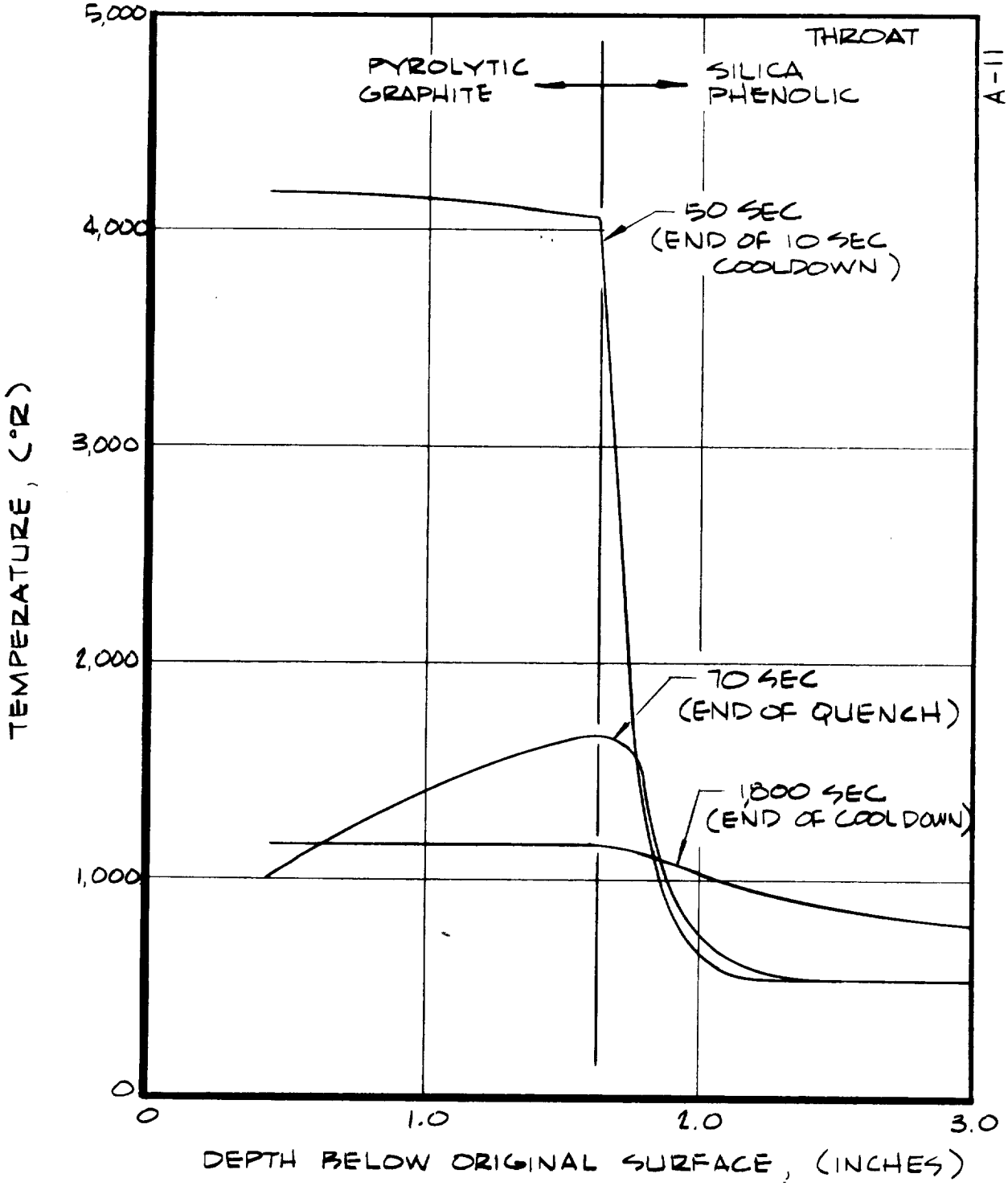

b) COOLDOWN & QUENCH

FIGURE 5-5 CONTINUED

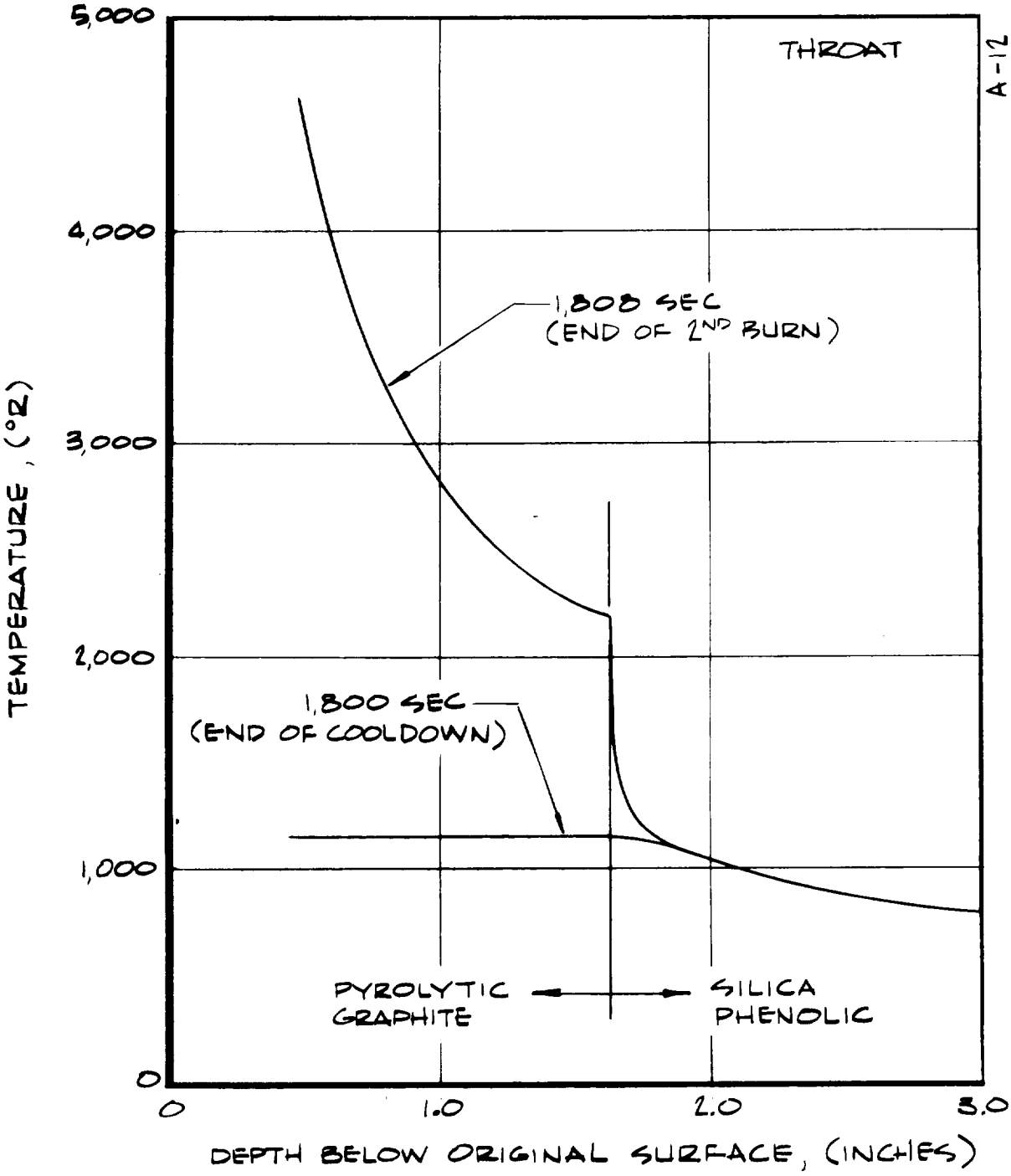

c) SECONDARY BURN

FIGURE 5-5 CONCLUDED

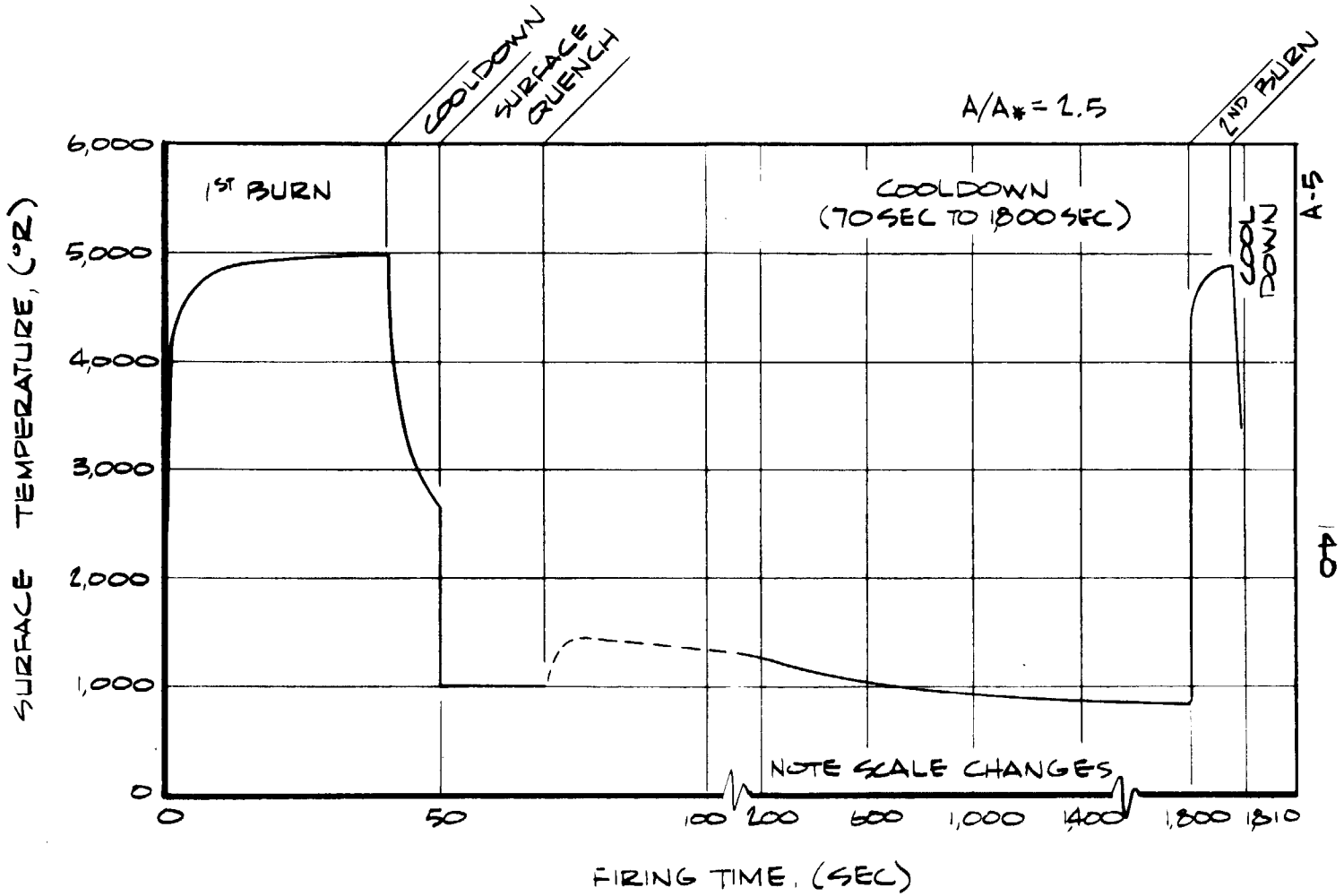

FIGURE 5-6 PREDICTED SURFACE TEMPERATURE HISTORY FOR GRAPHITE PHENOLIC AT $A/A_* = 2.5$, BERYLLIUM PROPELLANT MOTOR.

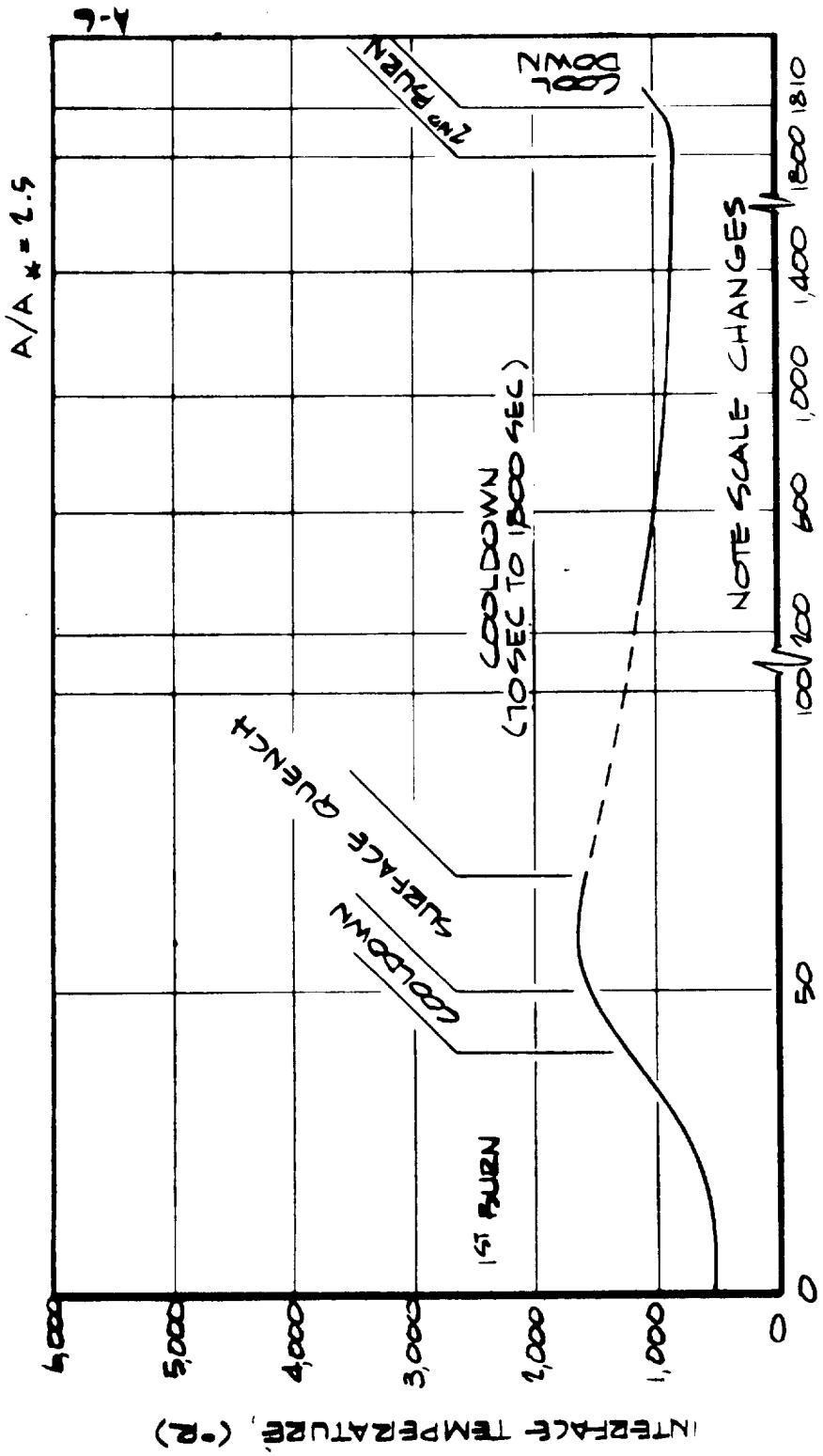

FIGURE 5-7 PREDICTED GRAPHITE PHENOLIC/SILICA PHENOLIC INTERFACE TEMPERATURE HISTORY AT $A/A^* = 1.5$, BERYLLIUM PROPELLANT MOTOR

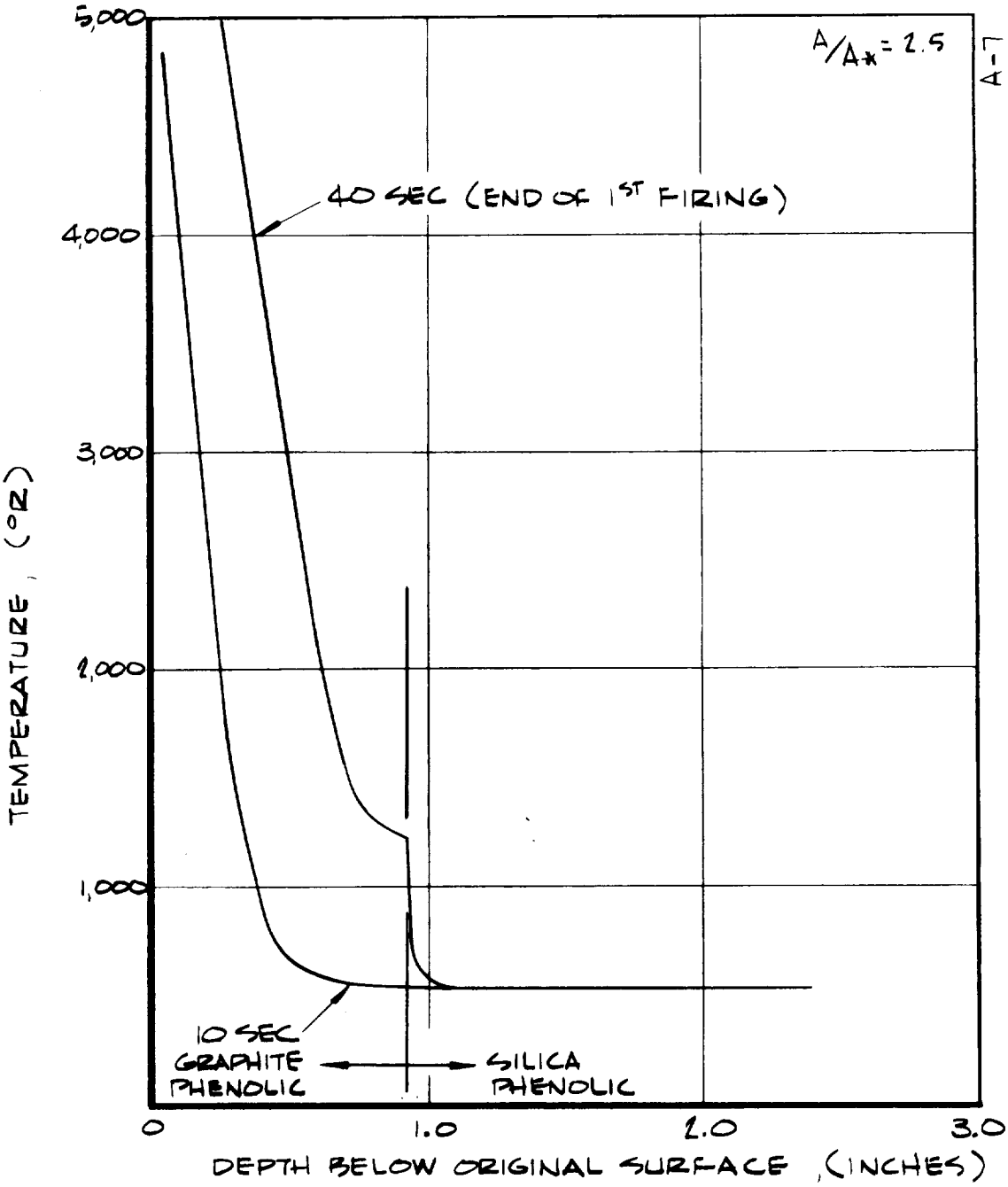

a) PRIMARY BURN

FIGURE 5-8 PREDICTED TEMPERATURE DISTRIBUTIONS FOR GRAPHITE PHENOLIC AT $A/A_x = 2.5$, BERYLLIUM PROPELLANT MOTOR.

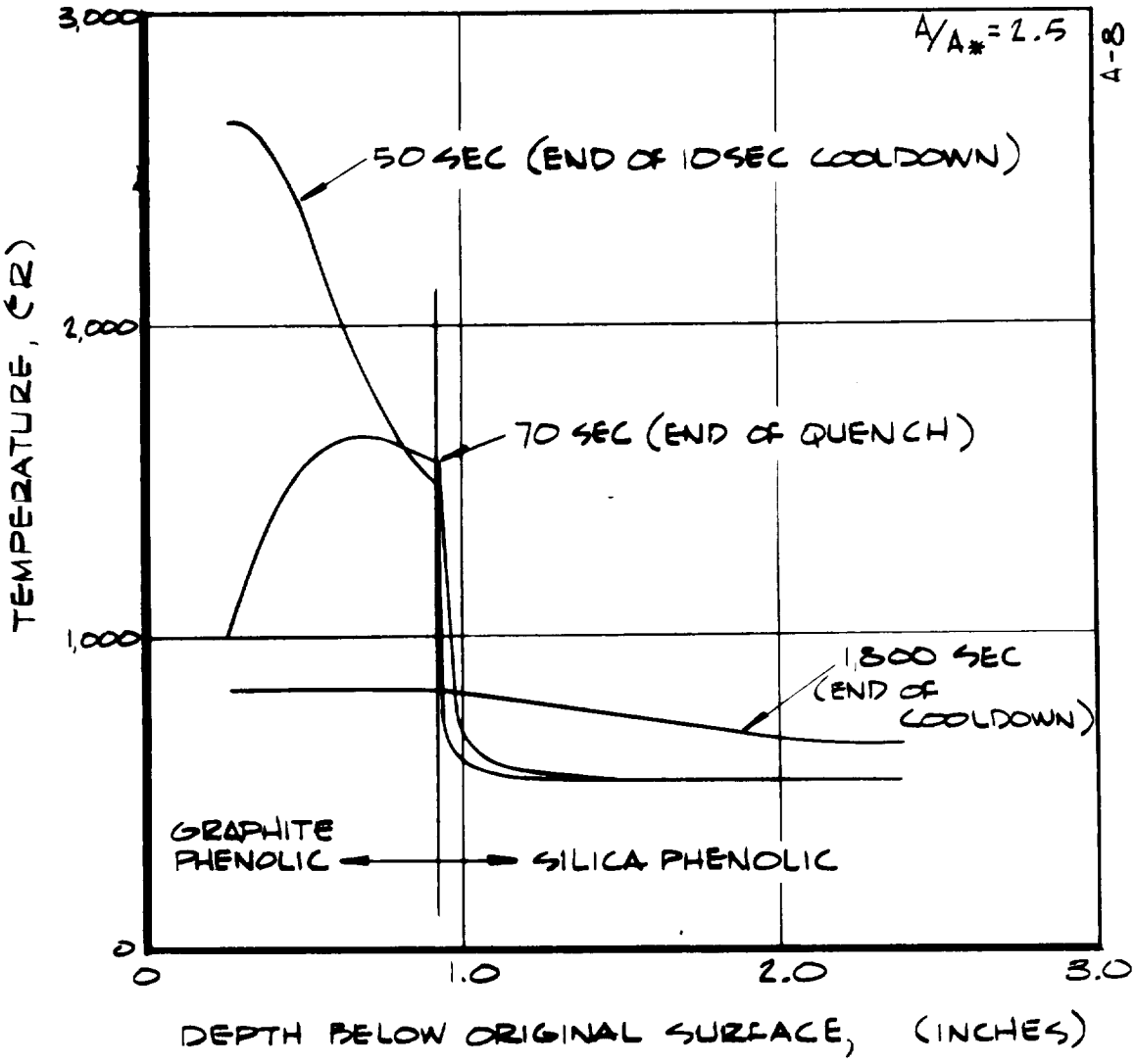

b) COOLDOWN & QUENCH

FIGURE 5-8 CONTINUED

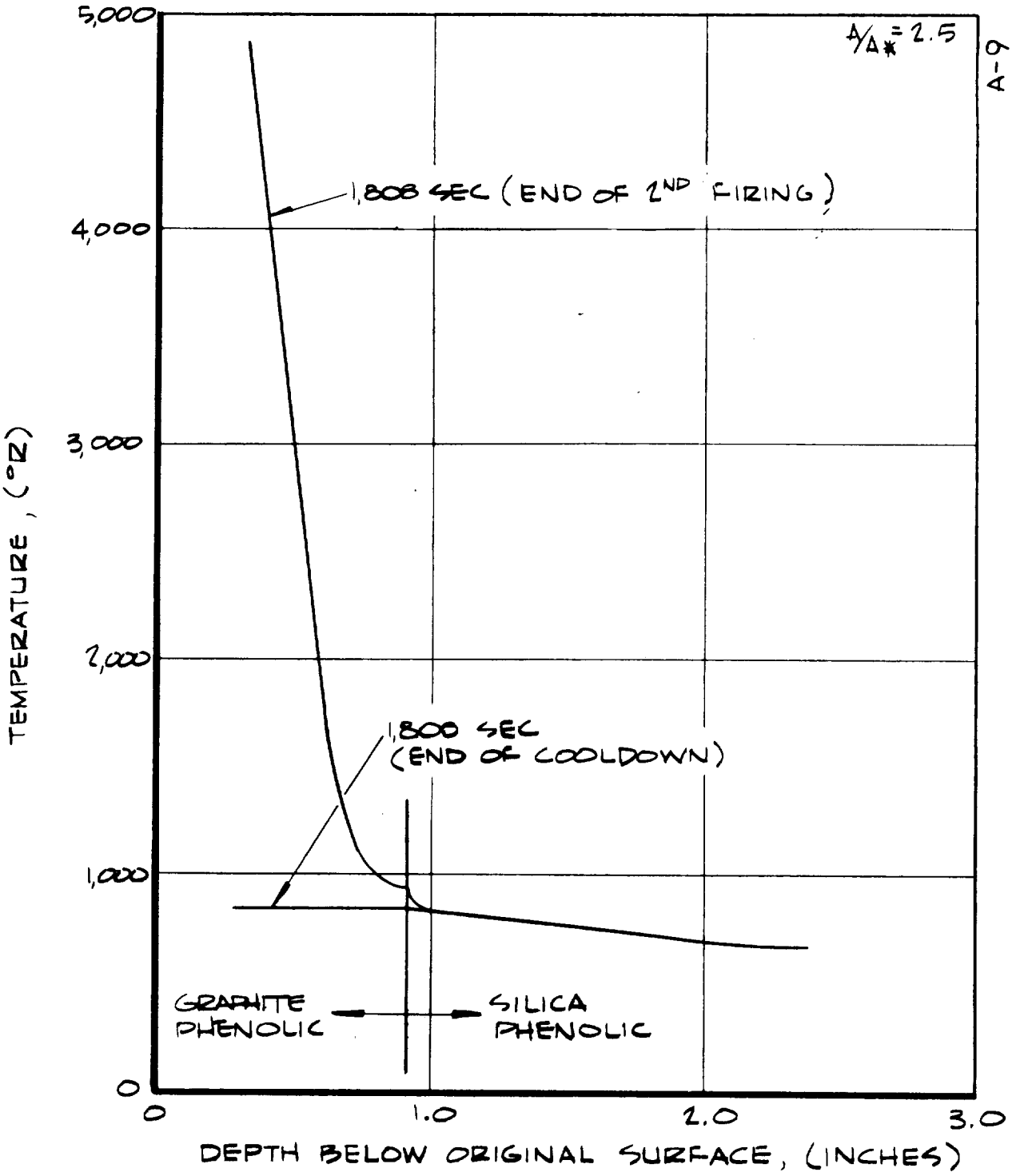

c) SECONDARY BURN

FIGURE 5-8 CONCLUDED

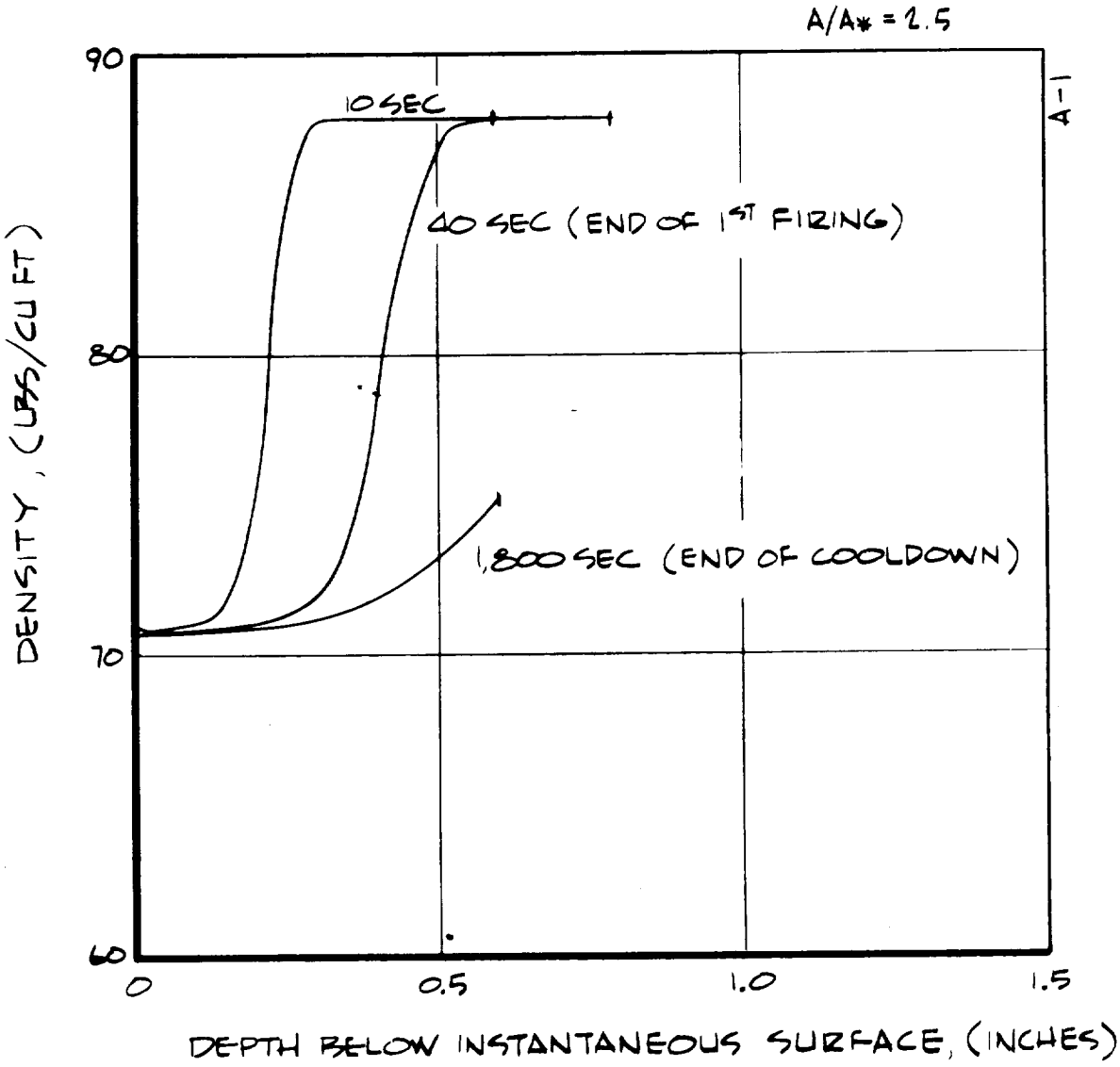

FIGURE 5-9 DENSITY DISTRIBUTIONS FOR GRAPHITE PHENOLIC AT $A/A_* = 2.5$, BERYLLIUM PROPELLANT MOTOR.

Also, because of the low conductivity of the graphite phenolic, the quench is not as effective as for pyrolytic graphite (Figure 5-8).

The density distribution through the graphite phenolic section is presented in Figure 5-9. At the end of the primary burn, approximately 0.25 inch of virgin material remains in-depth, the char thickness being about 0.6 inch. At the end of cooldown, however, the heat soak has resulted in the complete graphite phenolic section being almost fully charred. On this basis, the integrity of this part during the secondary burn is somewhat questionable.

In summary, the surface recession of the pyrolytic washers in the throat is large if diffusion rate controlled surface chemical reactions occur. Significant decomposition of the silica phenolic backup material occurs and therefore provision for venting must be made. The graphite phenolic exit cone material will be completely charred, at least to an area ratio of 2.5, at the start of the secondary burn. The integrity of this part for a restart is therefore somewhat questionable.

5.2 ANALYTICAL SCREENING OF MATERIALS

The applicability of several materials for use in the beryllium propellant environment was defined through analytic screening calculations. In these calculations, the steady-state surface recession rate and surface temperature were defined for the conditions in the throat of the nozzle considered in Section 5.1 (Figure 5-1). The materials considered were:

Graphite
Graphite Phenolic
Silica Phenolic
Beryllium Oxide
Beryllium
Tungsten
Silicon Carbide

Before presenting the results, the beryllium propellant environment as it affects material response and the calculational technique employed are first discussed.

The combustion products of a beryllium propellant contain significant quantities of beryllium gas phase species (e.g., BeCl, BeOH). This is contrary to typical aluminized propellant for which the gas phase aluminum species are negligible. Because of this, condensed phase beryllium species can form at the surface and can have an important effect on surface recession and temperature through the formation of a flowing melt layer or the build-up of a solid phase surface. Note that this condensed phase formation is exclusive of any BeO* particle deposition that might occur. The possible condensed phase species that can form at the surface are Be*, BeO*, Be_2C*, Be_3N_2*, and

$BeCl_2^*$; under certain conditions more than one of these species can occur at the surface at once.

It is interesting to note that a beryllium condensed phase (or phases) has been observed on nozzle surfaces in firings of beryllium propellant motors (e.g., Reference 5-2). This has been attributed to particle deposition. However, for circular grain ports and axisymmetric nozzle configurations, particle deposition would not be expected to be important and any observed depositions would probably be due to the condensation discussed above.

The screening calculations were performed using the Aerotherm Chemical Equilibrium (ACE) Computer Program and the Steady-State Charring Material Ablation (SSCMA) Computer Program as discussed in Section 4. Because of the large number of possible condensed phase species, the theoretical treatment of their formation and subsequent removal is quite complex and was beyond the capabilities of the ACE program. The program was therefore modified to allow for these complications, including the possible formation and removal of several condensed species within the constraints of surface chemical equilibrium. The steady-state response calculations were performed for two basic assumptions: first, condensed phase species were allowed to form in equilibrium as discussed above and second, condensed phase species were not allowed to form. This latter case provided the basis for assessing the effect of the condensed phase formation on the material response. In the calculations, melt removal of the exposed material was allowed wherever appropriate. The melt or fail temperatures (Reference 2-7) for the possible surface species are presented in the table below. It should be noted that when the parent nozzle material

Condensed Phase	Fail Temperature ($^{\circ}$R)
SiO_2*	3389
SiC*	4991
Si*	3035
Si_3N_4*	1800
W*	6570
WO_2*	3600
WO_3*	3140
WCl_5*	905
WCl*	1005
Be*	2800
BeO*	5076
Be_2C*	4325
Be_3N_2*	4450
$BeCl_2$*	1228

has a low fail temperature, the effective fail temperature for any high fail temperature condensed phase must be close to that of the parent nozzle material. Therefore wherever necessary, the fail temperatures were modified such that the fail temperature of any condensed phase could not exceed that of the parent nozzle material. For example in the calculation of the response of beryllium, the fail temperatures for BeO*, Be_2C*, and Be_3N_2* were set at 2800^{o}R, the fail temperature of Be*.

The calculation results for the seven nozzle materials considered are presented in Table 5-1. Both options, condensed phases allowed and condensed phases not allowed, are included except, of course, for the beryllium oxide and beryllium materials where the latter option is impossible since the nozzle material is one of the condensed phases. The material which occurs as the surface material is also indicated in the table. Note that this material is not necessarily the same as the nozzle material.

The most attractive material from a surface recession standpoint is tungsten which exhibits an almost negligible recession rate. It, however, may be unattractive from a weight and structural standpoint and also has a high thermal conductivity. Graphite is the next most attractive material even though the steady state recession rate is quite high. Note that this value corresponds to diffusion rate control of the surface chemical reactions; if they are reaction rate controlled the recession would be lower. The ranking of the remaining nozzle materials in order of increasing recession rate is graphite phenolic, silica phenolic, beryllium oxide, silicon carbide, and beryllium. The recession rate for beryllium is almost astronomical - over 1 inch per second. Based on these results, graphite (or barbonaceous) materials and possibly tungsten are the most attractive for nozzle materials in beryllium motors. Additional analytical screening results for the same beryllium propellant at different firing conditions and for different nozzle materials are presented in Reference 5-3.

For the boundary conditions considered herein (the throat conditions of Section 5.1), only silica phenolic exhibits an effect due to the exclusion of condensed phases. If condensation of beryllium species does not occur, the predicted recession for silica phenolic more than doubles. At lower surface temperatures than found for the boundary conditions considered herein, condensation of beryllium species will also occur for graphite and graphite phenolic (or their carbon counterparts). In all cases, the surface material is beryllium oxide. On the basis of these results, beryllium oxide can occur on graphite, carbon, graphite phenolic, carbon phenolic, and silica phenolic nozzle parts in a beryllium propellant motor in the absence of any particle deposition.

TABLE 5-1

STEADY STATE PERFORMANCE OF VARIOUS NOZZLE MATERIALS IN THE THROAT OF A BERYLLIUM PROPELLANT MOTOR

Nozzle Material	Density (lb/ft^3)	Resin Mass Fraction	Condensed Phase Beryllium Species Allowed			Condensed Phase Beryllium Species Not Allowed		
			$\dot{s}$ (mils/sec)	T_w (^oR)	Surface Material	$\dot{s}$ (mils/sec)	T_w (^oR)	Surface Material
Graphite or Carbon	130	--	13.9	5620	C*	13.9	5620	C*
Graphite Phenolic or Carbon Phenolic	87.5	0.340	23.7	5440	C*	23.7	5440	C*
Silica Phenolic	104.8	0.325	40.0	5076	BeO*	87.0	4140	SiC*
Beryllium Oxide	188	--	63.5	5076	BeO*	--	--	--
Beryllium	113.2	--	1220	2800	Be*	--	--	--
Tungsten	1203	--	0.02	5970	W*	0.02	5970	W*
Silicon Carbide	198	--	75.0	4991	SiC*	75.0	4991	SiC*

REFERENCES - SECTION 5

5-1 Schaefer J., Reese, J., and Anderson, L., Determination of Kinetic Rate Constants for the Reaction of Solid Propellant Combustion Products with Pyrolytic Graphite. Aerotherm Final Report No. 68-31, May 1, 1968.

5-2 Smallwood, W., et al., Beryllium Erosion Corrosion Investigation for Solid Rocket Nozzles (U). Fourth Technical Progress Report, Contract AF 04(611)-10753, Technical Report AFRPL-TR-67-16, February 1967. CONFIDENTIAL

5-3 Clark, K., Rindal, R., Inouye, L., and Kendall, R., Thermochemical Ablation of Rocket Nozzle Insert Materials, NASA CR-66632, Aerotherm Final Report No. 68-29, February 15, 1968.